LEBANESE AMERICAN UNIVERSITY

PIV and CFD Investigation of Flocculation

Hydrodynamics

By

Hrair Razmig Danageuzian

A thesis

Submitted in partial fulfillment of the requirements

for the degree of Master of Science in Civil and Environmental Engineering

School of Engineering

May 2019

THESIS APPROVAL FORM

Student Name: Hrair Danageuzian   I.D. #: 201300933

Thesis Title: PIV and CFD Investigation of Flocculation Hydrodynamics

Program: Master of Science in Civil & Environmental Engineering
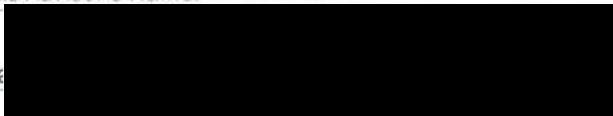
Department: Civil Engineering

School: Engineering

The undersigned certify that they have examined the final electronic copy of this thesis and approved it in Partial Fulfillment of the requirements for the degree of:

Master of Science _____ in the major of Civil & Environmental Engineering

Thesis Advisor's Name: Dr. Jean Chatila

Signature: ██████████████   Date: 17 / 05 / 2019
                                          Day   Month   Year

Committee Member's Name: Dr. Caesar Abi Shdid

Signature: ██████████████   Date: 17 / 5 / 2019
                                          Day   Month   Year

Committee Member's Name: ██████████

Signature: ██████████████   Date: 17 / 5 / 19
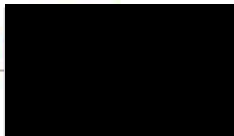   Day   Month   Year

ii

THESIS COPYRIGHT RELEASE FORM

Name: Hrair Danageuzian

Signature:

Date: 17 / 05 / 2019
Day / Month / Year

PLAGIARISM POLICY COMPLIANCE STATEMENT

I certify that:

1. I have read and understood LAU's Plagiarism Policy.
2. I understand that failure to comply with this Policy can lead to academic and disciplinary actions against me.
3. This work is substantially my own, and to the extent that any part of this work is not my own I have indicated that by acknowledging its sources.

Name: Hrair Danageuzian

Signature: ███████████

Date: 17 / 05 / 2019
        Day   Month   Year

ACKNOWLEDGEMENT

PIV and CFD Investigation of Flocculation Hydrodynamics

Hrair Razmig Danageuzian

Abstract

The performance of paddle flocculators in water treatment is highly influenced by the basin hydrodynamics. In their design, several hydrodynamic and geometric parameters are required to ensure the efficiency of the process. Amongst these parameters, the slippage factor k is estimated to fall in the range of 0.2 to 0.3. An existing lack of the quantitative understanding of the velocity flow field in such flocculators is evidently identified in the literature. This research investigates the velocity field of turbulent flow in a paddle flocculator, and its influence on the process performance by quantifying k at low rotational speeds of 3 rpm and 4 rpm.

A laboratory scale paddle flocculator was designed and experimentally investigated using particle image velocimetry measurements. Time averaged velocity data of the flow field at a plane perpendicular to the paddle wheel revealed the velocity of water particles surrounding the blades. Numerical simulations using a commercial computational fluid dynamics software package, ANSYS, were generated for the laboratory scale paddle flocculator. The influences of mesh structure and turbulence models SST k–ω and IDDES were evaluated.

As a result, a good correlation between the PIV and CFD results was verified through a Goodness-of-Fit evaluation (with a coefficient of determination almost equal to 0.9).

Results showed that the SST k–ω model can accurately predict the flocculation flow when the more computationally expensive IDDES model is not feasible. The slippage factor k was quantified as 0.18 for both rotational speeds. This indicates that more power is imparted to the water body than estimated in most design procedures, thus yielding higher velocity gradient values for flocculation in the basin. It is expected that the application of the validated CFD model will help improve the design and optimization of paddle flocculators.

Keywords: Flocculation, Velocity Field, Turbulence, Slippage Factor, PIV, CFD.

Table of Contents

List of Tables

List of Figures

List of Abbreviations

PIV	Particle Image Velocimetry
CFD	Computational Fluid Dynamics
LDV	Laser Doppler Velocimetry
SST k–ω	Shear Stress Transport k-omega
IDDES	Improved Delayed Detached Eddy Simulation
rpm	Rotations per Minute
2D	Two Dimensional
3D	Three Dimensional

Chapter One

Introduction

1.1 Background

Our ancestors withheld an apparent importance of ample water quantity for drinking and other purposes, as ancient civilizations established themselves near water supplies. However, an understanding of water quality was not well identified. Historical records document only aesthetic problems regarding drinking water which was the main focus of water treatment. Ancient Sanskrit and Greek writings recommended water treatment methods to improve the taste and odor of drinking water as early as 4000 B.C. The Egyptians aimed at clarifying water by using chemical alum to settle out suspended particles as early as 1500 B.C., and until the mid-1800s, slow sand filtration was being commonly used in Europe. During the late 1800s, scientists had a much more clear understanding of water contaminants that were not visible by the naked eye, and the transmission of diseases through water containing microbes.

Concerns regarding drinking water quality focused on pathogens in public water supplies during the 19th century. In the early 1900s, most drinking water treatment systems in the U.S. aimed at reducing turbidity by removing contaminants which were causing typhoid, dysentery, and cholera. In 1914, federal regulations regarding water quality initiated when the U.S. Public Health Service set standards for bacteriological quality of drinking water. With numerous modifications in these standards emerged the Safe Drinking Water Act of 1974. Numerous health concerns, and the continuous follow up of federal governments urged water treatment plants to improve and maintain the required quality

standards. As years progressed, and with considerable research in this field, water treatment plants continue to improve and progress toward providing clean and safe water to the public (US EPA, Office of Water, 2000). Water Supply and Distribution-Engineered systems preventing the spread of disease and increasing life expectancy was nominated as the fourth engineering achievement of the 20th century (Wulf, 2000).

1.2   Water Treatment Overview

Water is essential for human beings and other living things, and the availability of clean and safe water at our homes is taken for granted. Behind this convenience lies water treatment plants and facilities. Water treatment can be defined as the processing of water to achieve a water quality that meets specified goals or standards set by regulatory agencies (Howe et al., 2012). The critical role of such plants is to meet water quality standards while also reducing power and energy demands. With pumps, motors, and other equipment operating continuously, water and wastewater facilities are considered among the largest consumers of energy in a community.

Sustainability and energy consumption should be considered in selecting, designing, and operating treatment processes because the treatment and distribution of potable water is one of the most energy-intensive industries (Howe et al., 2012). According to United States Environmental Protection Agency (US EPA), the energy consumed by water and wastewater facilities accounts for 35 % of typical U.S. municipal energy budgets. Electricity use accounts for 25 to 40 % of the operating budgets for wastewater utilities and approximately 80 % of drinking water processing and distribution costs. In addition, as much as 40 % of operating costs for drinking water systems can be for energy, noting that the cost of this energy is largely consumed in the flocculation basin. (US EPA, 2013).

Water treatment plants treat raw water by removing impurities and natural organic matter in a conventional method composed of numerous processes which are coagulation, flocculation, clarification/sedimentation, filtration, and disinfection. The coagulation – flocculation processes are the bedrock of the treatment process, and therefore these processes must occur at the highest possible efficiency to ensure the optimal performance of a water treatment plant. Coagulation is the addition of a coagulant to destabilize colloidal particles during rapid mixing. This allows particles to agglomerate into flocs and consequently settle in a practical period of time (Droste, 1997). Coagulation has been well studied and researchers have conducted experiments and drawn conclusions regarding major coagulation mechanisms. The optimization of the coagulation process has been studied by examining numerous operational parameters such as the coagulant dosage, physiochemical conditions, and hydrodynamic conditions (Zhong et al., 2011).

Flocculation is the process following coagulation, in which the small colloidal particles that were destabilized, conjoin as a result of inter-particle contact while the fluid is subjected to hydraulic shear by gentle stirring. The outcome of flocculation is the formation of flocs that can be removed by sedimentation and filtration (Wang, & Shammas, 2015). Flocculation requires slow mixing over a period of 20 minutes to 40 minutes, and a high amount of energy is required to mix the large volume of water.

This study investigates the rotational mixing flow inside a laboratory scale paddle flocculator by examining the velocity field and streamlines surrounding the blades of the paddle wheel. The slippage factor of the water mass in the flocculator is quantified, and its influence on the efficiency of the flocculation process is addressed.

1.3   Research Aim and Objectives

This research aims to investigate the velocity field of turbulent flow in a laboratory scale paddle flocculator. The research aim is achieved through the following objectives:

1. Conduct a comprehensive literature review on the history and theory of flocculation hydrodynamics.

2. Identify typical paddle flocculator designs and establish a laboratory scale prototype for flow visualization.

3. Develop an experimental understanding of the flow field surrounding the blades of the laboratory scale paddle flocculator.

4. Generate CFD models of the paddle flocculator prototype for flow simulation.

1.4   Scope of Work

The scope of work of this study is as follows:

1. Conducting PIV experiments for flow visualization at a plane perpendicular to the blades of the laboratory scale paddle flocculator.

2. Modeling the laboratory scale paddle flocculator using commercial CFD software ANSYS Fluent.

3. Producing time averaged velocity contours and vector profiles above blade faces from both approaches.

4. Validating the CFD models generated through comparison of simulated results with experimental results.

5. Conducting a Goodness-of-Fit evaluation, based on the coefficient of determination, for velocity magnitude data above blades from PIV and CFD.

5. Analyzing the results obtained to understand flow structures and velocity fields surrounding the blades of the paddle flocculator.

6. Quantifying the slippage factor k through the power imparted to water from the validated CFD models.

7. Delivering conclusions and recommendations.

1.5 Research Significance and Contribution

The significance of this research lies in providing a quantitative understanding of the velocity flow field inside a paddle wheel flocculator prototype. This is achieved through flow visualization using PIV, and flow modeling using CFD.

The contribution of this research is the quantification of the slippage factor, which is a dimensionless parameter in the design of paddle flocculators, through validated CFD models. The impact of the research findings is correlated towards a better understanding of the basin hydrodynamics and the process efficiency.

Experimental data are produced which can be used for future research, and verified CFD models are presented which can be used as tools to further examine other aspects of flocculation hydrodynamics.

Chapter Two

Literature Review

The quality of a water source cannot be overlooked in water supply development, and nearly all sources of water require some form of treatment before potable use. The evolution of water treatment has a rich history of empirical and scientific developments. The following comprehensive literature review is divided into six sections. The first section addresses the theory of flocculation. In the second section, flocculation basins are discussed in terms of mixing flow and design parameters. PIV and flow visualization are presented in the third section. While in the fourth section, experimental investigations of flocculation using PIV are discussed. CFD is addressed in the fifth section, while numerical modeling of flocculation is covered in the final sixth section.

2.1   Flocculation Theory

In 1917, Smoluchowski based the theory of flocculation on his observation of small particles undergoing random Brownian motions due to collisions with fluid molecules which resulted in particle-particle collisions. While in 1921, Langelier based the theory behind flocculation on the idea of stirring water comprising particles creating velocity gradients that produce particle collisions. The characteristics of particles and the conditions of fluid mixing determine the action of flocculation. Particles must become destabilized in order to start flocculating, and this is achieved in the coagulation stage.

Flocculation mechanisms differ with particle size, where for small particles (less than 0.1 µm) the primary flocculation mechanism is Brownian motion or microscale flocculation.

Microscale flocculation or better known as perikinetic flocculation is the aggregation of small particles into microflocs (1 to 100 μm). While for particles larger than 1 μm, the primary flocculation mechanism is gentle mixing of water by means of a mechanical mixer. Collisions between suspended particles are achieved by the velocity gradients arising from gentle mixing. This is known as macroscale or orthokinetic flocculation. Furthermore, in 1978, O'Melia studied the flocculation mechanism for suspensions containing a wide range of particle sizes. Differential particle settling or sedimentation is an apparent flocculation mechanism for these heterogeneous suspensions due to differences in settling velocities.

The erosion and disruption of floc aggregates, which is termed as floc breakup is apparent in macroscale flocculation since particle flocs are subjected to shear forces. After some period of mixing, the formation and breakage of flocs is stabilized, and a steady state floc size distribution is reached. The hydrodynamics of the entire system, in addition to the chemistry of the coagulant-particulate interactions determine the rate at which steady-state size distribution is achieved (Crittenden, 2012).

2.1.1 Particle aggregation, floc formation, and floc growth

Particles aggregate on collision with other particles when they are sufficiently destabilized in the coagulation phase (Gregory, 2009). The agglomeration process can be separated into two steps, starting first with the collision of agglomerating particles and secondly the adhesion of these particles upon collision (Jarvis et al., 2005). As mentioned earlier, particle collision takes place at a second order rate that is dependent on the flocculation transport mechanisms of Brownian diffusion, fluid shear, and differential settling (Oyegbile et al., 2016). Upon the collision of particles and their adhesion, floc

formation occurs. The rate of floc growth depends fundamentally on the rate of particle collisions and the nature of particle interactions.

$$R_{floc} = \alpha R_{col} - R_{br}$$

The rate of floc growth (R_{floc}) is considered as the difference between the rate of aggregation and the rate of floc breakage (R_{br}), knowing that floc growth is limited by floc breakage which is discussed next. The rate of aggregation is represented as the rate of particle collision (R_{col}), and a collision efficiency factor (α) which is the fraction of collisions that result in attachment (Jarvis et al., 2005).

2.1.2 Floc strength, breakage, and regrowth

Flocs can be described as loosely connected aggregates that are highly porous and have an irregular shape. Since flocs are composed of small primary particles, the strength of a floc is highly reliant on the number and magnitude of the interparticle interactions and bonds between the constituents of aggregates (Jarvis et al., 2004). Floc strength is directly related to floc structure, consequently it is highly dependent on the floc formation process. Therefore, the physiochemical conditions including raw water type, coagulant type and dose, and floc structure control floc strength (Jarvis et al., 2005).

Floc size is well thought of as a balance between hydrodynamic forces that are applied on flocs and the strength of flocs. Therefore, during flocculation, flocs grow until reaching a certain rather limiting size beyond which breakage occurs (Bridgeman et al., 2010). As previously stated, the limiting size is often referred to as a steady state phase which is a balance between floc growth and breakage at a specified shear condition (Oyegbile et al., 2016).

The theoretical growth – breakage mechanism of flocs is expressed as the ratio of hydrodynamic forces to floc strength.

$$B = \frac{\text{Hydrodynamic Forces}}{\text{Floc Strength}} = \frac{F}{J}$$

When flocs cannot endure the hydrodynamic forces exerted ($B > 1$), then breakage occurs. However, when flocs are strong enough to withstand the hydrodynamic forces ($B < 1$), then flocs remain intact and maintain their size, or might even experience growth (Coufort et al., 2005).

In general, two modes of floc rupture or breakage have been acknowledged. These two modes are categorized as either surface erosion or large-scale fragmentation. The removal of small particles from the floc surface is identified as surface erosion which is owing to the shearing stress acting tangentially to the floc surface. While large-scale fragmentation is the breakage of flocs into pieces of a similar size and it is believed to happen due to tensile stress acting normally across the whole floc (Jarvis et al., 2005). The ability of flocs to regrow is a significant operational parameter during the process of flocculation. Broken flocs that have the potential for re-aggregation will probably not be able to reform to their prior size because of a loss of bonding capacity (Jarvis et al., 2004). In certain cases, floc breakage may be irreversible to an extent that only limited regrowth may occur, however research regarding this aspect is limited (Yukselen & Gregory, 2004).

2.2   Flocculation Basins

2.2.1   Characterization of Mixing Flow in a Flocculation Basin

In 1955, Thomas Camp explained the fundamental theories of the physical process of floc formation, and delivered procedures in the practical application of the theory to the design of flocculation basins. He was the first to characterize mixing in flocculation basins on the basis of the velocity gradient in the mid-1900s. Since then, the velocity gradient has been used to characterize mixing in a range of engineering applications. Camp defined the root mean square velocity gradient as:

$$G = \sqrt{\frac{W}{\mu}} = \sqrt{\frac{P_{Total}}{\mu V}}$$

The work of shear per unit of volume per unit of time at a point is the rate of power dissipation, known as the dissipation function. The mean value of the dissipation function is denoted by W, which is equal to the total power dissipation divided by the volume of the chamber. In addition μ is the absolute viscosity of the fluid. When turbulence is induced by mechanical mixing, the dissipation function is estimated from the drag force of the rotating blades or air bubbles in water and the distance moved per second.

By Newton's law, the drag force for a body immersed in water is:

$$F_D = \frac{1}{2}\rho C_D A v^2$$

Where: ρ is the density of the fluid

              C_D is the drag coefficient

A is the cross sectional area of the submerged object in a plane

perpendicular to the direction of motion

v is the relative velocity of the object with respect to the fluid

The distance moved per second by the submerged blade is equal to its velocity with respect to the liquid. However, Camp discussed that the relative velocity of the stirring blade and of the liquid immediately surrounding the blade is difficult to determine. He indicated that rotary stirring devices set the liquid in spiral motion with an average angular velocity less than the velocity of the rotors. Camp concluded that the relative motion of blade and tank is not the same as the relative motion of blade and surrounding liquid. Rising air bubbles also tend to impart motion to the surrounding liquid, which in turn will result in faster rise of the air bubbles with respect to the tank (Camp, 1955).

CFD played a vital role in quantifying and understanding the local impact of mean flow and turbulence on floc formation and break-up using the local velocity gradient (Bridgeman et al., 2009). The role of CFD and its applications in the water treatment industry is thoroughly discussed in following sections.

2.2.2 Paddle Type Flocculation Basins

In the 1950s, Camp conveyed that most of the available apparatus for flocculation was the revolving paddle type with either vertical or horizontal shafts. In most cases, only rotor paddles are provided. Therefore, the only resistance to rotation of the water with the paddles is the drag on the walls of the tank. Camp identified that little was known about the relative velocity of the paddles and the water.

Knowing that the efficiency of the flocculation process depends on the mixing flow conditions, effective control of the velocity gradient is needed. In a basin provided with rotor paddles, it is necessary to change the speed of rotation of paddles in order to change the magnitude of the mean velocity gradient. Therefore, the power dissipation must be definitely related to the speed of rotation after equilibrium is reached following starting of the paddles. Consequently, rotor paddles must be mounted parallel to the shaft such that the velocity of a paddle with respect to the tank is then proportional to its distance from the shaft. The expression for the dissipation function for a single rotor blade at a distance r_b from the center of the shaft is:

$$W = \frac{F_D v}{V} = \frac{C_D A \frac{62.4}{64.4} v^3}{V} = \frac{C_D A \frac{62.4}{64.4} [2\pi r_b (1 - k) S_o]^3}{V} = \frac{239 C_D A r_b^3 (1 - k)^3 S_o^3}{V}$$

Where: v is the velocity of the blade with respect to the water

r_b is the distance of the center of the blade from the shaft

S_o is the speed of the shaft in revolutions per second

kS_o is the speed of the water in revolutions per second

Camp noted that the validity of the equation depends on the presence of a constant ratio between the rotating speed of the shaft and the velocity of the water surrounding the paddle incorporated in the term k.

Camp investigated four flocculation chambers which were constructed in 1951 – 1952 for the Cambridge water works. The plant was the first practical application of the theory of flocculation. Nothing was known about the velocity of the rotors relative to the surrounding water or about the amount of power loss to be expected in the transmission,

12

bearings, and stuffing boxes. Unidentified tests were conducted on flocculation mechanisms at this plant. Test results showed that after equilibrium is established, the water revolves at approximately 24 % of the speed of the rotors in the high speed compartments (approximately 2 rpm to 5.2 rpm), and at approximately 32 % of the speed of the rotors in the low speed compartments (approximately 1.1 rpm to 2.9 rpm). Therefore, the value of k was found to be between 0.24 and 0.32 (Camp, 1955). No information was provided regarding the methodology used to determine these results or the types of tests which were conducted.

Noting the work of Camp and his conclusions regarding the slippage factor k, a thorough literature review was conducted to identify any source of information regarding a better understanding of k and its estimate. The findings below show different definitions of k from various researchers' and authors' perspectives.

Brabty et al. (1977), discussed the design of flocculation systems. In their work, they stated that "for the present study k was found to have a constant value of 0.24, for the full range of rotational speeds applied." They did not discuss the determination of k in any form. After reviewing the publication record of Dr. Bratby, published results addressing the determination of k were not found. However, Bratby (2016) discussed k as a design parameter in paddle flocculators. He stated that, as a guide, k falls in the range of 0.2 at high impeller speeds (1.8 rpm to 5.4 rpm) to 0.35 at low impeller speeds (0.9 rpm to 3 rpm) by referring to the work done by Camp.

Peavy et al. (1986), addressed k very briefly while discussing the design of paddle flocculators. They stated that the velocity of the paddle tip is the velocity relative to the water and is about 75 % of the actual paddle speed. Thus yielding a k value of 0.25.

Droste (1997), stated that the velocity of the fluid will be less than the velocity of the paddle by a factor k because of slip. "If baffles are placed along the walls in a direction perpendicular to the fluid movement, the value of k decreases because these baffles obstruct the movement of fluid". Without baffles, Droste adopted a k value of 0.25, while with baffles he considered that k is assumed to fall in the range of 0 to 0.15.

Hendricks (2011), stated that since the whole water mass is subjected to motion by the paddle wheel of a flocculator, a slippage factor k is introduced. This factor k is the ratio of rotational velocity of water mass to rotational velocity of paddle wheel, and is considered to fall in the range of 0.24 to 0.32 as per Camp's work. Hendricks proceeded in relating the slippage factor with the rotational speed through an empirical formula. He concluded that slippage factors calculated through the formula also fall within the range established by Camp.

Howe et al. (2012), discussed the velocity of fluid relative to the paddle (v_R). They stated that "v_R is usually assumed to be 70 to 80 % of the paddle speed without tank baffles. With tank baffles, 100 % of the paddle speed is approached." Thus considering that k is assumed to fall in the range of 0.2 to 0.3.

The review above shows that there are no advancements in the determination and quantification of k since Camp's work in 1955. Researchers and book authors use a slippage factor of k = 0.25 as a guideline, or recommend k values within the range of 0.24 and 0.32 based on Camp's conclusions.

2.3   PIV and Flow Visualization

Numerous scientific developments require a measuring method or technique for velocity distributions across a flow field. A flow visualization technique is needed that can provide quantitative and instantaneous measurements of flow in any structure. This is where PIV emerged. PIV is an optical and non-intrusive method that is related to both flow visualization and optical point techniques. This technique is able to provide accurate quantitative measures of instantaneous flow velocity across a planar area of a flow field.

2.3.1   History of PIV

The term Particle Image Velocimetry first appeared in literature in the early 1980s. The first investigators to achieve such measurements used the method of laser speckle which was originally developed in solid mechanics. They showed that it could be applied to fluid velocity fields. In 1977, three research groups established the feasibility of applying laser speckle phenomenon to fluid flow by measuring the parabolic profile in a laminar tube flow. By 1983, Meynart, who was a young doctoral student at the Karman Institute in Belgium, was the leading expert of this method. He demonstrated that practical measurements could be made in laminar and turbulent flows of liquids and gases. Meynart called his work as Laser Speckle Velocimetry (LSV). Different scientists argued that the illumination of particles by a light sheet in fluid flow would rarely create a speckle pattern. Hence, the term Particle Image Velocimetry was introduced to distinguish this mode of operation from the laser speckle mode.

Many researchers became interested in PIV since it offered a new and exceedingly promising means of studying the structure of turbulent flow. The involvement of different researchers in PIV along the years led to its enhancement and evolvement as a flow

visualization technique. A big step in PIV was the utilization of double pulsed solid state lasers which produced excellent double exposure images of particles. Also, the greatest challenge in PIV during the first decade was the interrogation of images due to limited computer capabilities which became much feasible along the years. In addition, one of the most important changes in PIV was the move from photographic to video graphic recording which immensely improved the popularity of PIV. The current standard PIV system consists of a double pulsed laser with a light sheet, illuminating particles a few microns in diameter along with interline-transfer PIV video cameras and interrogation by correlation analysis. In the 1990s, it was evident that digital imaging would become the standard at some point in the future of PIV. However, it was unexpected the extent to which digital imaging would simplify PIV and thus make it a method everybody would be willing to use. The other outstanding impact of digital PIV was the entrance of interline transfer cameras that could hold two images recorded in rapid succession by transferring the first image by each pixel to an on-chip storage well, and then record a second image. The optical side of PIV also witnessed many developments such as stereographic imaging which provided the third velocity component. It is difficult to predict the future of PIV because the advancement of PIV depends on developments in the technology of components that lie outside its field such as computers, lasers, and cameras. In its modern form, PIV means the accurate and quantitative measurement of fluid velocity vectors at a very large number of points simultaneously, which is indeed a very challenging and complicated achievement. Presently, the standard system sold by commercial companies consists of a double pulsed laser illumination setup, a high speed CCD video camera, and a process control along with an image processing software package (Adrian, 2005).

2.3.2 How PIV Works

Figure 1 demonstrates the general setup of a 2D PIV image acquisition system. In order to obtain measurements using PIV, the flow must be seeded with tiny neutrally buoyant particles called tracers. A light sheet is formed using a double pulsed laser beam through an optical arrangement of cylindrical lenses. Using the light sheet, particles in the flow are illuminated twice with a small time separation or time interval dt. The displacement of particles in the time interval between two laser pulses is recorded. The recorded particle displacement field is measured across the whole field of view of images, scaled by the image magnification, and then divided by the known pulse separation to obtain the flow velocity at each point. A camera is placed perpendicular to the plane of the light sheet to capture the light scattered from the particles.
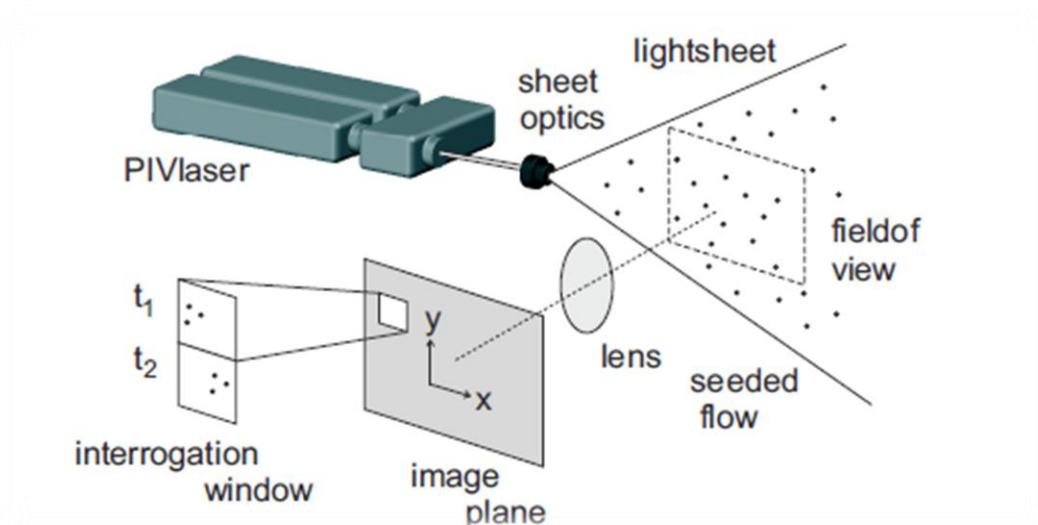
Figure 1: A 2D PIV System Setup (extracted from LaVision PIV Manual)

PIV recordings are divided into interrogation windows which are small subareas as seen in figure 1, and local displacement vectors are determined for each interrogation window using statistical correlation techniques. Interrogation window sizes vary, however a

17

proper size must be selected such that all particles move homogenously in the same direction and the same distance within the area. Regarding the evaluation of particle images, it is assumed that the tracers follow the flow into the local flow velocity between two illuminations (Adrian, 2005).

2.3.3   Other Flow Visualization Techniques

Another popular technique for flow visualization is the Laser Doppler Velocimetry. Like PIV, this technique is non-intrusive and can measure the three velocity components of a flow field. A monochromatic laser beam is directed toward the target and the reflected radiation is collected. Based on the Doppler Effect, the change in wavelength of the reflected radiation is a function of the targeted object's relative velocity. Therefore, the velocity of an object can be acquired by measuring the change in wavelength of the reflected laser light, which is achieved by forming an interference fringe pattern (i.e. superimpose the original and reflected signals).

Similar to a PIV setup, the flow is seeded with small neutrally buoyant particles that scatter light. The particles are illuminated by a known frequency of laser light and the scattered light is detected by a photomultiplier tube (PMT). The difference between the incident and scattered light frequencies is called the Doppler shift. The local velocity of the fluid is obtained by analyzing the Doppler-equivalent frequency of the laser light scattered by the seeded particles within the flow. The main setbacks noted while using an LDV system are the need for sufficient transparency between the laser source, the target surface, and the photo detector; and the highly sensitive alignment of emitted and reflected beams on the accuracy of results.

2.4 Experimental Investigation of Flocculation using PIV

Coufort et al., (2005) conducted experiments with PIV to relate flocculation to hydrodynamics in a Taylor-Couette reactor and in a jar. The aim of the study was two-fold. The study first aimed to estimate global and local dissipation rates of turbulent kinetic energy. Secondly, the study targeted to relate floc size to hydrodynamics by performing flocculation – breakup – re-flocculation cycles in the jar and in the Taylor-Couette reactor. The jar test apparatus had a diameter of 94 mm, and a height of 145 mm, while the Taylor-Couette consisted of two concentric cylinders with a 15 mm gap in width. The flow was fully turbulent in both experiments. To study hydrodynamics experimentally, the working fluid consisted of tap water with seeding particles. PIV was used to determine the radial and tangential velocities in the horizontal plane, and the axial and radial velocities in the vertical plane. While to study floc size distributions, the working fluid consisted of a synthetic suspension of bentonite and alum was used as a coagulant.

Flocs were subjected to different hydrodynamic stresses, and aggregate cohesion and floc size were monitored. Distributions of the viscous dissipation rate of turbulent kinetic energy (ε), and the Kolmogorov micro-scale (η), and their most probable values (ε_{peak} and η_{peak}) were investigated. The same trend appeared in both reactors where the floc size depended on hydrodynamics and on initial population conditions. In addition, for the Taylor-Couette reactor, hydrodynamics was studied using CFD software Fluent, and a comparison for mean velocity components showed convergence between the PIV and CFD results. Moreover, the study showed that irrespective of the tank type, the most probable floc size is a function of (ε_{peak}). Flocs formed from aggregates as a result of the

breakup stage were smaller than flocs formed from elementary particles under the same hydrodynamic conditions. By approximating a hydrodynamic force exerted on the aggregates, an estimate of the aggregate strength was deduced, where the magnitude of this strength was dependent on floc diameter, ε_{peak}, and initial population conditions (Coufort et al., 2005).

Xiao et al., (2007) employed the PIV system to investigate the hydrodynamic properties of settling particles and aggregates in water. Experiments were conducted on a rectangular glass settling column with a length of 36 mm, a width of 33 mm, and a height of 350 mm. Polyamid seeding particles were used in the settling column experiments as flow tracers and fine particles for flocculation with falling objects. The PIV system captured thorough fluid information surrounding the falling objects. Streamlines of flow around and through a falling object could be determined, since the PIV system was able to track the paths of appropriate tracers. Hence, from these streamlines, hydrodynamic features and permeability of aggregates and particles could be defined. Conducting repeated tests for the same type of falling object (a solid sphere), the flow field surrounding the settling sphere was obtained. The study concluded that aggregates' permeable feature, being highly porous and fractal, allows flow through them which significantly improves their flocculation and their collision with surrounding particles, in addition to mass transfer into the aggregates (Xiao et al., 2007).

Zhong et al., (2011) studied and compared the size, recoverability, and fractal structure of kaolin flocs in the absence and presence of humic acid at different concentrations using PIV. Experiments were conducted on rectangular jars with 80 mm x 80 mm x 200 mm dimensions containing 1 L of kaolin suspensions, and alum was used as a coagulant. More

than 20 successive images were examined to yield a particle size distribution. The variations in floc size were continuously recorded by PIV, and thus floc breakage modes could be identified. The PIV recordings showed that at short shear time, large scale fragmentation was the main breakage mode, while at long shear time, large scale fragmentation and surface erosion existed. With increasing humic acid concentrations, the stable alum-kaolin floc size decreased. The study also concluded that reduced floc settling velocities were observed due to the decrease of the fractal dimensions of flocs as humic acid concentration increased (Zhong et al., 2011)

A similar study conducted by Xiao et al., (2011) aimed at investigating flocculation dynamics for different flocculants in various model waters with different humic acid concentrations by employing the PIV system. With the PIV and image analysis, the change in particle size distribution could be well documented. The rate of floc formation, the strength of flocs, the recovery of broken flocs, and the morphological and structural features of the flocs were characterized by means of flocculation, shear breakage and re-flocculation on a jar test device. The jars were glass rectangular tanks with 80 mm x 80 mm x 200 mm dimensions, equipped with a flat paddle mixer. Images of particles and flocs were recorded during the course of flocculation – breakage – re-flocculation, and the results were largely consistent with former particle size distribution (PSD) measurements. It was suggested that the structure of flocs in breakage became more compact with little permeability and an increase in floc compaction would cause a reduction in floc size. This contributes further explanation for the limited regrowth for most flocs. Regarding the different coagulants, alum and ferric, it was noticed that humic acid flocs had dissimilar properties with different chemical coagulants used. Alum shaped

larger flocs which tolerated a higher recovery capability after experiencing higher shear as compared to ferric (Xiao et al., 2011).

Yu et al., (2011) studied the effect of different rapid mixing times and slow stirring speeds on coagulation and floc properties. A photometric dispersion analyzer (PDA-2000) was utilized to monitor floc formation, breakage, and regrowth in an attempt to investigate underlying mechanisms. Experiments were conducted on 1 liter jar with stock kaolin suspensions and alum as a coagulant. The PDA 2000 provides a continuous monitoring technique that allows the measurement of the average transmitted light intensity (dc value) and the root mean square (rms) value of a fluctuating component which yields a ratio (rms/dc), often termed as the flocculation index. The flocculation index (FI) is strongly associated with floc size, where FI increases as aggregation occurs and flocs grow, and decreases as flocs are broken.

Rapid mixing speed was maintained at 200 rpm during and after the addition of alum, however the duration of rapid mixing was varied between 10 and 120 seconds. An increased rapid mix time resulted in a decrease of final floc size. Moreover, after floc formation, the slow stirring speed was varied between 40 and 100 rpm for a constant duration of 10 minutes, and the steady state floc size decreased with increased slow stirring speeds. Floc growth – breakage – regrowth cycles were repeated at different rapid mixing times and slow stirring speeds in order to monitor floc size and variations of the flocculation index. This study concluded that shear conditions during initial floc growth had very little bearing on floc size after breakage and after regrowth. Moreover, broken flocs did not fully regrow, which was expected, and coagulation efficiency was found to be related with the characteristic of flocs surface. The authors stated that more detailed

examination of the correlation between collision efficiency and surface properties of flocs must be addressed (Yu et al., 2011).

2.5   CFD and Flow Simulation

CFD is derived from the disciplines of fluid mechanics and heat transfer. In the beginning, CFD was only known in the high technology engineering areas such as aeronautics and astronautics. Yet, CFD rapidly became a methodology adopted for solving complex problems in modern engineering practice such as chemical, civil, and environmental engineering. The three main disciplines involved in CFD are engineering (fluid dynamics), mathematics, and computer science. CFD is particularly dedicated to fluids that are in motion (fluid dynamics), and how the behavior of fluid-flow influences processes that may include heat transfer and possibly chemical reactions in combusting flows. Moreover, fundamental mathematical equations are used to describe the physical characteristics of the fluid motion, usually in partial differential form, which govern a process of interest and are often called governing equations in CFD. Computer scientists using high-level computer programming languages convert the equations into computer programs in order to solve these mathematical equations. The computational part essentially means the study of the fluid flow using numerical simulations, which comprises employing computer programs or software packages performed on high-speed digital computers to attain the numerical solutions.

Conventionally, both analytical and experimental methods have been used to study the various aspects of fluid dynamics and to assist engineers in the design of equipment and industrial processes involving fluid flow and heat transfer. However, the numerical aspect has emerged as another viable approach. The trend is clearly toward greater reliance on

23

the computational approach for industrial designs, particularly when the fluid flows are very complex.

CFD complements experimental and analytical approaches by providing an alternative cost-effective means of simulating real fluid flows. Particularly, CFD substantially reduces lead times and costs in design and production compared with experimentally based approaches and offers the ability to solve a range of complicated flow problems where the analytical approach is lacking. These advantages are realized through the increasing performance power of computer hardware and its declining costs.

Aside from its advantages, there are inherent limitations of applying CFD. Numerical errors exist in computations, consequently there will be differences between computed results and reality. Visualization of numerical solutions using vectors, contours, or animated movies of unsteady flows is considered to be the most effective approach of interpreting the huge amount of data generated from the numerical calculation. Any numerical result obtained must always be carefully examined and analyzed. Critical judgments must be made regarding the computed results (Tu et al., 2013).

CFD is based on the governing equations of fluid dynamics which represent mathematical statements of the conservation laws of physics. The following physical laws are adopted:

1. Mass is conserved for the fluid.

2. Newton's second law: The rate of change of momentum equals the sum of forces acting on the fluid.

3. First law of thermodynamics: The rate of change of energy equals the sum of the rate of heat addition to the fluid and the rate of work done on the fluid.

2.5.1   Equations Governing Fluid Transport

1.   The Continuity Equation

The law of conservation of mass is pertinent to fluid flow where matter may be neither created nor destroyed. For an incompressible flow, we can represent the continuity equation in two dimensions as follows:

$$\frac{\partial u}{\partial x} + \frac{\partial v}{\partial y} = 0$$

This principle of mass conservation as applied to the whole domain in one dimension is also applicable to any small control volume that is used in CFD to numerically solve the partial differential equations. In two dimensions, the mass flow may not be conserved in one direction but, overall it will be conserved throughout the control volume by either removing or adding the mass in the other direction.

2.   The Momentum Equation

Newton's second law of motion states that the sum of forces acting on the fluid element equals the product of its mass and the acceleration of the element. The following equations are derived from Newton's second law, and describe the conservation of momentum in the fluid flow, also known as Navier-Stokes equations:

$$\frac{\partial u}{\partial t} + u\frac{\partial u}{\partial x} + v\frac{\partial u}{\partial y} = -\frac{1}{\rho}\frac{\partial p}{\partial x} + v\frac{\partial^2 u}{\partial x^2} + v\frac{\partial^2 u}{\partial y^2}$$

$$\frac{\partial v}{\partial t} + u\frac{\partial v}{\partial x} + v\frac{\partial v}{\partial y} = -\frac{1}{\rho}\frac{\partial p}{\partial y} + v\frac{\partial^2 v}{\partial x^2} + v\frac{\partial^2 v}{\partial y^2}$$

Where v is the kinematic viscosity ($v = \mu/\rho$)

3. The Energy Equation

The equation for the conservation of energy is derived from the consideration of the first law of thermodynamics as stated above. In most practical fluid-engineering problems, the local time derivative of pressure $\partial p/\partial t$ and the dissipation function Φ can be neglected. Also, assuming that the temperature is invariant along the z direction and the thermal conductivity k is constant, the equation for the conservation of energy in two dimensions can be expressed as:

$$\frac{\partial T}{\partial t} + u\frac{\partial T}{\partial x} + v\frac{\partial T}{\partial y} = \frac{\lambda}{\rho C_p}\frac{\partial^2 T}{\partial x^2} + \frac{\lambda}{\rho C_p}\frac{\partial^2 T}{\partial y^2}$$

4. The Additional Equations for Turbulent Flow

Most flows of engineering significance are turbulent. Small disturbances in the fluid streamlines of a laminar flow can lead to a random state of motion i.e. a turbulent condition. Turbulence depends on the ratio of inertia force to viscous force, which is indicated by the Reynolds number. At low Reynolds numbers, inertia forces are smaller than viscous forces, and the naturally occurring disturbances are dissipated away. The flow remains laminar. While at high Reynolds numbers, the inertia forces are sufficiently large to amplify the disturbances, and a transition to turbulence occurs. Hence, the motion becomes naturally unstable even with constant boundary conditions, where velocity and all other flow properties vary in a random way.

Turbulence is associated with the existence of random fluctuations in the fluid. The random nature of flow precludes computations based on the equations that describe the fluid motion. Although the conservation equations remain applicable, the dependent

variable, such as the transient velocity distribution must be interpreted as an instantaneous velocity—a phenomenon that is impossible to predict, as the fluctuating velocity occurs randomly with time. Instead, the velocity can be decomposed into a steady mean value $\bar{u}$ with a fluctuating component u'(t) superimposed on it: u(t) = $\bar{u}$ + u'(t) (Tu et al., 2013).

2.5.2   Modeling Turbulence

In principle, turbulence is described by the Navier-Stokes equations stated earlier. However, in most situations it is impossible to resolve the wide range of scales in time and space by Direct Numerical Simulation (DNS) since the CPU requirements would exceed the available computing power for any foreseeable future. Consequently, averaging procedures have to be applied to the Navier-Stokes equations to filter out all or at least parts of the turbulent spectrum. The most widely applied averaging procedure is Reynolds averaging which is time-averaging of the equations, resulting in the Reynolds Averaged Navier-Stokes (RANS) equations.

Applying RANS, all turbulent structures are eliminated from the flow and a smooth variation of the averaged velocity and pressure fields can be obtained. Nevertheless, the averaging process introduces additional unknown terms into the transport equations such as Reynolds Stresses and Fluxes, which must be provided by suitable turbulence models. The quality of the simulation can depend crucially on the selected turbulence model.

An alternative to RANS are Scale-Resolving Simulation (SRS) models. With SRS methods, at least a portion of the turbulent spectrum is resolved in at least a part of the flow domain. The most well-known method for such purposes is Large Eddy Simulation (LES). As all SRS methods require time-resolved simulations with relatively small time steps, it is important to understand that these methods are substantially more

computationally expensive than RANS simulations (ANSYS Fluent User's Guide, 2013). ANSYS Fluent provides various choices of turbulence models, and the adopted ones for this research are discussed in coming chapters.

2.6   Numerical Modeling of Flocculation using CFD

CFD has been a useful and valuable tool in understanding typical hydrodynamics of flow processes in structures, however, flocculation is a complex process that encompasses computations at an excessive degree of complexity and improvements in CFD are essential (Bridgeman et al., 2009). At a water treatment plant, the flocculation process is achieved by either mechanical or hydraulic flocculators. In mechanical flocculators, the shear stress is generated by an agitator which results in a rotating flow. The modeling of rotating flows in mechanical flocculators is necessary, and it was traditionally accomplished by applying experimentally acquired velocity data in the outflow of the impeller.

Explicit calculations of the flow pattern in the vicinity of the blades by the use of CFD models has replaced the traditional experimental method, especially in conditions where experiments cannot be conducted. The sliding mesh method is one of the methods adopted in CFD to calculate the flow field in rotating flow settings as in mechanical flocculators. In this method, two regions are established in the tank, namely the impeller region and the tank region (including the liquid itself, the tank walls and bottom, and the baffles), and each region is treated separately. A different approach for modeling the mixing process is by referring to the Multiple Reference Frames (MRF) method. In this method, one stationary reference frame is selected for the vessel walls, and a second reference frame related to the rotating shaft and impeller. For steady state applications,

the MRF method is very useful and practical, while for unsteady states, the sliding mesh method is preferred.

Swirling flow conditions often arise in the mixing process of mechanical flocculators. This presents anisotropic turbulence conditions which creates some challenges. CFD practitioners commonly use two-equation models which are based on the assumption that turbulence is isotropic, and therefore difficulties are tackled when modeling swirling flows. Since swirling flows are anisotropic in nature, therefore other models such as the Reynolds Stress Equation Model (RSM) are employed to capture this anisotropic turbulence (Bridgeman et al., 2009).

As previously stated, the average velocity gradient was considered as insufficient to characterize the mixing flow in flocculation processes, and therefore CFD codes rely on the local velocity gradient:

$$G_L = \sqrt{\frac{\varepsilon}{v}}$$

Within the water treatment industry, the use and application of CFD has increased tremendously since 1995 until today. CFD has been used to demonstrate the limitations of the average velocity gradient as a design parameter for flocculators. Moreover, CFD is used as a tool to model and study flow fields within jar testers, laboratory scale flocculators, and full scale flocculators.

Bridgeman et al., (2010) modeled and studied the flow field within a jar test apparatus and within full scale flocculators using the CFD code Fluent v6. The authors focused their study on further understanding floc formation and breakage mechanisms. This was

achieved by concentrating on the development and application of simulation techniques and the analysis of computational models. This literature review focuses on the CFD modeling within the full scale flocculator only. The said flocculator consists of three identical rectangular cells 6.4 m in width, 7.0 m in length and 4.75 m deep each. A 6.0 m diameter rake paddle with four blades on each side was operated at different rotating speeds to stir the water.

The authors state that such a tapered system provides an enhanced flocculation process. In the first cell, high density flocs are produced quickly, while in the second cell floc growth is stimulated. Finally, in the third cell, a minimum amount of turbulence is generated which is enough to maintain the suspension yet avoid floc breakage. One vessel was modeled at a time, in order to reduce computational expenses, and three mixing speeds of 3.2 rpm, 2.4 rpm, and 1.6 rpm were simulated. At a mixing speed of 2.4 rpm, simulated velocity contours for one quadrant of the mechanical flocculator at a depth of 3.0 m indicate that the highest velocities are located towards the tips of the paddles. The velocity within the vessel varies between 0 and 0.89 m/s.

The average and maximum local velocity gradients, G_{Lave} and G_{Lmax} respectively, vessel average velocity gradient G_{ave}, and average turbulent eddy dissipation ε_{ave} values, were calculated for each mixing speed and flow rate. The results indicated that both the average and maximum local velocity gradients are clearly affected by the mixing speed, but are effectively independent of flow rate at each mixing speed. As the mixing speed was increased from 1.6 rpm to 3.2 rpm, the average local velocity gradient increased from 16.9 s^{-1} to 46.5 s^{-1}, while the maximum local velocity gradient increased from 268.7 s^{-1} to 832.8 s^{-1}. However, these gradients showed minimal variations for increasing flow rates

at the same rotating speed. In a previous study, Bridgeman et al., (2008) proposed that flocs formed from upland water can withstand velocity gradient values up to 150 s^{-1}. The distribution of local velocity gradient values within the mechanical flocculator indicates that the vast majority of the velocity gradients are at or below the postulated threshold. Consequently, this shows that the magnitudes of the velocity gradients induced are satisfactory for sufficient flocculation (Bridgeman et al., 2010).

Chapter Three

The Laboratory Scale Paddle Flocculator

3.1   Flocculation Practice

In principle, the mixing required for flocculation is provided by horizontal and vertical mechanical devices as well as arrangements that promote turbulence by hydraulic means alone. It has also been shown that flocculation benefits from compartmentalization. The first flocculators comprised of large and flat vertical blades rotating in cylindrical tanks made to imitate large jars. Today's flocculation installations can be categorized into two groups: mechanical and hydraulic. In mechanical flocculation, horizontal paddles and vertical turbines have become the most common configurations. While in hydraulic flocculation no particular arrangement dominates. Crittenden (2012), addresses the main differences between the three process approaches as summarized in table 1.

Table 1: Comparison of Flocculator Types (Crittenden, 2012)

Process	Horizontal Shaft with Paddles	Vertical Shaft Turbines	Hydraulic Flocculation
Type of Floc Produced	Large and Fluffy	Dense, Small to Mediuam and	Very Large and Fluffy
Head Loss	None	None	0.05 – 0.15 m
Operational Flexibility	Good, limited to low $\overline{G}$	Excellent	Moderate to Poor
Capital Cost	Moderate to High	Moderate	Low to Moderate
Construction Difficulty	Moderate	Easy to Moderate	Easy to Difficult
Maintenance Effort	Moderate	Low to Moderate	Low to Moderate
Compartmentalization	Moderate	Moderate	Excellent

Vertical turbines are more commonly used in direct filtration systems and can be replaced or maintained while the process is operating. Furthermore, hydraulic flocculation is particularly popular in locations with poor access to resources and trained personnel for maintenance and operation. However, horizontal shaft paddles are more common in conventional treatment which include sedimentation (Crittenden, 2012).

3.2   Design Principles of Paddle Flocculators

The basic design criteria for mechanical flocculators are the Camp and Stein RMS velocity gradient and the hydraulic detention time. In 1943, Camp and Stein developed the basic theory of power input for mixing where the velocity gradient is proportional to the amount of energy dissipated in the fluid. The difference in velocity between adjacent layers of the fluid is known as a velocity gradient. They adopted a force balance and a power balance to relate the velocity gradient to the power input in a basin. Requirements of hydraulic detention time depend more on the downstream process than on the means of flocculation. Rather shorter flocculation times, 10 to 20 minutes, are usually needed with direct filtration than for conventional treatment which require 20 to 30 minutes.

Crittenden (2012), discussed the design process as follows:

- Determining the water power input required to achieve a $\overline{G}$ value

$$\overline{G} = \sqrt{\frac{P}{\mu V}} \qquad P = \overline{G}^2 \mu V$$

In flocculators, turbulent flows normally exist. Flocculators are typically designed to have $\overline{G}t_d$ values in the range of 10^4 to 10^5, where $\overline{G}$ values may range from 10 to 60 s^{-1}, and

detention times are limited between 15 and 45 minutes. Typical values of $\overline{G}$ are 20 to 50 s^{-1}, since it is difficult to achieve 50 to 60 s^{-1} with paddle wheel flocculators.

- Determining the power input to the water by horizontal paddles

The power input imparted by horizontal paddles is dependent on the drag force and the relative velocity of the fluid with respect to the blade. The velocity of the fluid will be less than the velocity of the paddle because of slip.

$$P = \frac{C_D A_p \rho v_R{}^3}{2}$$

Where: P is the power input (N-m/s)

C$_D$ is the drag coefficient on the paddle for turbulent flow (unit less)

A$_p$ is the projected area of the paddle (m^2)

ρ is the fluid density (kg/m^3)

v$_R$ is the velocity of the paddle relative to the fluid (m/s)

Different authors discuss the velocity of the paddle relative to water in varying terminology, all stemming from the work done by Camp in 1955. Hendricks (2011) explained that since the whole water mass is subject to being set in motion by the paddle wheel, a slippage factor k is considered. k is the ratio of rotational velocity of water mass to the rotational velocity of the paddle wheel, and it is assumed to fall in the range of 0.24 to 0.32 with k = 0.25 used commonly (Hendricks, 2011).

- Determining the Reynolds number

$$Re = \frac{D_{pw}{}^2 N \rho}{\mu}$$

Where: Re is the Reynolds number (unit less)

Dpw is the diameter of the paddle wheel (m)

N is the rotational speed (s^{-1})

ρ is the fluid density (kg/m^3)

μ is the fluid dynamic viscosity $(N.s/m^2)$

3.3   Design of the Laboratory Scale Paddle Flocculator

The general procedure for paddle flocculator design was adopted as a guide for designing the laboratory scale flocculator. Numerous provisions were implemented in the design due to laboratory work restrictions. Since the flocculator was used for experimental research, the feasibility of conducting PIV experiments was also considered. The spacing restrictions dictated the volume of the flocculator. Initial provisions adopted in the design are listed below:

- The flocculator consists of only one compartment or stage.

- The flocculator is a rectangular box with a top opening.

- A minimum freeboard of 40 cm is needed.

- Two paddle wheels are mounted on the horizontal shaft, each having four arms.

- Arms are welded into the shaft such that all consecutive arms are perpendicular.

35

- The paddle wheel design includes three blades per arm.

- The minimum length of an individual arm is 40 cm.

- The minimum edge to edge clearance between the paddle wheels is 10 cm.

- The minimum clear spacing between a blade and the base is 10 cm.

- The minimum clear spacing between a blade and a wall is 10 cm.

- The minimum clear spacing between consecutive blades on an arm is 10 cm.

The dimensions of the flocculator are summarized in table 2, while detailed calculations are presented in Appendix B.

Table 2: Flocculator Dimensions

Depth	Length	Width
150 cm	140 cm	120 cm

With a freeboard of 40 cm, the effective depth of the flocculator is 110 cm. A 4 cm diameter horizontal shaft extending over the length of the flocculator is fixed at a height of 60 cm from the bottom of the flocculator to ensure sufficient clear spacing between the paddles and the base. The flocculator has 1.5 cm thick plexiglass walls, and a total effective volume of 1.763 m^3.

3.4 The Actual Flocculator

The design stated above along with drawings were used to manufacture the flocculator. Due to some limitations in manufacturing and assembly, minor errors were incorporated and the drawings below show the detailed dimensions and configuration.

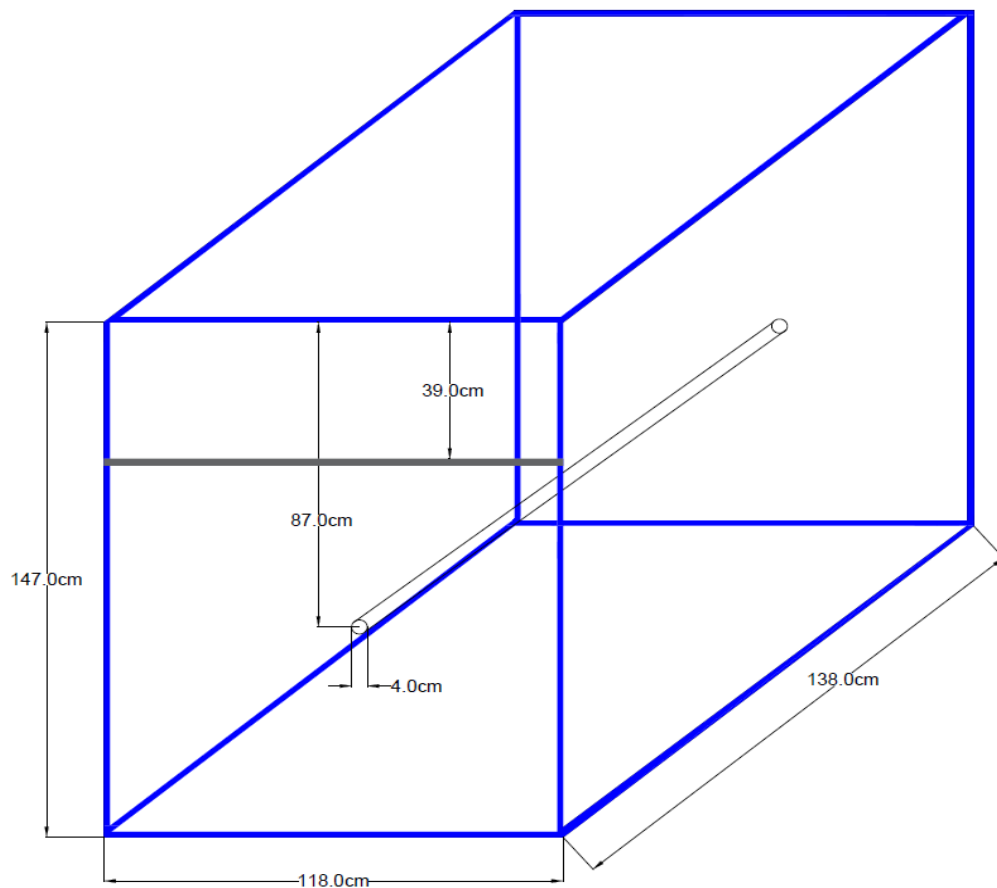### 3.4.1 Flocculator 3D View

Figure 2: 3D View Schematic of the Flocculator

- An electric motor with a chain and gears rotates the mixer.
- The electric motor is connected to a control unit, to input the required rotating speed of the mixer.

37

3.4.2 Flocculator Front and Side View
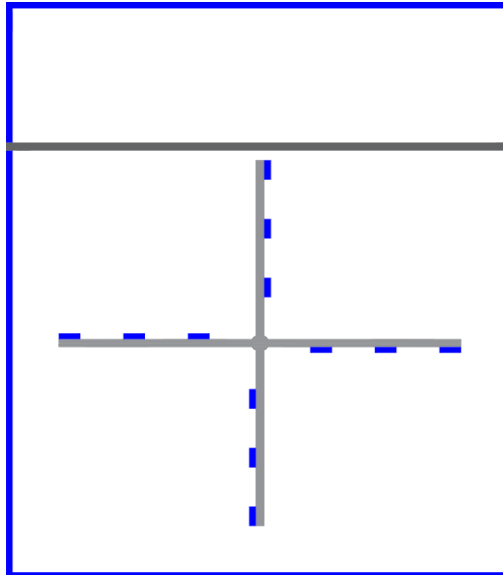
Figure 3: Front View Schematic of the Flocculator
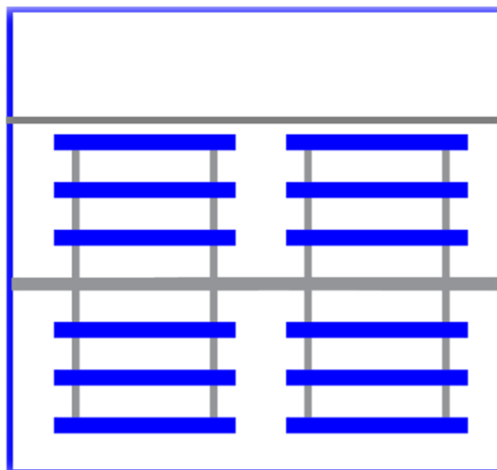
Figure 4: Side View Schematic of the Flocculator

- Blades are plexiglass with a thickness of 1.5 cm.

- Each arm consists of two steel axes spaced 40 cm apart.

- Blades extend 5 cm on each side of the arm axes.

3.4.3 Flocculator Top View

Figure 5: Top View Schematic of the Flocculator

- The height at which all blades are fully submerged in water is 108 cm from the

  base of the flocculator thus ensuring a freeboard of 40 cm approximately.

3.4.4 Flocculator Flow

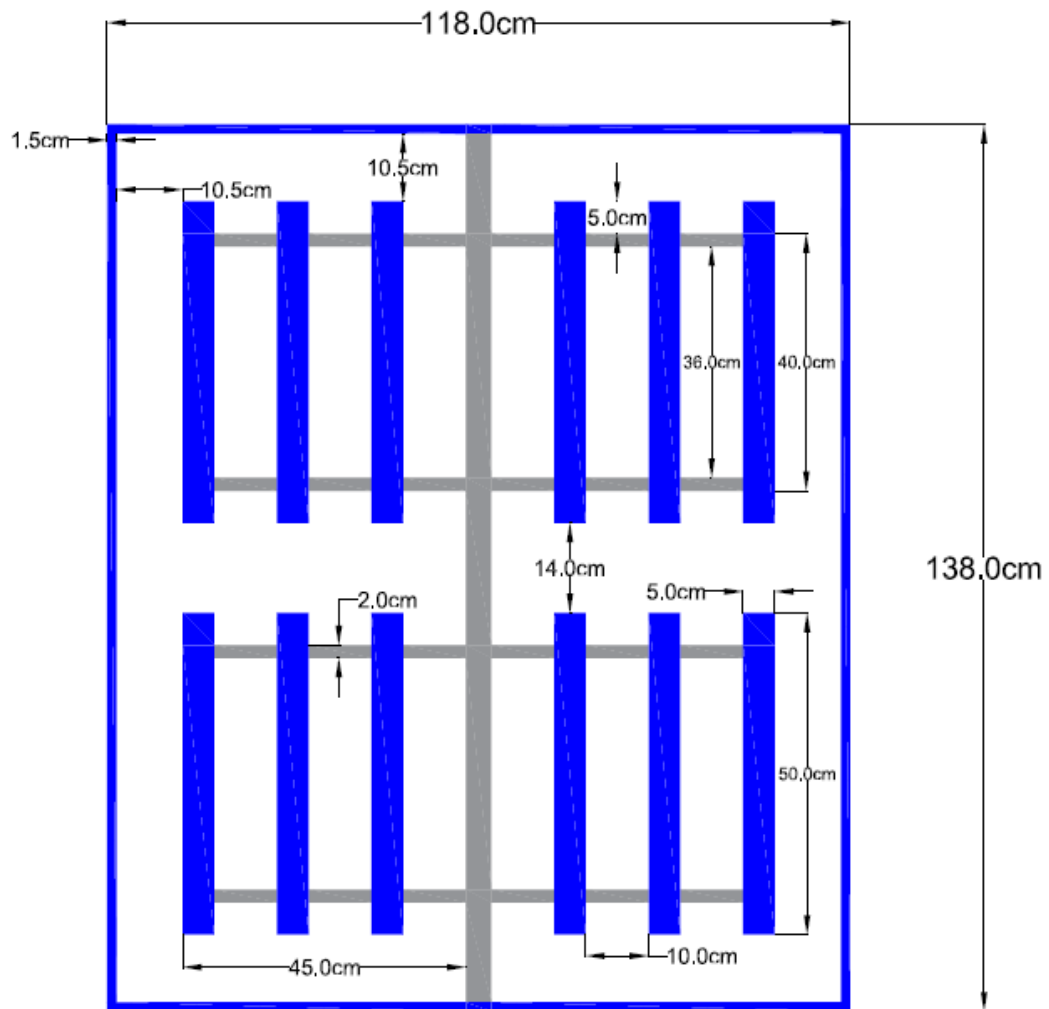The rotational speed required in flocculation processes ranges between 2 rpm and 6 rpm. For the purpose of this research, experiments were conducted at the most common speeds which are 3 rpm and 4 rpm. Therefore the power input, velocity gradient, and Reynolds number is calculated for the flow inside the flocculator as per the design formulas mentioned earlier. Table 3 summarizes the parameters required, while detailed calculations are presented in Appendix B.

Table 3: Parameters for Flow Calculations

Parameter	Value
C_D	1.3
A_p	0.2 m^2
ρ	1000 kg/m^3
v_R	0.75v_p
V	1.763 m^3
μ	0.001 N.s/m^2
D_{pw}	0.94 m

- A_p is one third of the blades' area

- A slippage factor of 0.25 is adopted as per most designs. That is, the speed of the blades relative to the water will be 0.75 of the blade speed.

The results of the calculations at 3 rpm and 4 rpm are summarized in table 4.

Table 4: Flow Parameters at 3 rpm and 4 rpm

	3 rpm	4 rpm
P (watts)	0.2	0.5
$\overline{G}$ (s^{-1})	11	17
Re	44,180	58,910

The flow inside the laboratory scale flocculator truly represents the flow inside a compartment of a flocculation basin at a drinking water treatment plant. For both rotating speeds, the $\overline{G}$ values are above 10 s^{-1}, and the Reynolds number indicates turbulent flow.

Chapter Four

Methodology

In this chapter, the experimental investigation of flow structures and velocity fields surrounding the blades of the flocculator is discussed in the first part. While in the second part, the CFD models generated to simulate the mixing flow field are covered.

4.1   PIV Experiments

4.1.1   Experimental Setup

The experimental setup consists of the laboratory scale paddle flocculator, the LaVision PIV system (2017), and an Arduino laser-sensor external trigger.

1.   Laboratory Scale Paddle Flocculator

The detailed design of the flocculator was previously discussed, and comprehensive drawings showing its configuration were presented in figures 2, 3, 4, and 5.

2.   LaVision PIV System

The components of the PIV system used to conduct the experiments are as follows:

1. Illumination System: double pulsed Nd: YAG laser
2. Image Acquisition Unit: Imager Pro X 2M CCD camera
3. System Calibration Tool: 3D Type 11 calibration plate
4. Data Acquisition and Processing Unit: DaVis 8.4 software

The specifications and characteristics of each of the PIV system components stated above are thoroughly discussed in Appendix A, and the basic layout of a PIV system is illustrated below.
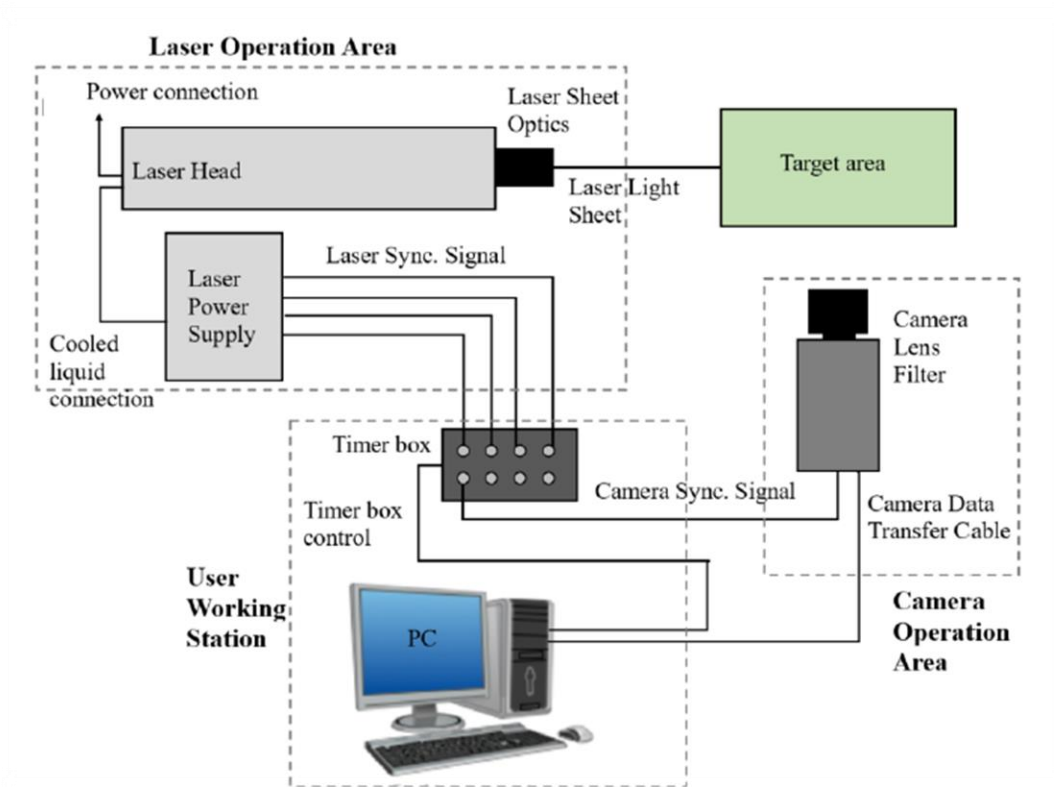

Figure 6: Layout of a PIV System (extracted from LaVision PIV Manual)

The laser operation area and the camera operation area are both connected to the Timer Box or Programmable Timing Unit which itself is connected to the user working station i.e. the data acquisition and processing software. The PTU acts as the orchestrator of a PIV system. The target area in this case is the flocculator itself, in addition an external trigger is connected to the PIV system through the PTU which is discussed in detail next.

3. Arduino Laser-Sensor External Trigger

A PIV recording initiates with a trigger source inside the programmable timing unit (PTU) which is responsible for the operation and synchronization of the laser light source and the camera. Based on the experimental setup, the trigger source is determined. In the case of this research, the PIV system is used to obtain recordings as the flocculator is operating at a specific rotating speed. The aim of such recordings is to visualize the velocity field at a plane perpendicular to the blades located at mid-length of the blades.

Deciding on the trigger source originates by questioning if the internal frequency controlled trigger source is applicable on the experimental setup and if its use yields the required results. Since time averaged PIV recordings are needed to reveal the velocity field at the plane of interest, this means consecutive recordings must be acquired where the blades are in the same position in each recording.

Using the internal trigger source involves obtaining subsequent images for a certain duration of time where the trigger rate and recording rate are to be determined. Then, extracting from all the recorded images the ones that show the blade of interest at the same location. Extracting the needed data from large sets would require a lot of time and averaging the results would not be representative of the velocity field due to numerous human and instrumental errors.

From this determination, the need of an external trigger was evident. The PIV system requires an external trigger to be a TTL signal with positive logic (0 V $\rightarrow$ 5 V) and a gate of $1 \geq \mu s$. Noting the geometry and structure of the laboratory scale flocculator, a laser-sensor external trigger was the most convenient.

The external trigger setup consists of the following:

- Arduino laser transmitter module

- Arduino laser sensor receiver with a working voltage of 5 V

- BNC cable and wire signal
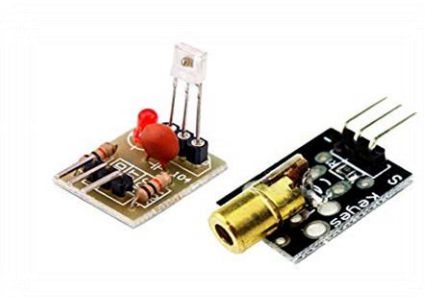
- 5 V – 2 A adapter

Figure 7: External Trigger Laser and Receiver

This type of external trigger was adopted since it is a non-intrusive trigger having no impact on the mixing flow inside the flocculator.

The sensor has a high output level when it receives a signal, and a low output level when it does not receive a signal. The 5 V adapter is used as a power supply for the system. The laser must be located on one side of the flocculator (along its width) and the laser sensor receiver to be situated on the other side. The laser produces a red light beam which hits the plexiglass wall of the flocculator perpendicularly. This incident beam then refracts in water and emerges through the opposing plexiglass wall in a straight manner. The difficulty here lies in situating the sensor receiver due to the refraction of the laser light in water. The path of the laser light beam to reach the sensor is interfered by the rotating arms of the paddle wheel flocculator. As the flocculator operates, and for one full rotation,

the red laser light is obstructed four times, once by each arm, where the steel paddles are obstructing the path of the laser light beam and not the plexiglass blades.

The sensor receiver is connected to the programmable timing unit of the PIV system by means of a BNC cable which is connected to the trigger adapter of the PTU. When the sensor receives a signal, its output is 5 V and the system is not triggered. When the sensor does not receive a signal due to the obstruction of the laser light beam by the arm of the mixer, its output is 0 V and the system is triggered.

The trigger source is selected as external random since the laser sensor receiver connected to the PTU functions as an external random trigger. For every trigger the PTU receives, it commands the devices connected to it i.e. the laser light source and the CCD camera to take a recording.

4.1.2   Experimental Procedure

In order to conduct accurate experiments which yield reliable and repeatable results, a systematic way of work was adopted ensuring that all the experimental work conditions were met. These conditions are listed and discussed below.

1. Mixing Flow conditions

This is accomplished by filling the flocculator with domestic water, which contains impurities, such that the entire paddle wheel is submerged at all times. Moreover, the flocculator is allowed to operate at slow mixing speeds (3 rpm or 4 rpm) for a short period of time (5 – 10 minutes) to normalize the flow. The design of the flocculator previously discussed and verified ensures that the mixing flow inside the basin is representative of that in flocculation processes.
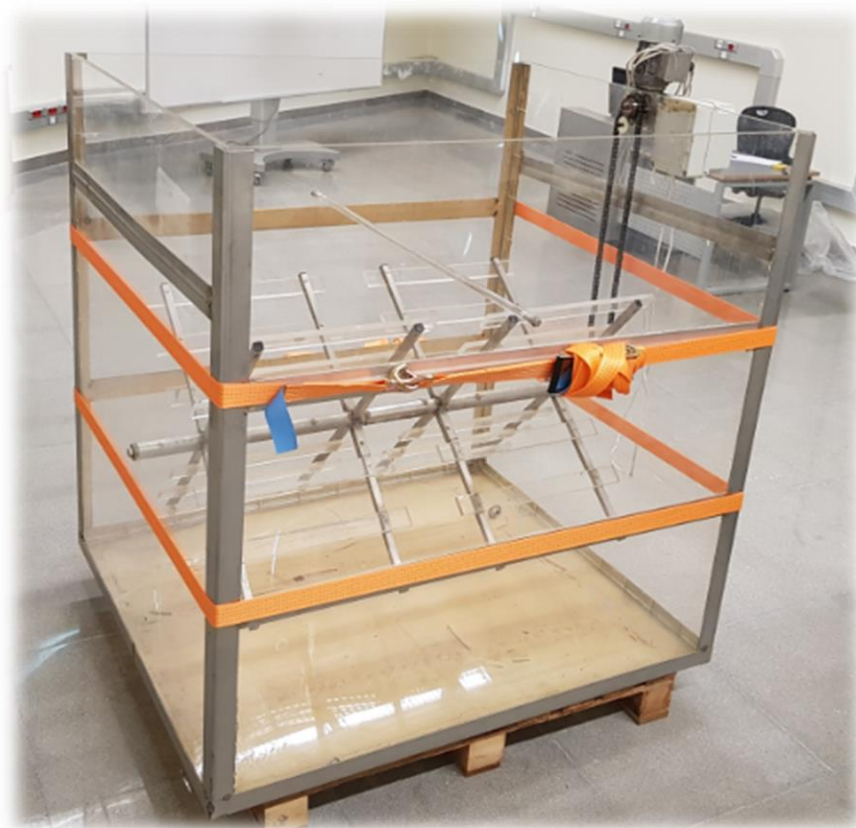
Figure 8: Photo of the Laboratory Scale Paddle Flocculator

2. Calibration conditions

The calibration plate is submerged into the flocculator and placed on one of the blades of interest. Calibration is completed after filling the flocculator with water in order to account for the same refractive index field, as well as the same shape of the flocculator plexiglass wall which might bend slightly due to the hydrostatic pressure exerted by the water. For the purpose of this study, a 1.5 cm thick aluminum plate was utilized and placed on top of the flocculator (extending over its width) to position the light sheet optics of the PIV laser. The laser sheet must be directed exactly on the calibration plate creating a planar light sheet at its face. The calibration process is accomplished according to the standard procedure described in Appendix A.
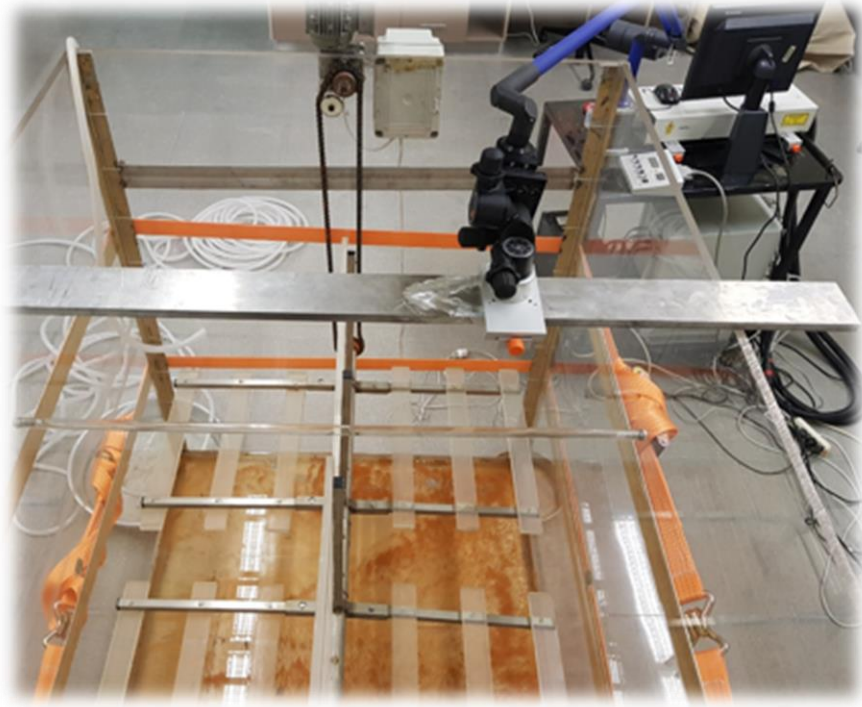
47

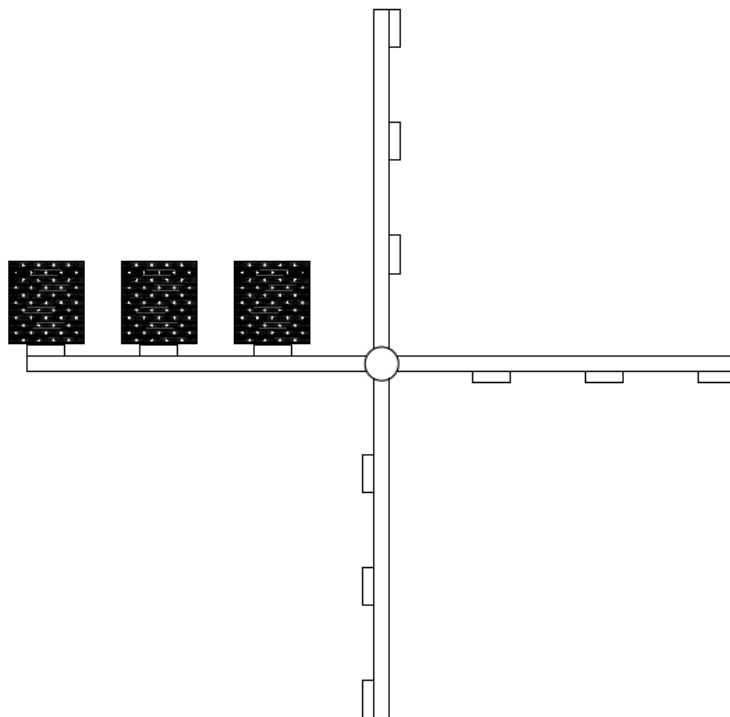**Figure 9: Photo of the PIV Laser Mounted Over the Flocculator**

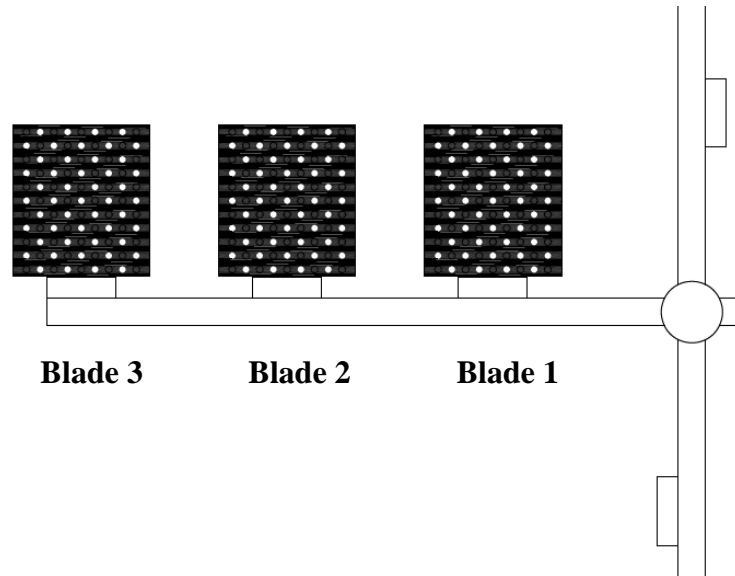**Figure 10: Schematic of Calibration Plate Locations on Mixer**

Figure 11: Schematic of Calibration Plate on Blades of Flocculator

3. Trigger Source conditions

The location of the Arduino laser transmitter and that of the laser sensor receiver is calibrated such that the sensor receives a full signal when its path is free, and no signal when its path is obstructed by the paddles.
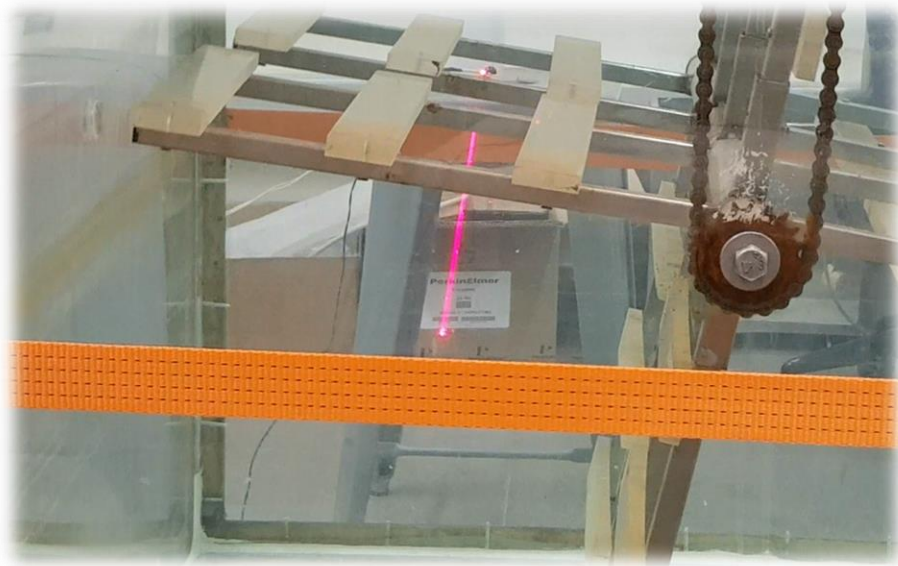

Figure 12: Photo of External Trigger Laser Path Unobstructed

Figure 13: Photo of External Trigger Laser Path Obstructed by Flocculator Arm

4. PIV conditions

For PIV recordings, the time separation between two laser pulses dt was adjusted between 6900 and 7700 μs by allowing a minimum particle shift of 5 pixels. Tests concerning the number of images needed to get accurate time averaged measurements were performed. Vector statistics of samples containing 40, 50, 60, 80, 100, 120, 160, 200, 240, and 280 images were compared. It was concluded that a sample size of 240 images produce a stable time averaged result noting that each image consists of two frames. Therefore, experiments were performed with 240 images for the best measurement accuracy.

Since the flow is turbulent in the flocculator, small interrogation window sizes are required with a high number of particles to resolve the small turbulent flow structures. Decreasing size multi-pass iterations were applied with the cross correlation algorithm to ensure accuracy. An initial interrogation window size of 48 x 48 pixels with a 50 % overlap and 1 adaptation pass followed by a final interrogation window size of 32 x 32

pixels with a 100 % overlap and 2 adaption passes were applied. Furthermore, glass hollow spheres were used as seeding particles in the flow whereby a minimum of 10 particles were allowed per interrogation window.

In addition, the following parameters were adjusted for the PIV experiments:

- Camera mode: double frame and two reference times (basis of operation of PIV)

- Trigger source: external random (to read the trigger from the laser-sensor system)

- Reference time: describes the time between the PTU trigger and the moment when the image is taken or illuminated by a pulse light source. This is limited by the intrinsic delay of all activated devices, and was regulated as 3 ms.

- Devise offset: allows to adjust the timing if one or more of the devices have internal delays that are different from the default values. The device offset option is only available for the Imager Pro X camera which means the camera must be synchronized with the laser light source. It was calibrated as 5 μs.

- Light source power: since a double pulse Nd: YAG laser is used, the power of each laser pulse must be identified. In general, the light source power of the first pulse must be stronger than that of the second pulse in order to obtain visible images in both the first and second frame. Light source power was calibrated as 100 % for pulse one and 40 % for pulse two.

- The trigger rate and recording rate are overridden by the use of an external trigger.

After all parameters have been adjusted, image acquisition initiates as soon as the first arm of the paddle wheel obstructs the laser signal, triggering the PIV system to record the first image. All images are recorded accordingly.
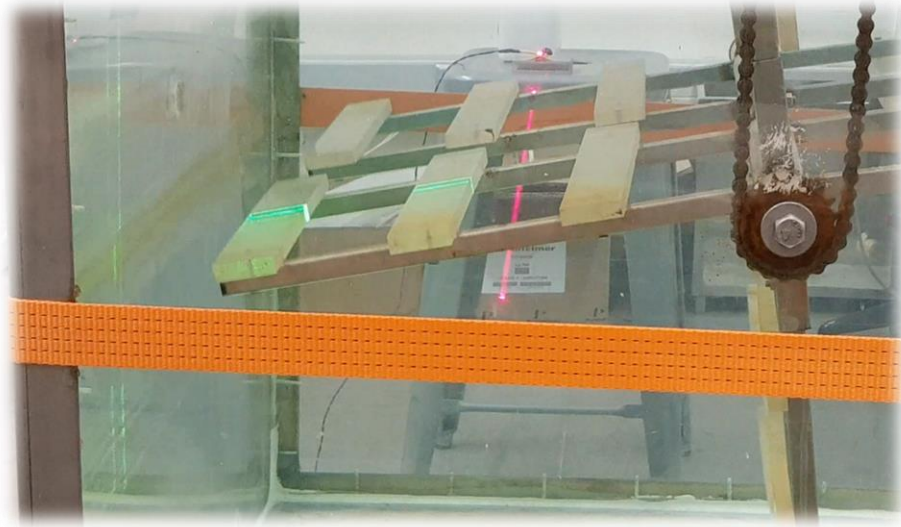
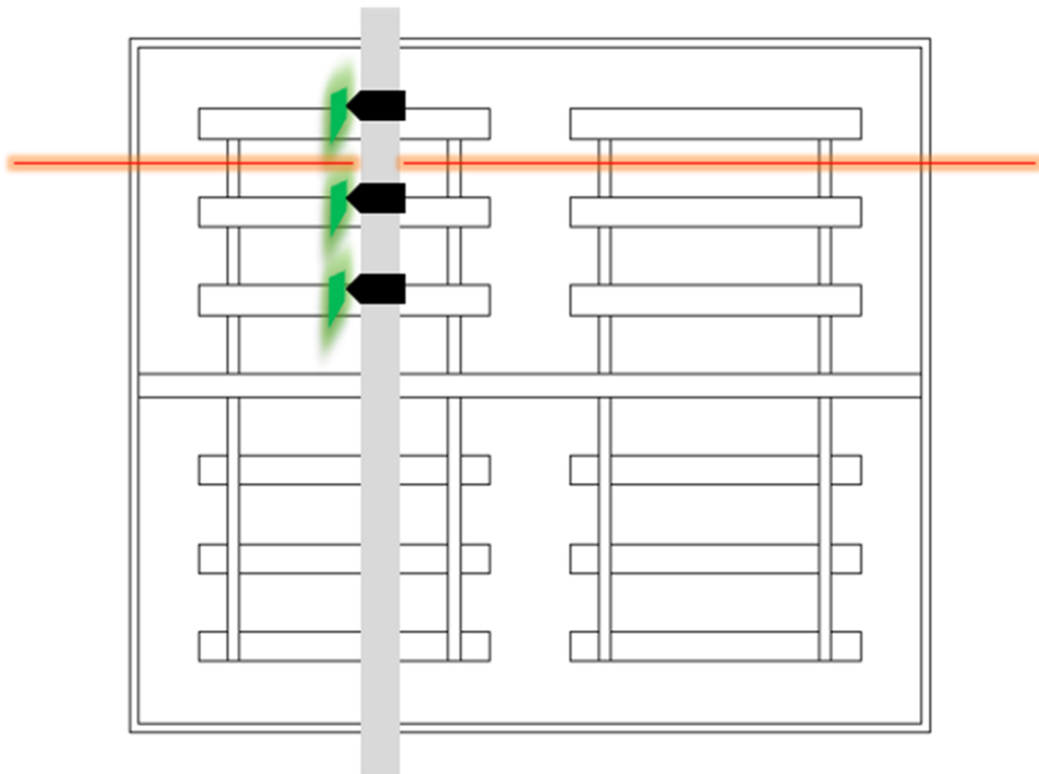**Figure 14: Photo of PIV System Triggered after Laser Path was obstructed**

Figure 15: Flocculator Schematic Showing the Location of PIV Images Recorded

4.2 CFD Models

The commercial CFD software package ANSYS Fluent v 19.1 was used to develop the 3D models and to solve the governing flow equations. The methods used to develop the models are discussed in this section.

4.2.1 Geometry

A 3D model was generated of the laboratory scale paddle flocculator. The model was formed as a rectangular box consisting of two paddle wheels fixed on a horizontal shaft identical to the laboratory prototype. The model internal dimensions comprised of a length L = 135 cm, and a width W = 115 cm. The flocculator was modeled only up to the height at which it would be filled with water while conducting the experiments, excluding the freeboard. Thus, the height used in generating the model was H = 108 cm. The horizontal shaft, paddle wheel axes, and blades were referred to as one body, named as mixer. A horizontal cylindrical-shaped plane was added encompassing the mixer. The generation of the cylindrical plane is needed to achieve rotation of the entire mixer in the setup phase, and to simulate the rotational flow field inside the flocculator.

The model geometry consists of two domains, where both are fluid. This is achieved by using the Boolean subtract function. Initially the cylinder (including the mixer) is subtracted from the box which is fluid. Then, the mixer is subtracted from the cylinder thus yielding two fluid bodies. Consequently, the two fluid bodies were the mixer and the fluid. Finally, a sliding interface was applied between the two domains, namely a box-cylinder interface and a cylinder-mixer interface (figures 16, 17, and 18).
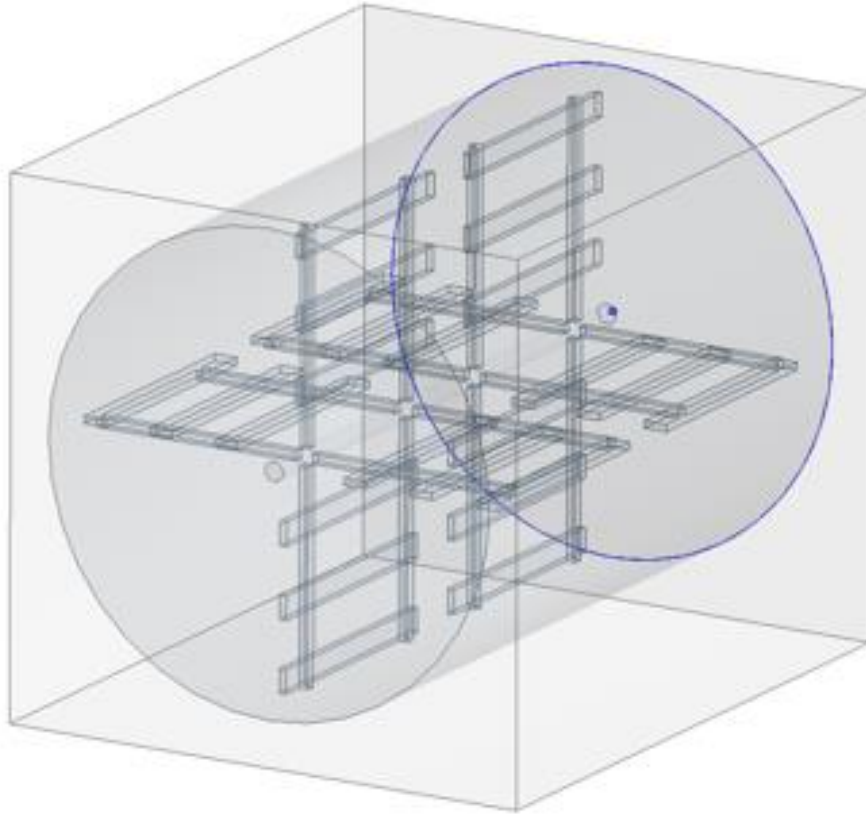
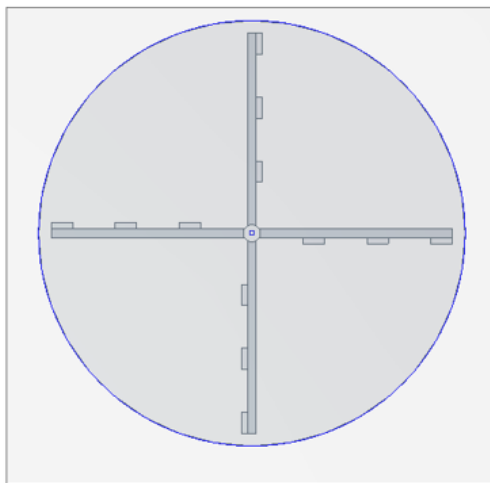**Figure 16: 3D View ANSYS Schematic of Flocculator Geometry**

Figure 17: Front View ANSYS Schematic of Flocculator Geometry
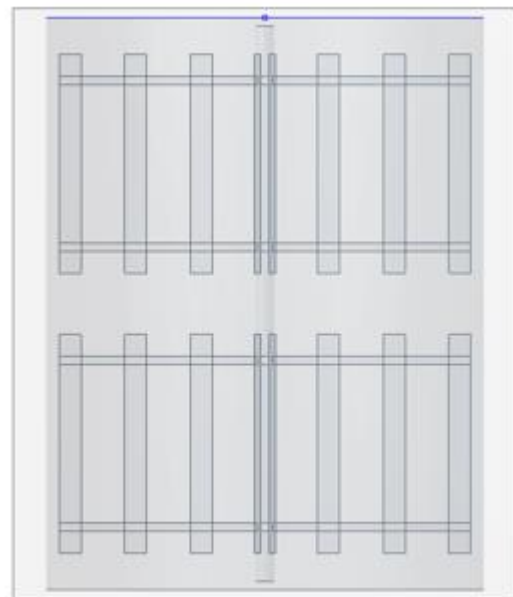

Figure 18: Top View ANSYS Schematic of Flocculator Geometry

4.2.2 Mesh

Mesh quality and size is essential in obtaining accurate results and minimizing simulation errors. A good quality mesh was achieved by maintaining good element quality, low levels of element skewness, and proper orthogonal quality. Mesh generation for the built model was completed to fit the requirements of the turbulence models which would be used in running the numerical simulations.

An unstructured mesh with inflation layers near solid surfaces was utilized. Inflation layers were created for all walls, with a growth rate of 1.2 ensuring that complex flow structures were captured, and a first layer thickness of 7 x 10^{-4} m ensuring that $y^+ \leq 1.0$. Body sizing through a patch conforming method using tetrahedrons was applied. Face sizing of the two interfaces with an element size of 2.5 x 10^{-3} m was generated. While face sizing of the mixer originated with an element size of 9 x 10^{-3} m. The original generated mesh was composed of 2,144,409 elements.
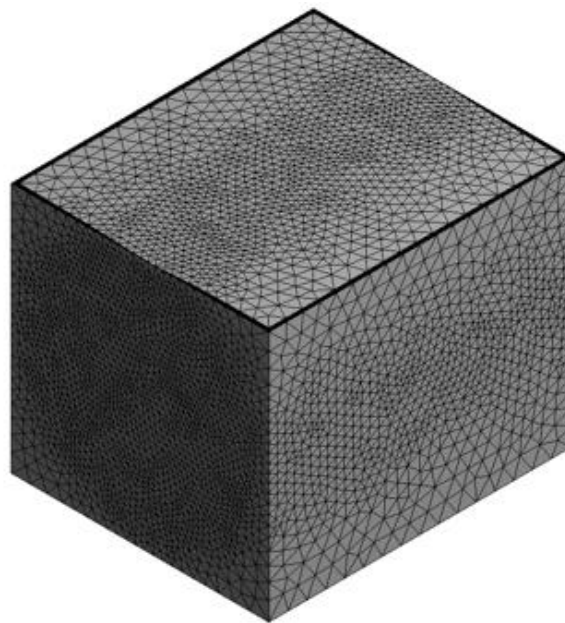

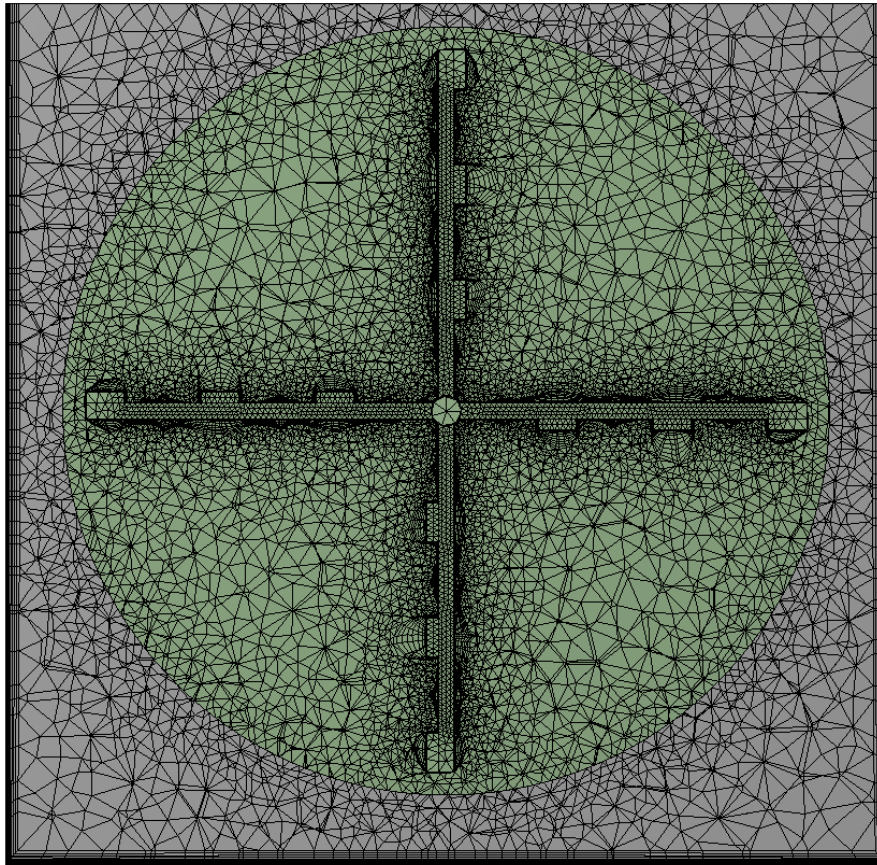**Figure 19: ANSYS Mesh of Flocculator Body**

Figure 20: ANSYS Mesh of Flocculator at Plane

4.2.3   Turbulence Models

Turbulent flows are characterized by fluctuating velocity fields. There is no single turbulence model which is universally accepted as being superior for all classes of problems. The choice of turbulence model depends on numerous considerations such as the fluid dynamics, the capabilities and limitations of the options, and the available computational resources.

Mesh considerations are essential for turbulent flow simulations, and were accordingly addressed in this study. Since there is a strong interaction between the mean flow and turbulence, numerical results for turbulent flows tend to be more subject to mesh

56

dependency when compared to laminar flows. As stated earlier, near-wall mesh guidelines were considered by applying inflation layers to all solid surfaces of the domain to ensure that $y^+ \leq 1.0$. y^+ is a geometrical quantity that is not fixed. It is a non-dimensional wall distance for a wall-bounded flow which is solution dependent.

For modeling turbulent flow inside the flocculator, the two equation k–ε turbulence model was selected as a starting baseline model. However, this model is not adequate for complex flows including rotating flows such as the case of this study. Computationally more expensive models were selected to accurately simulate the rotational flow inside the flocculator. The two CFD models adopted to numerically study the turbulent rotational flow inside the flocculator were the SST k–ω and the IDDES. Results from both models were compared with the PIV experimental results for model validation.

Firstly, the SST k–ω turbulence model was selected, since this model is the best two equation model for such flows. It accurately predicts flow separation due to adverse pressure gradients. Secondly, the widely used IDDES method of the DES model with a SST k–ω RANS model was selected. IDDES is a hybrid RANS-LES model that provides a more flexible and convenient scale resolving simulation (SRS) model. It relies on the LES models to resolve the large eddies and reverts to SST k–ω to model the small scale eddies (sub grid eddies). Statistical analysis of results obtained from simulations using SST k–ω and IDDES compared to PIV results for model validation is discussed in the following chapter.

4.2.4 Fluent Setup

A pressure based and transient solver was employed, with a gravitational acceleration of 9.81 m/s^2 in the Y direction. Regarding the cell zone conditions, as mentioned earlier the two bodies were fluid. Rotation was achieved by assigning a mesh motion to the mixer, where the rotational axis origin was the center of the horizontal shaft and the rotation axis direction was in the Z. Similar to the experimental procedure, the equivalent of a rotational speed of 3 rpm and 4 rpm was selected and entered in rad/s for the different simulations.

A mesh interface was created for the two interfaces of the model geometry, producing the two boundary zone sides. Boundary conditions for the mixer and the flocculator walls were assigned as walls, while the top opening of the flocculator was assigned as an outlet vent with a gauge pressure equal to zero. The SIMPLE scheme was used for the pressure-velocity coupling, and least squares cell based for the spatial discretization of the gradient with second order functions for all parameters.

The convergence criterion of all flow variables was a scaled residual of 1 x 10^{-3}. The maximum number of iterations per time step was 20, with a time step size equivalent to 0.5° rotation. The solution converged at the 8th iteration for the SST k–ω model and at the 12th iteration using IDDES. Also, the number of time steps was calculated such that mixer would rotate a minimum of 12 complete rotations. Data sampling for time statistics was applied after 3 rotations allowing the flow to normalize similar to the experimental procedure. Comparison of velocity contours exported at each rotation yielded precisely identical results for the last four rotations indicating that steady state was achieved. Additional revolutions did not have any effect on the averaged velocity contour.
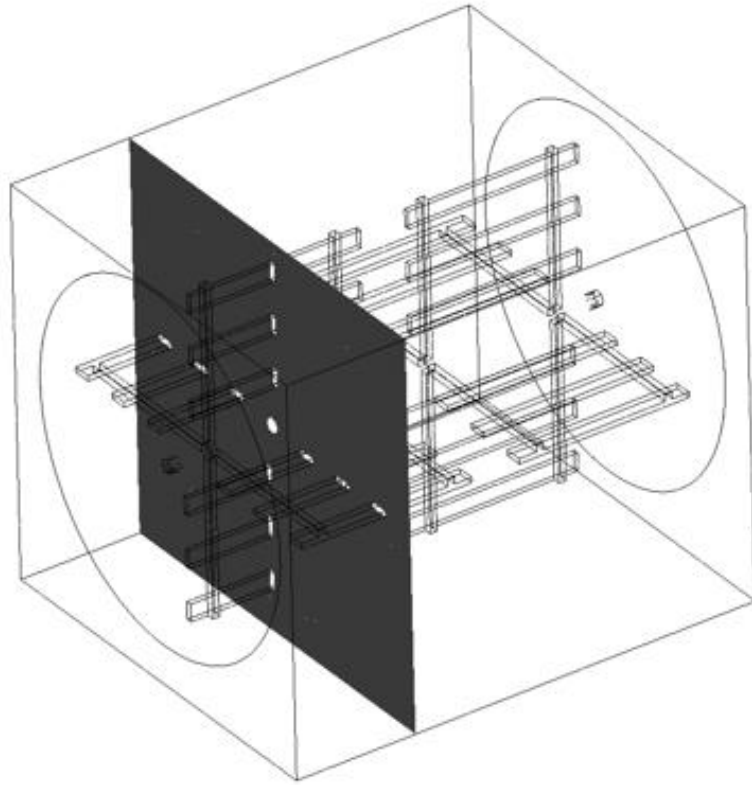
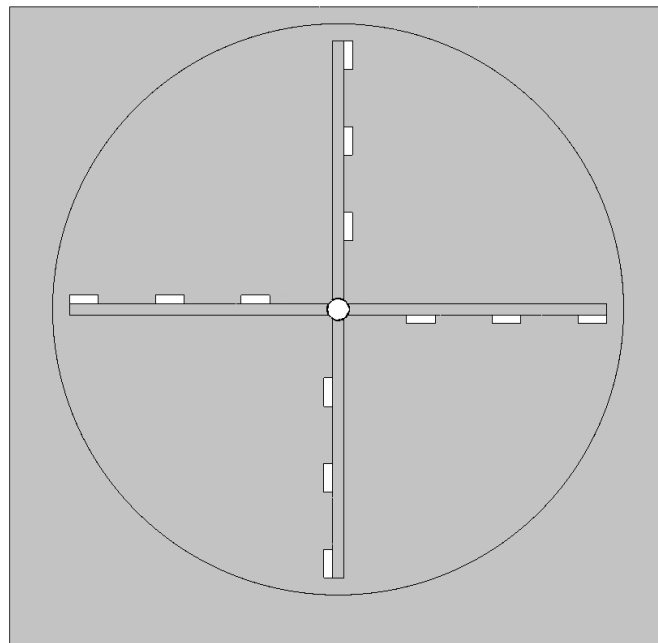**Figure 21: 3D View Fluent Schematic Showing Plane of Interest**

Figure 22: Front View Fluent Schematic Showing Plane of Interest

4.2.5 Time Step Size and Mesh Refinement

Determination of the time step size was related to the rotational speed. For a rotational speed of 3 rpm (or its equivalent in rad/s), one full rotation of the flocculator paddle wheel would consume 20 seconds. An initial assumption of the time step size was considered as the time needed for the mixer to rotate 1°. Initial numerical simulations were conducted using a time step size of $0.0\overline{5}$ seconds (equivalent to 1° rotation) with a maximum of 20 iterations per time step. Results showed that the solution was converging while consuming the complete 20 iterations per time step. Consequently, the time step size was decreased to the time needed for the mixer to rotate 0.5°. This showed to be adequate since the solution readily converges as mentioned earlier. Therefore, all numerical simulations for both turbulence models were conducted using the modified time step size of $0.02\overline{7}$ for 3 rpm, and $0.0208\overline{3}$ for 4 rpm. The cell courant number was always less than 1.0 using the refined time step sizes stated.

In an attempt to study the dependency of model on the mesh, results were generated first using the original mesh having 2,144,409 elements followed by the refined mesh having 2,877,263 elements. Mesh refinement was achieved by decreasing the element size of the mixer body from 9 x 10^{-3} m to 7 x 10^{-3} m. Average values of velocity magnitude at different locations surrounding the blades were compared for the original and refined mesh of both turbulence models. The percent difference between the results was 1.73 % for the SST k–ω model and 3.51 % for the IDDES model. IDDES showed a higher percent difference since it is a hybrid RANS-LES model. These differences were considered to be negligible, and therefore the original mesh having 2,144,409 elements with a time step size of 0.5° rotation was used to perform the simulations.

Chapter Five

Results and Analysis

5.1 PIV Experimental Results

PIV is widely used by many researchers because of the convenience it delivers in producing quantitative numerical data for recorded images. Single instantaneous velocity fields only show the characteristics of raw measurements without delivering a complete understanding of the fundamental flow physics. However, it is possible to investigate the turbulent variation element of a flow using large time resolved velocity data sets.

The mean or time averaged PIV velocity fields and streamlines were used to visualize the prevailing flow structures at a plane perpendicular to the blades of the paddle flocculator at mid-length of the blades. PIV images recorded during the experimental procedure were processed and averaged as explained earlier, and the following velocity vector fields and velocity streamlines were produced for each of the three blades. Experiments were conducted for a rotational speed of 3 rpm and 4 rpm respectively, and hence six data sets were acquired as shown below.

Furthermore, velocity data were exported for each of the velocity vector fields presented. Velocity components in the x and y direction were used to calculate the average velocity magnitude in m/s.

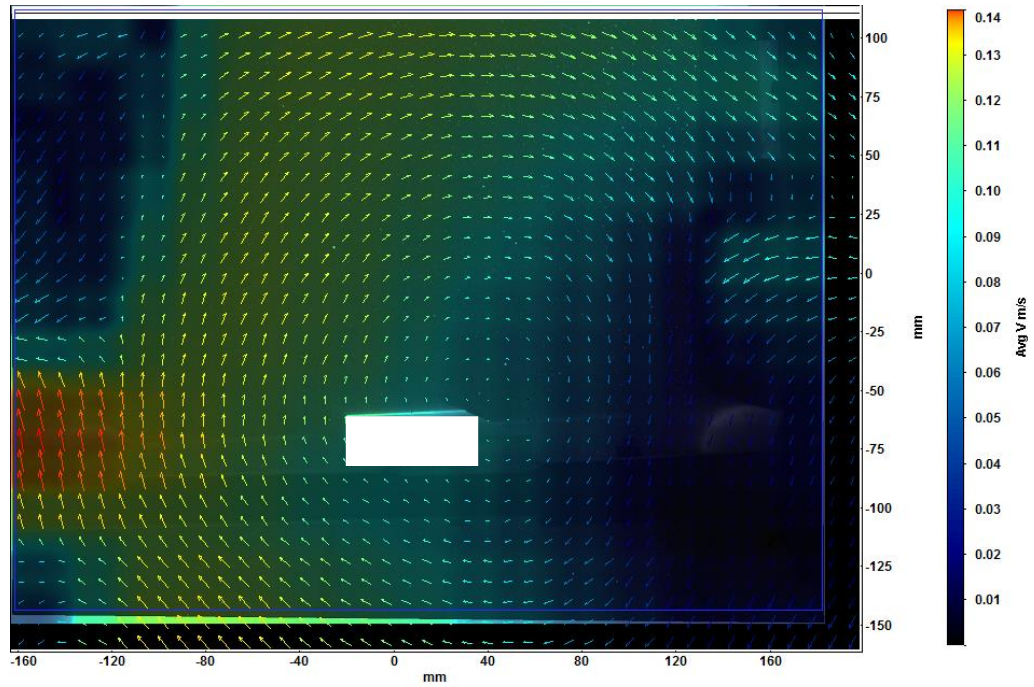**PIV Set 1: Blade 1 velocity vector field and streamlines at 3 rpm**

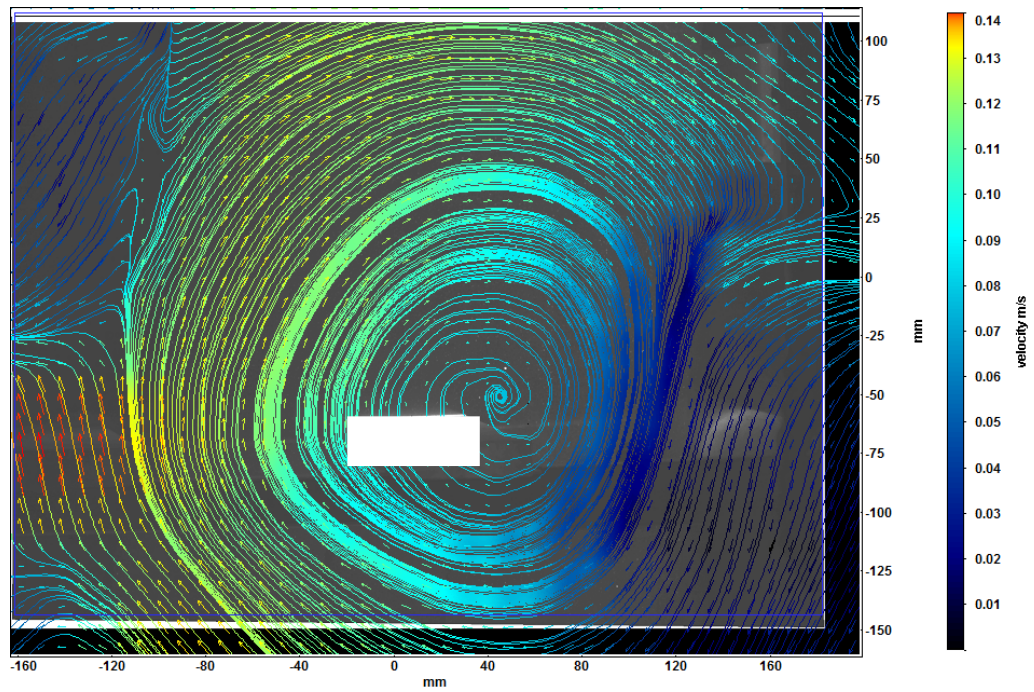**Figure 23: PIV Velocity Field of Blade 1 at 3 rpm**

Figure 24: PIV Streamlines of Blade 1 at 3 rpm

PIV Set 2: Blade 1 velocity vector field and streamlines at 4 rpm

Figure 25: PIV Velocity Field of Blade 1 at 4 rpm

Figure 26: PIV Streamlines of Blade 1 at 4 rpm

PIV Set 3: Blade 2 velocity vector field and streamlines at 3 rpm

Figure 27: PIV Velocity Field of Blade 2 at 3 rpm

Figure 28: PIV Streamlines of Blade 2 at 3 rpm

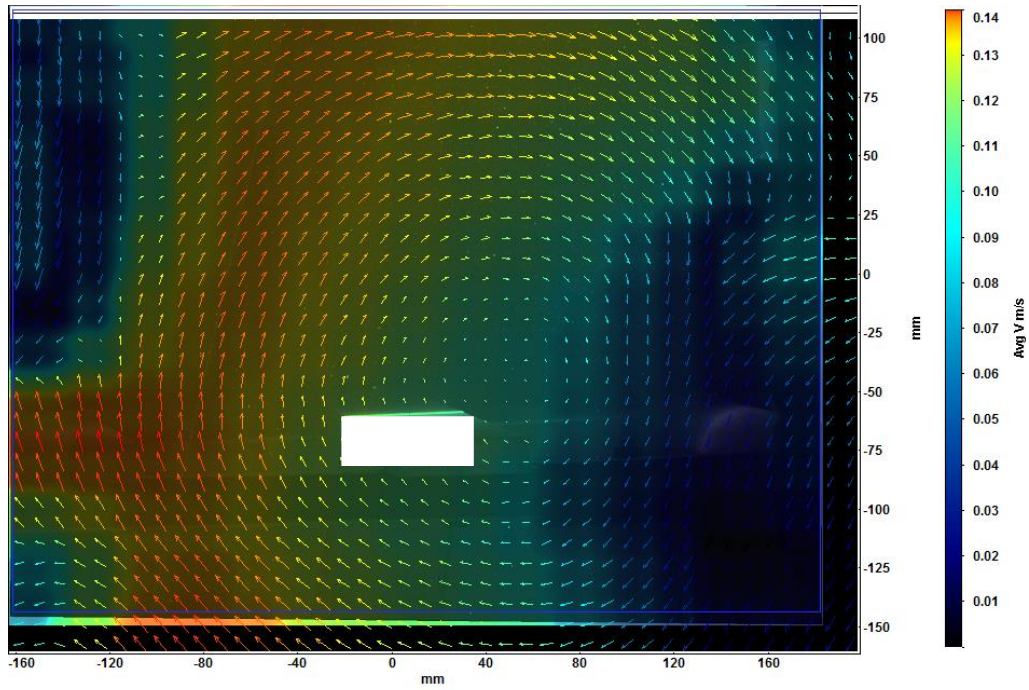**PIV Set 4: Blade 2 velocity vector field and streamlines at 4 rpm**

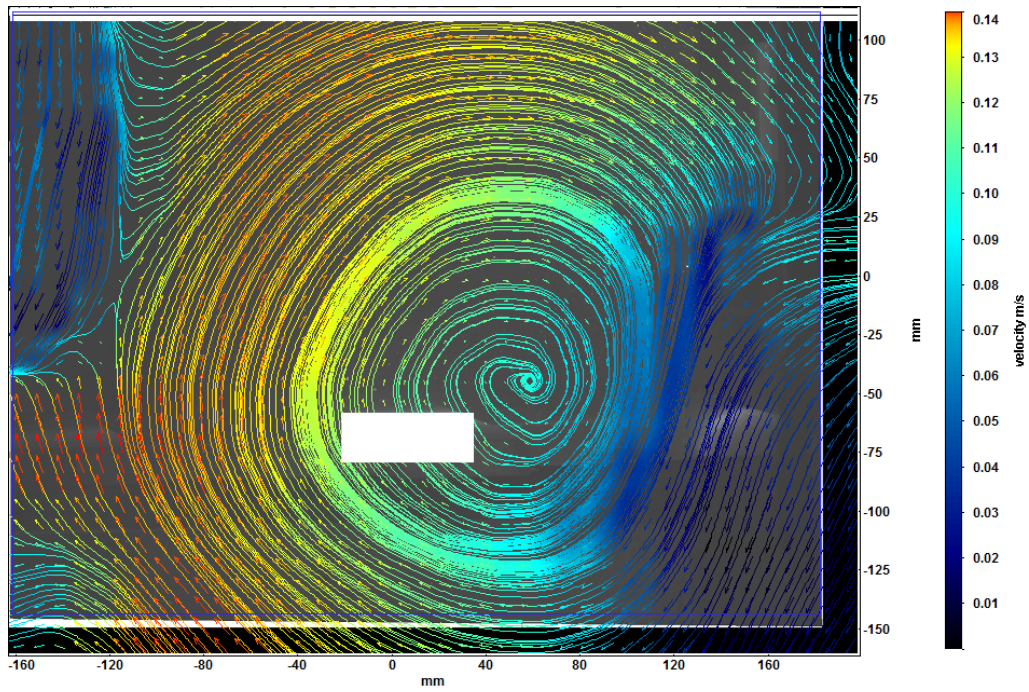Figure 29: PIV Velocity Field of Blade 2 at 4 rpm

Figure 30: PIV Streamlines of Blade 2 at 4 rpm

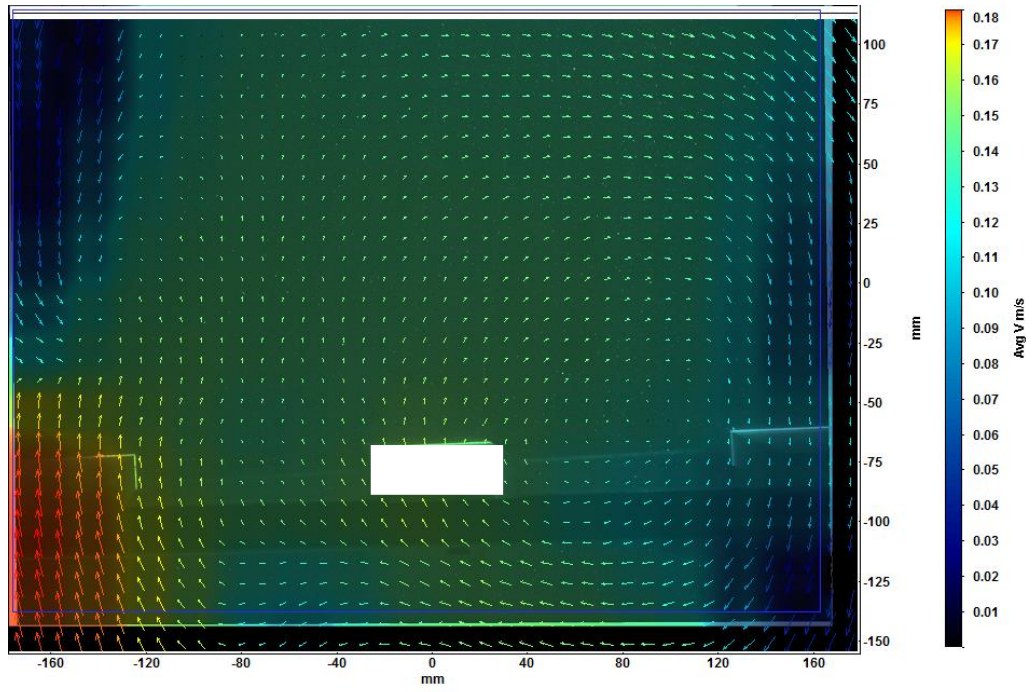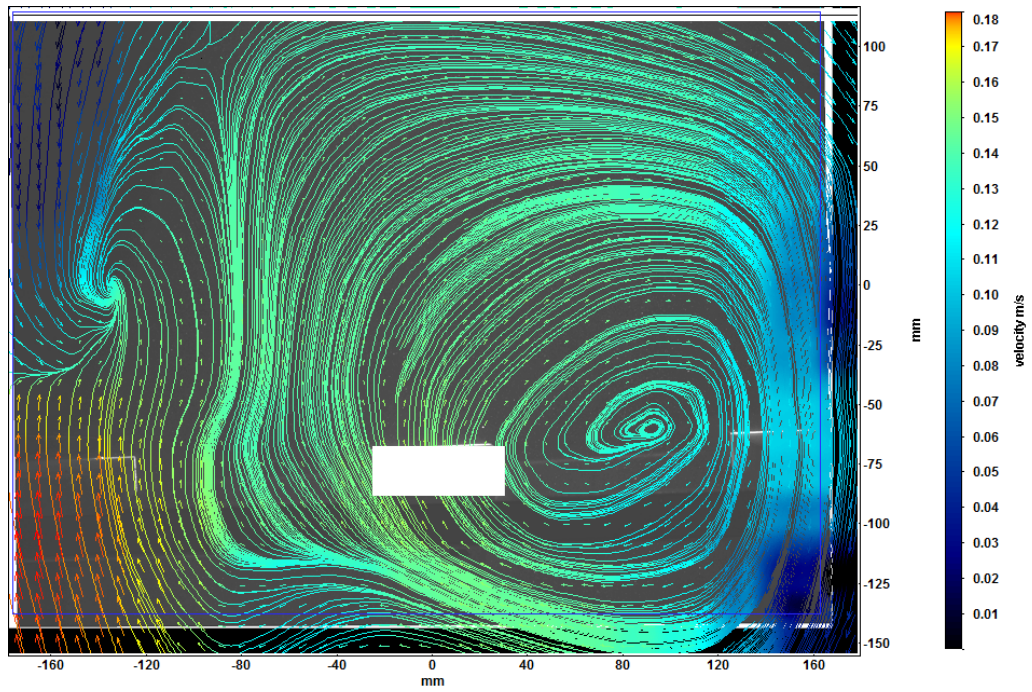# PIV Set 5: Blade 3 velocity vector field and streamlines at 3 rpm

Figure 31: PIV Velocity Field of Blade 3 at 3 rpm
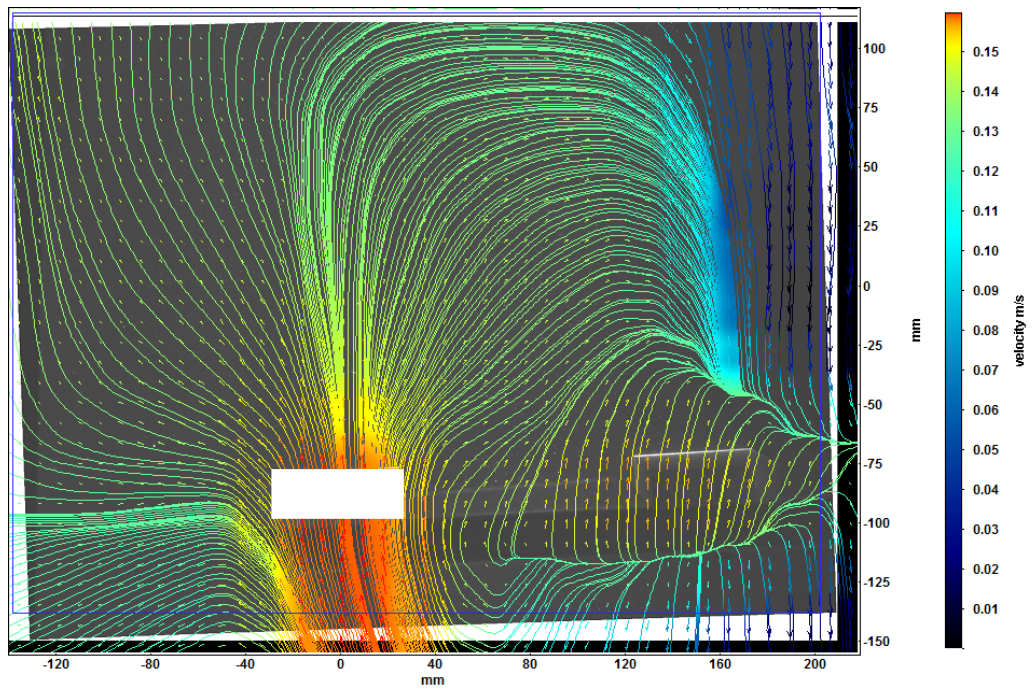
Figure 32: PIV Streamlines of Blade 3 at 3 rpm

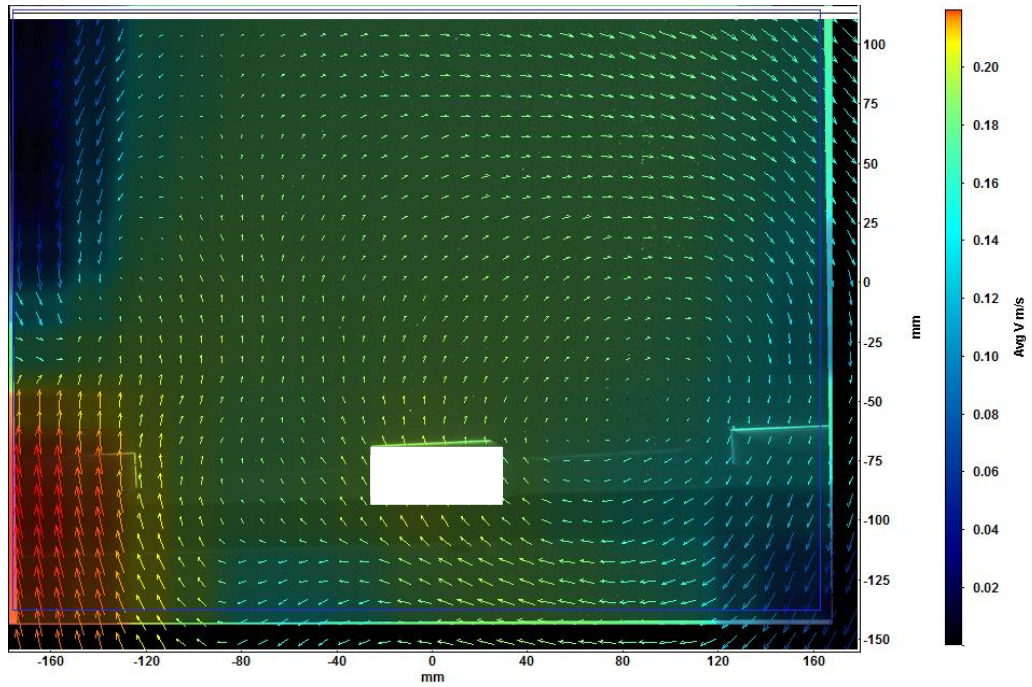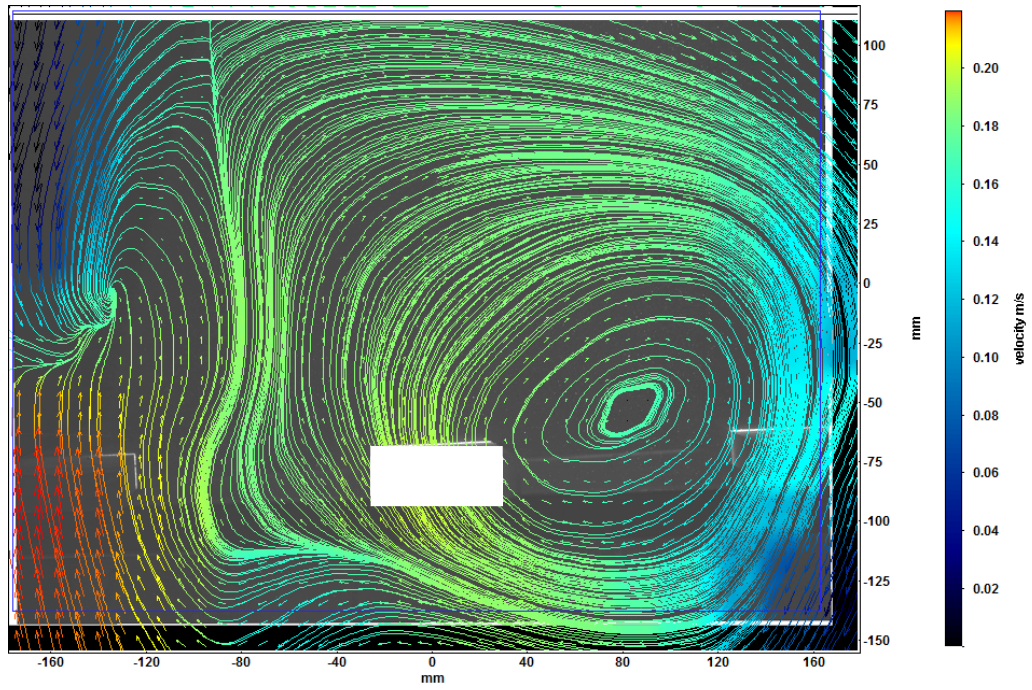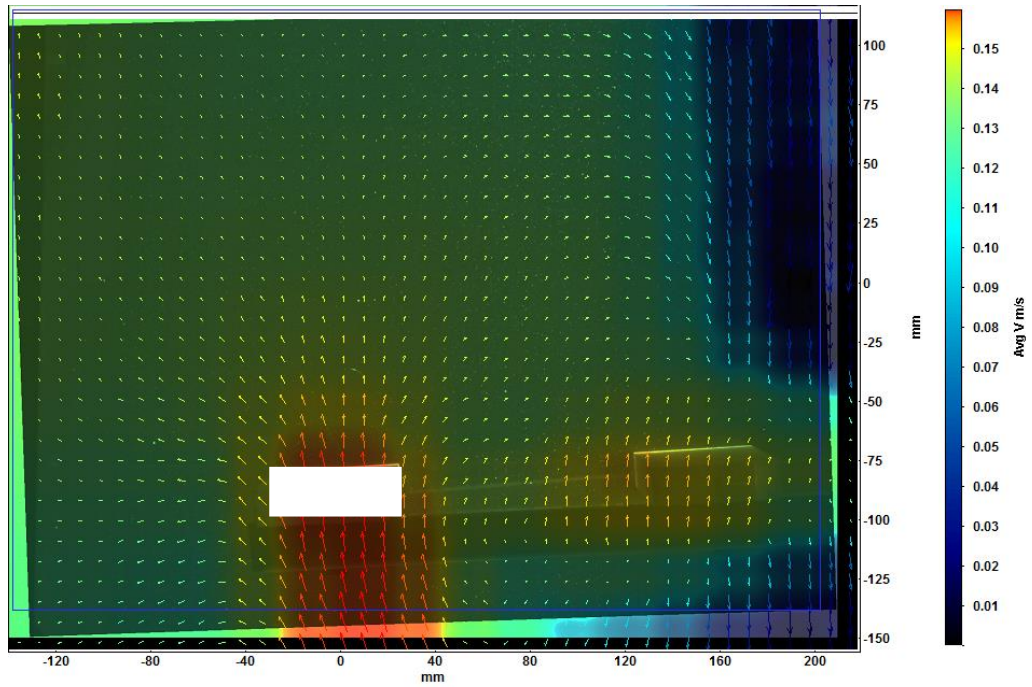**PIV Set 6: Blade 3 velocity vector field and streamlines at 4 rpm**
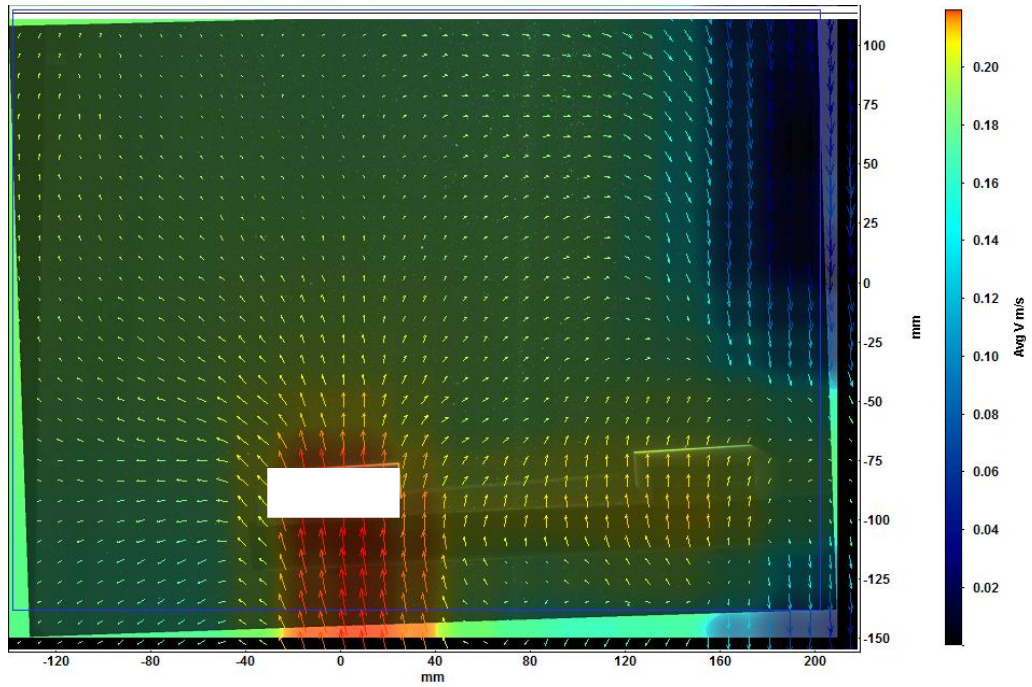
Figure 33: PIV Velocity Field of Blade 3 at 4 rpm
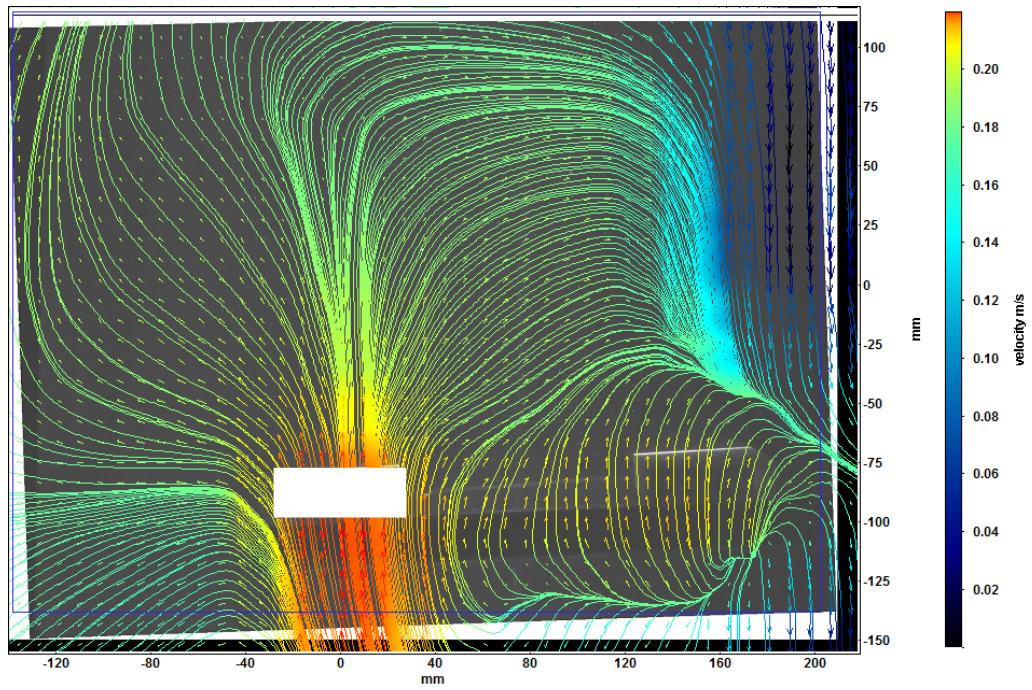
Figure 34: PIV Streamlines of Blade 3 at 4 rpm

5.2 CFD Numerical Results

CFD was used to simulate the flow inside the laboratory scale paddle flocculator. The investigation focused on the velocity field at a plane perpendicular to the paddle wheel located at mid-length of the blades. Simulations were conducted using two turbulence models namely the SST k–ω and the IDDES for rotational speeds of 3 rpm and 4 rpm. After converging the solution, it was ensured that steady state would be reached prior to generating the averaged velocity contours. Achieving steady state was guaranteed by the comparison of velocity contours exported at each rotation for the last four consecutive rotations. The absolute similarity of the contours is shown below:

Figure 35: Comparison of CFD Velocity Contours

68

Once steady state is reached, time averaged velocity contours are generated as below.

IDDES at 3 rpm

Figure 36: IDDES Velocity Contour at 3 rpm

SST k–ω at 3 rpm
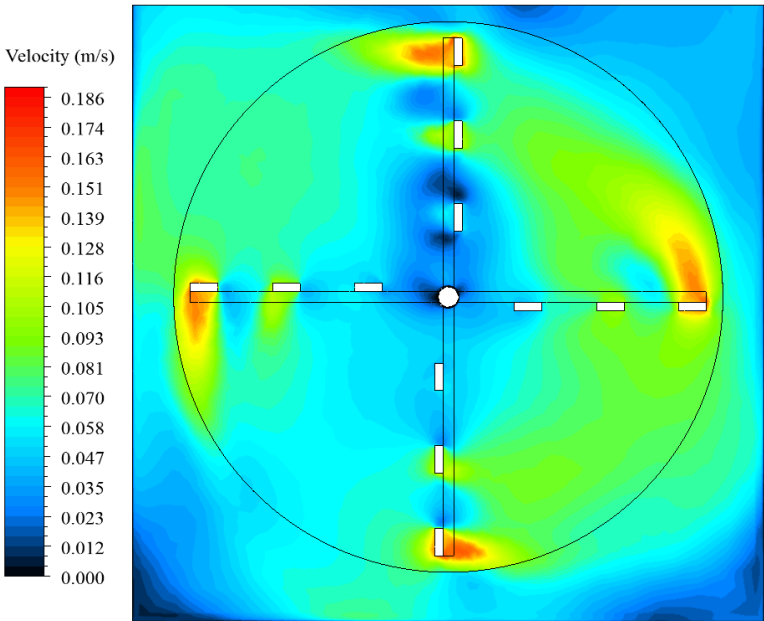
Figure 37: SST k–ω Velocity Contour at 3 rpm

IDDES at 4 rpm
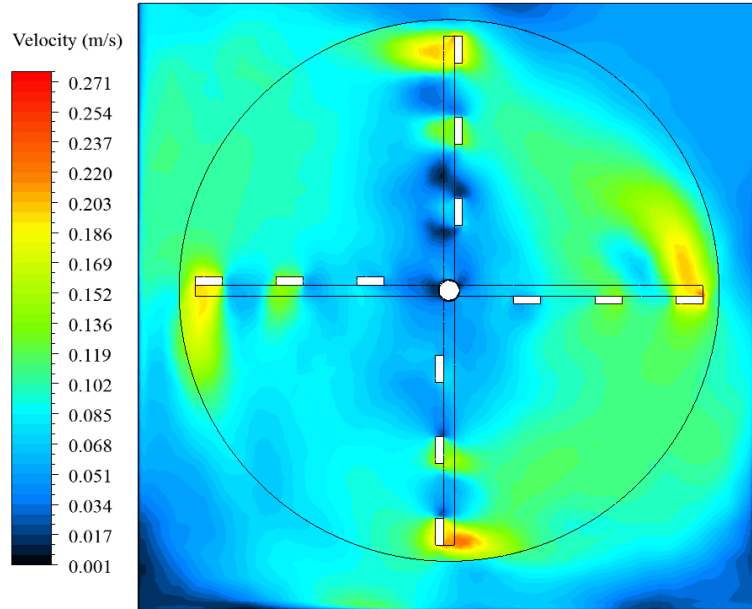
Figure 38: IDDES Velocity Contour at 4 rpm

SST k–ω at 4 rpm
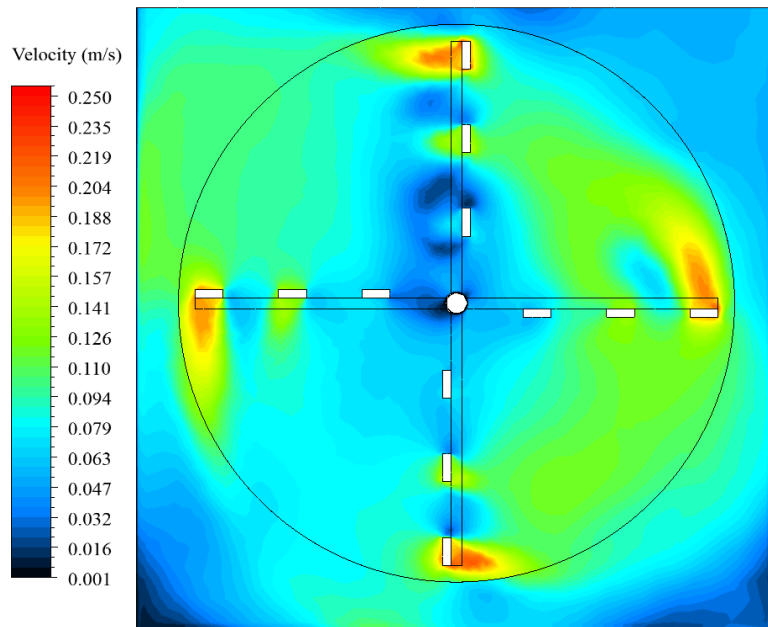
Figure 39: SST k–ω Velocity Contour at 4 rpm

5.3 Analysis and Discussion

5.3.1 Accuracy and Precision of PIV Results

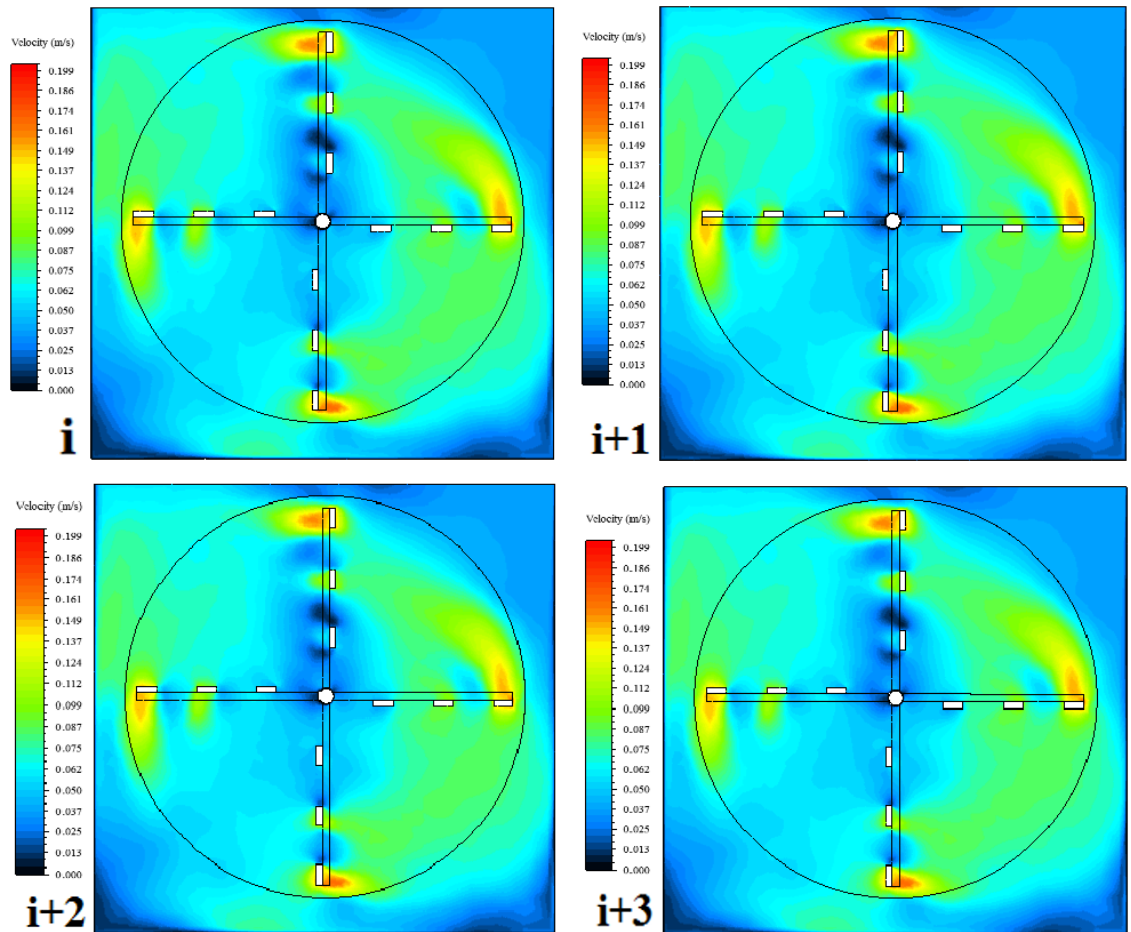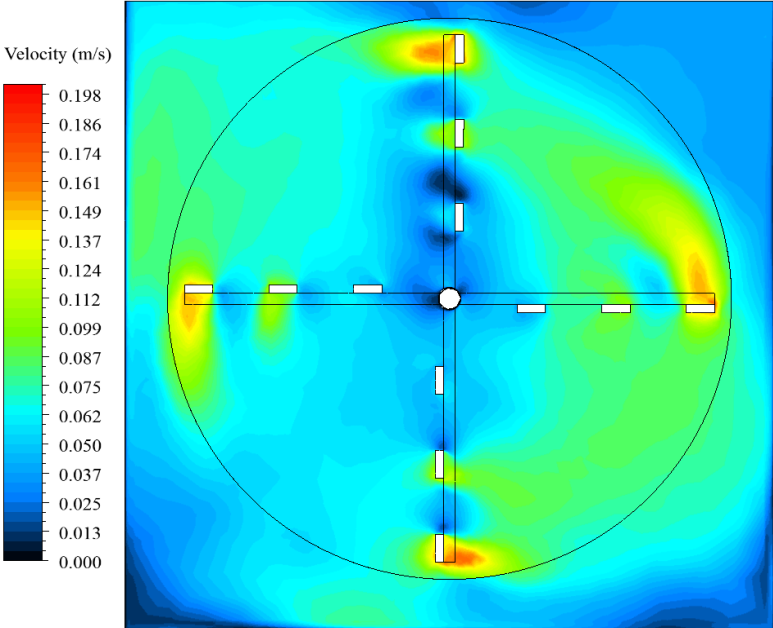The results obtained from PIV experiments are quantitative velocity vector fields, where the velocity magnitude at each vector location can be determined. Also, streamlines are produced to understand the flow structures and the complete field behavior.

Prior to analyzing the PIV results, their accuracy and precision must be addressed. In the case of these experiments, there is only one quantitative term that can be determined analytically and used for comparison with experimental measurements. That is, the velocity at the center of each blade. The velocities at the peripheries of blades are not considered since the behavior of water particles at these locations is complex in a turbulent rotating flow as the case of this study.

Therefore, the velocity of each blade is calculated analytically at its center as follows:

$$v_p = \frac{2\pi rN}{60}$$

Where: r is the distance to centerline of blade from center of rotation (m)

            N is the shaft rotational speed (rpm)

Table 5: Analytical Velocity of Blades

Blade Velocity v_p (m/s)	Blade 1	Blade 2	Blade 3
N = 3 rpm	0.046	0.093	0.140
N = 4 rpm	0.061	0.124	0.186

The blades are denoted according to their location from the shaft as per figure 11.

Since PIV is used to measure instantaneous velocity of particles in a flow, this means the time averaged results must yield velocities closely equal to those calculated at the center of blades. From this approach, the PIV results are primarily compared with the analytical results.

<p align="center">Table 6: Comparison between Analytical and PIV Blade Velocities</p>

Blade Velocity v_p (m/s)		Analytical	PIV
N = 3 rpm	Blade 1	0.046	0.049
	Blade 2	0.093	0.095
	Blade 3	0.140	0.135
N = 4 rpm	Blade 1	0.061	0.065
	Blade 2	0.124	0.130
	Blade 3	0.186	0.185

Table 6 shows that the velocity values obtained by PIV are very close to the analytical ones. Noting that velocity values are recorded to the third significant figure, the highest percentage error recorded is 6.5 % at blade 1 for both rotational speeds. For blades 2 and 3, the percentage error does not exceed 5 %.

These variations are negligible and arise from practical limitations of the experimental setup such as the rotational speed at which the flocculator was operating during

experiments. Since the rotational speed, as 3 rpm or 4 rpm, cannot be recorded into the control unit of the flocculator, trials were conducted to determine the duration of rotations by using a stop watch. A minimum of three trials were conducted for each rotational speed to determine the input values which would represent 3 rpm and 4 rpm. The average of three trials was used, however the control unit is accurate to one decimal digit only.

The first blade records the highest percentage error because of its location. Since it is the blade closest to the rotor, flow structures are complex at this location, compared to the entire flow in the basin. Not only so, but the first blade from the preceding paddle wheel arm also impacts the flow structures at this blade. The movement of water particles represented by seeding particles is complex. This is further discussed in the following sections. In addition, from a quantitative approach, the velocity values at this blade are very low, which yield higher percentage errors for very small variations. The differences are negligible and stem from practical reasons explained above.

Moreover, the repeatability and reproducibility of experimental results was studied. Repeatability was ensured by conducting each of the six experiments a second time and comparing results. The velocity values at the center of blades were compared for the two sets of experiments. Noting that both results are experimental, the average percentage difference between the two experimental sets was 3.1 %, which is insignificant. The reproducibility of the experimental results was also achieved through this comparison because the PIV system was re-calibrated independently for each experiment. This means that the experimental setup or system can be reproduced by other researchers. The validity of the experimental results allows us to accept these results as factual and correct measurements. The following section covers the analysis and discussion of these results.

5.3.2 Analysis of PIV Results

Velocity streamlines at blade 1 show a direct rotational flow surrounding and encompassing the blade. These flow structures stem form a point located to the right of the blade, which is between the rotor and the blade. A meticulous revision of the velocity vector field, with attention to the direction of individual vectors, shows a recirculating flow which starts next to the rotor, proceeds below the blade and revolves around the blade upwards.
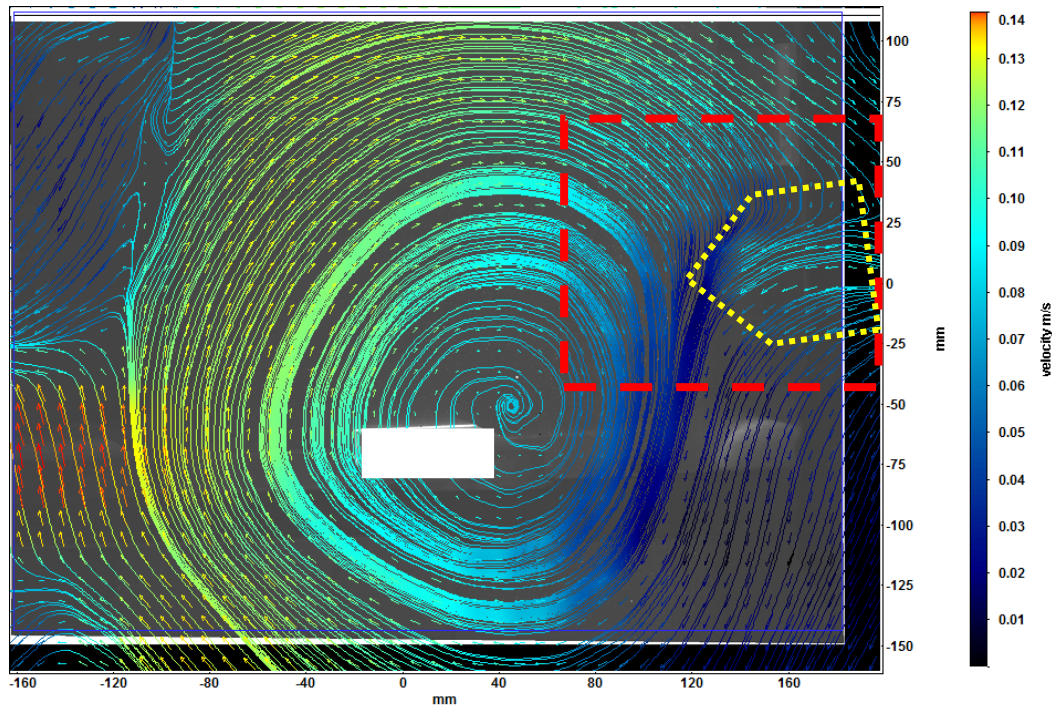
Figure 40: PIV Streamlines of Blade 1 at 3rpm Detailed

The velocity vectors at the face of the blade are in the upward direction which is predictable, since the paddle wheel arm was rotating clockwise and the PIV images were recorded as the arm moved the water upwards.

Inspecting the area denoted by the dashed box in red, it is interesting to identify another aspect of the re-circulating flow over and around the blade. Flow visualization indicates

74

a small water flux joining into the re-circulation zone. This flux is approaching from the right side of the blade and at a height of about 6 cm from the blade face. This flux would be due to the impact of the first blade of the arm preceding the one seen in the image. It can be clearly identified that this flux is intersecting the path of the re-circulating flow and joining its peripheral layer. Flow visualization at a rotational speed of 4 rpm shows the same behavior and structures, evidently with higher velocity values. The velocity vector field clearly shows the impact of these flow structures on the second blade, which is to the left of blade 1. The periphery of blade 2 is encompassed within the re-circulating flow and high velocity magnitudes are identified as seen in figure 40.

Moving on to the second blade, the velocity fields and streamlines are obtained by re-calibrating the PIV system at this location (i.e. face of blade 2). This means flow structures are investigated at this location, and more importantly, the impact of these structures on adjacent blades are determined. Another form of spiral flow is identified between blades 1 and 2. The vector field visibly indicates flow of water from beneath blade 2 moving upwards as noted by the vector directions. Clearly, as seen in the dashed box below, these vectors are not proceeding vertically upwards from the face of the blade, however they are rotating towards the right and gradually downwards. Velocity streamlines noticeably show an immense flow rotating around blade 2 and joining a spiraling flow down onto the face of blade 1. Vectors from the velocity field of blade 2 show downward directed vectors on the face of blade 1 approaching from the re-circulating flow that forms between these two blades and encompasses both.
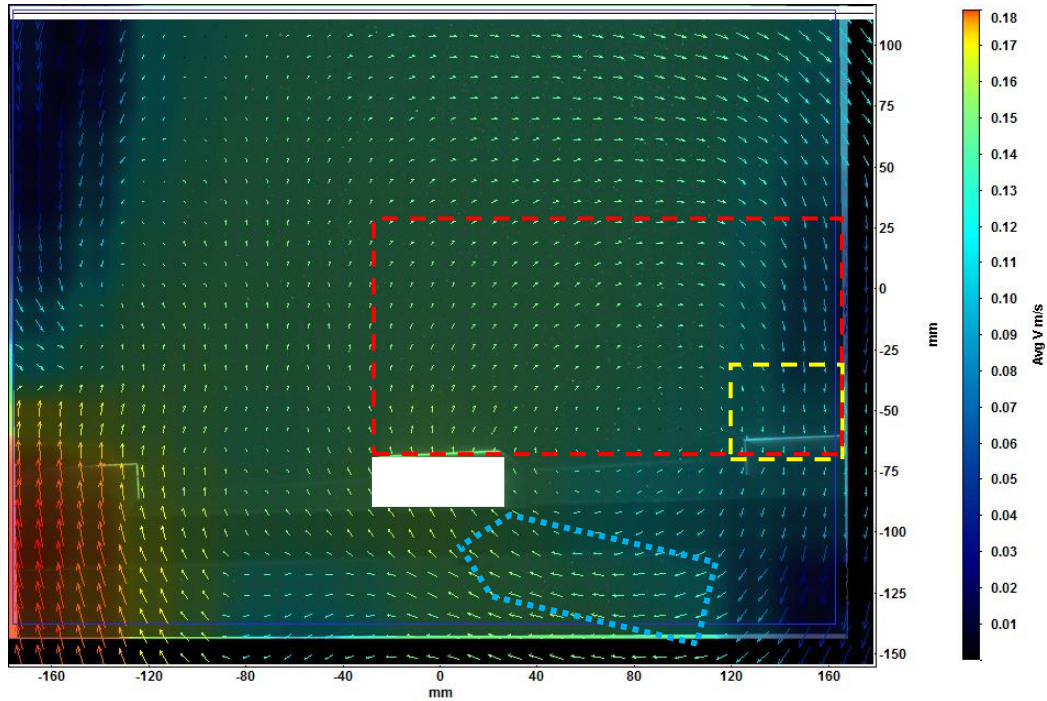
Figure 41: PIV Velocity Field of Blade 2 at 3 rpm Detailed

Flow structures at 4 rpm show similar behavior with higher velocity. It is important to note that there are no major interacting flow structures between blades 2 and 3. This can be studied and investigated by inspecting the velocity field obtained at blade 3.

As mentioned earlier, the accurate investigation of the flow field is achieved through a separate system calibration at each blade. The velocity field of blade 3 does not show a major contribution of velocity vectors from previous blades that are joining the flow beneath blade 3. The main flow flux beneath blade 3 is coming from vertical velocity vectors directed upwards with the flow of water. Minor rotational flow is noticed between blades 2 and 3 that contribute to blade 3. The velocity vectors and streamlines above the face of blade 3 can be divided into three sets. The first set is the one at the right periphery of the blade. Flow structures at this location are directly rotating upwards to the right i.e. towards blade 2. The second set is considered at the middle of the blade. Velocity vectors

76

at this location proceed vertically upwards without any deviation, and do not show any rotation. A decrease in velocity magnitude is identified with increasing height above the blade face. While for the third set, which is at the left periphery of the blade, flow is directed immediately to the left, i.e. towards flocculator walls. The majority of the flow, represented by the velocity vectors, proceeds upwards, while part of the flow advances horizontally downwards.
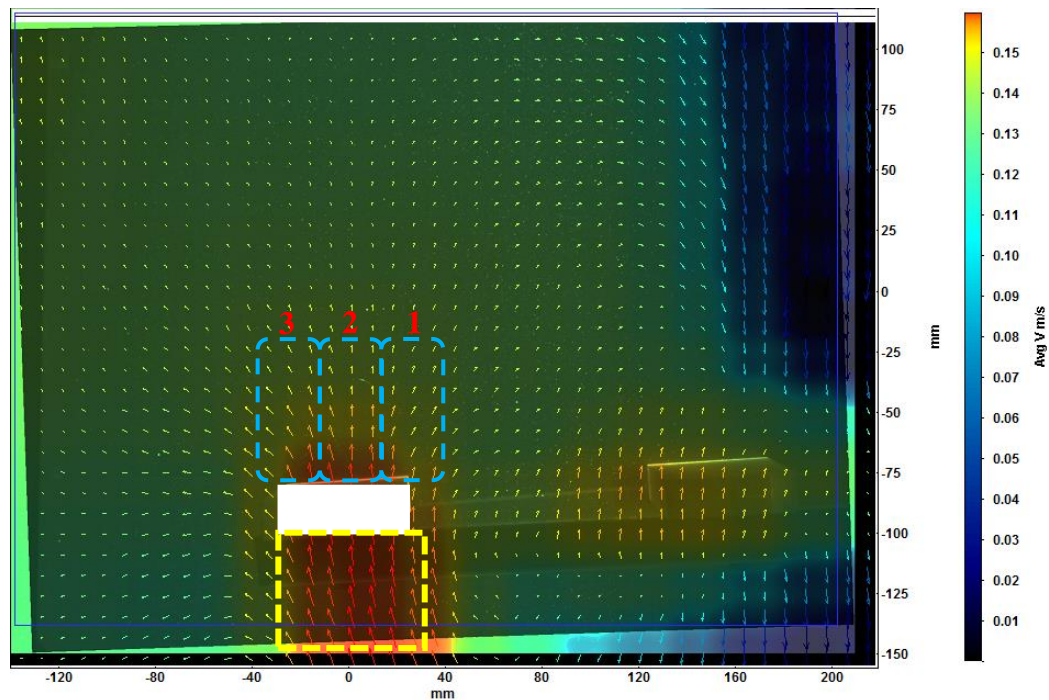
Figure 42: PIV Velocity Field of Blade 3 at 3 rpm Detailed

A close inspection of the velocity streamlines at blade 3 shows a major contribution of flow from the left of blade 3, i.e. set 1, joining the rotational flow at blade 2. There is a clear separation of flow between what is referred to as set 1 and set 2. However, both flows re-join at a height of about 15 cm above the blade face and move to the right forming a great flux directed downwards on blade 2.

A qualitative understanding of the velocity vector fields and streamlines is required to have a proper understanding of flow behavior and structure. However, a quantitative approach is required to plot velocity profiles above blades and to comprehend the variation of velocity magnitude with increasing height above blade faces. Here, it is important to note that velocity magnitude data are exported from each experiment conducted at each blade. Velocity profiles were plotted at the face of each of the blades, and at successive distances of 2.5 cm vertically upwards up to a height of 10 cm as shown in figure 43, for both rotational speeds. Noting that the width of each blade is 5 cm, 7 velocity points were identified across the width ensuring the production of representative velocity profiles.
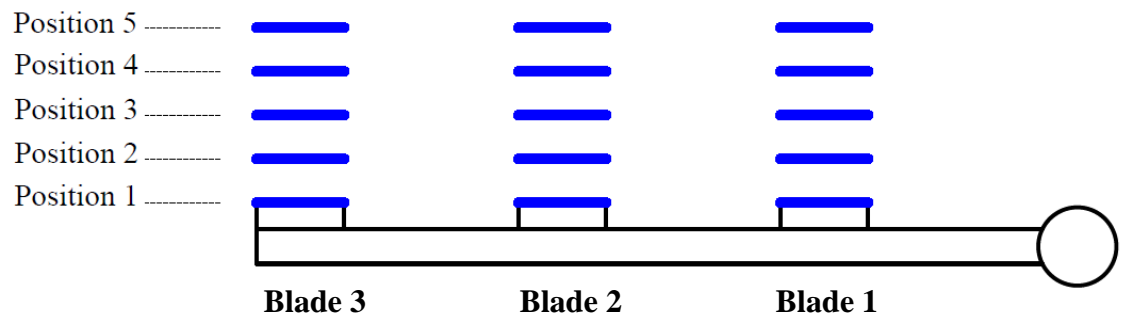

Figure 43: Schematic Showing Positions of Velocity Profiles Plotted

In the graphs of table 7, the x axis represents the width of each blade in mm. The origin (0 mm) represents the left periphery of blades, while the end (50 mm) represents the right periphery of blades as per Figure 43.

Table 7: PIV Velocity Profiles at 3 rpm and 4 rpm

PIV at 3 rpm	PIV at 4 rpm

Position 1

Velocity Profiles at 3 RPM / Y = 0.0 cm
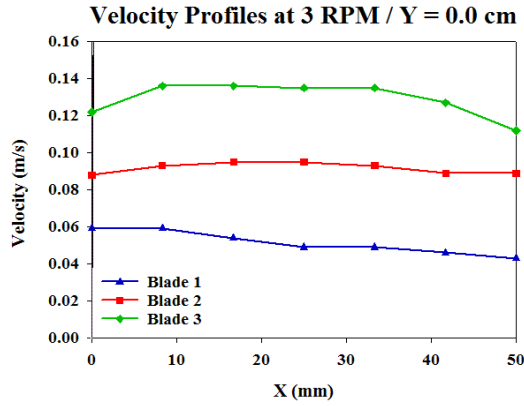
Figure 44: Position 1 PIV Plot at 3 rpm

Velocity Profiles at 4 RPM / Y = 0.0 cm
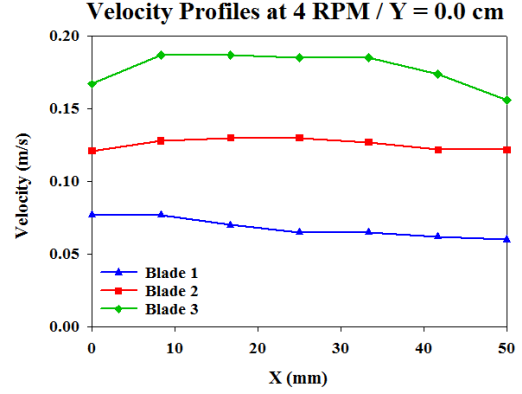
Figure 45: Position 1 PIV Plot at 4 rpm

Position 2

Velocity Profiles at 3 RPM / Y = 2.5 cm
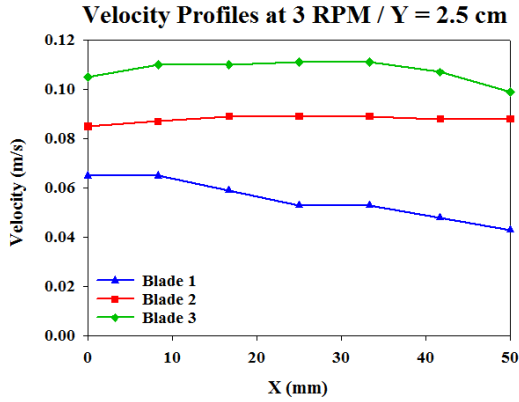
Figure 46: Position 2 PIV Plot at 3 rpm

Velocity Profiles at 4 RPM / Y = 2.5 cm
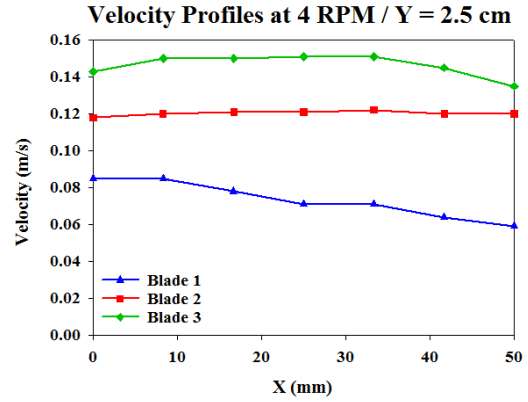
Figure 47: Position 2 PIV Plot at 4 rpm

Position 3

Velocity Profiles at 3 RPM / Y = 5.0 cm
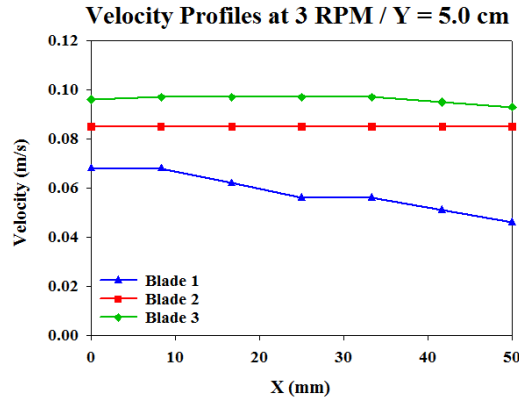
Figure 48: Position 3 PIV Plot at 3 rpm

Velocity Profiles at 4 RPM / Y = 5.0 cm
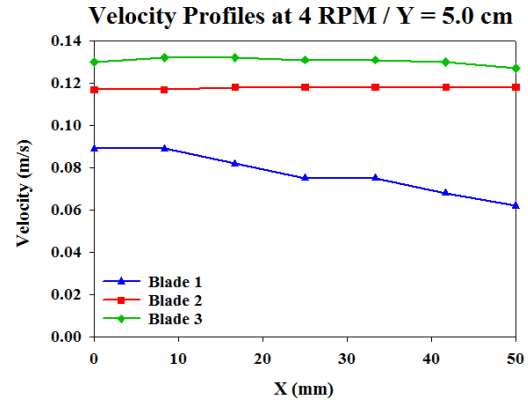
Figure 49: Position 3 PIV Plot at 4 rpm

79

Position 4

Velocity Profiles at 3 RPM / Y = 7.5 cm
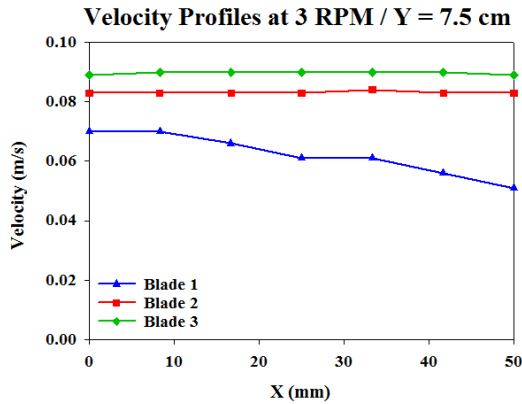
Figure 50: Position 4 PIV Plot at 3 rpm

Velocity Profiles at 4 RPM / Y = 7.5 cm
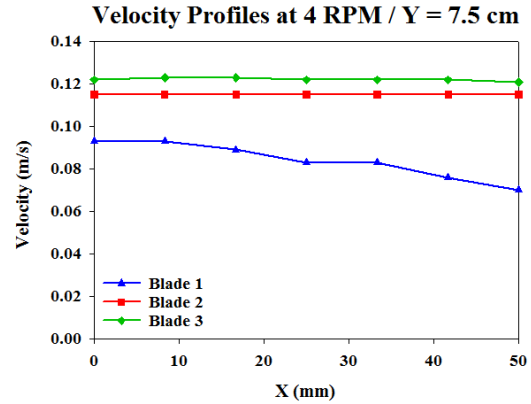
Figure 51: Position 4 PIV Plot at 4 rpm

Position 5

Velocity Profiles at 3 RPM / Y = 10.0 cm
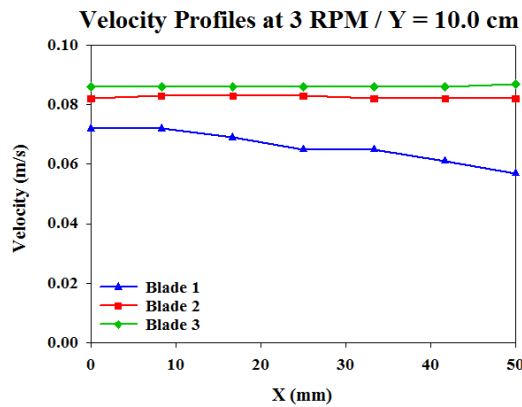
Figure 52: Position 5 PIV Plot at 3 rpm

Velocity Profiles at 4 RPM / Y = 10.0 cm
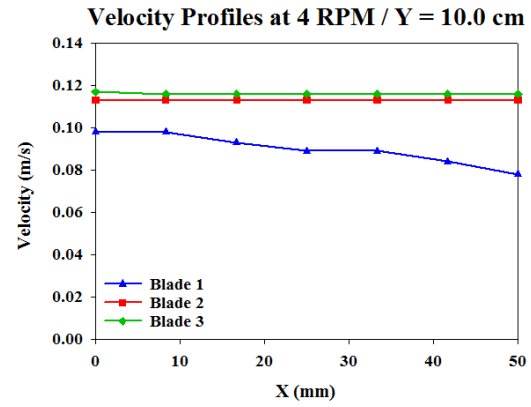
Figure 53: Position 5 PIV Plot at 4 rpm

Velocity profiles were plotted for each blade, for both rotational speeds, up to a height of 10 cm because the graphs show that at this height flow becomes uniform above blades 2 and 3 since both profiles show horizontal lines at almost equal magnitudes as seen in figures 52 and 53. However, this does not apply for blade 1. From the graphs above, it can be clearly identified that the velocity profiles of blades 2 and 3 show a trend of similarity with increasing height, while that of blade 1 varies independently.

80

At the face of blades, figures 44 and 45, the velocity profile for blade 1 shows incremental increase from the right periphery until the middle of the blade. Minor uniformity is identified at mid-blade which becomes more evident with increasing height above blade face. Further increase in velocity is noticed from mid-blade until the left periphery. What is remarkable about velocity profiles at blade 1, is the fact that these profiles maintain the same shape at all positions and do not show any regularity of flow similar to the remaining blades. The odd profile is identified for both rotational speeds.

Regarding blade 2, velocity profiles show some kind of a peak at mid-blade as compared to blade peripheries as seen in figures 44 and 45. However, the profiles becomes uniform and straight with increasing height above blade face. The same form can be identified for blade 3. Velocity profiles at blade 3 show a steep increase from the right periphery, followed by a uniform velocity magnitude spanning over the middle third of the blade. Further decrease is identified towards the left periphery of the blade. The shape of this profile starts to flatten with increasing height above blade face until stretching into a straight line at a height of 7.5 cm represented in figures 50 and 51. Velocity profiles of blades 2 and 3 become completely straight and at equal magnitude at a height of 10 cm from blade faces. This means that the flow becomes uniform at this location. It is important to note that blade 1 maintains the same velocity profile shape at all heights and does not normalize with height because of the swirling flow formed at the center of the mixer encompassing the first blade of all arms.

5.3.3   Analysis and Validation of CFD Results

Time averaged velocity contours are exported from ANSYS CFD Post after steady state is reached. These contours are obtained at a plane perpendicular to the mixer blades and at mid-length. The velocity contours provide a qualitative understanding of the velocity flow field at all locations surrounding the mixer arms and blades.

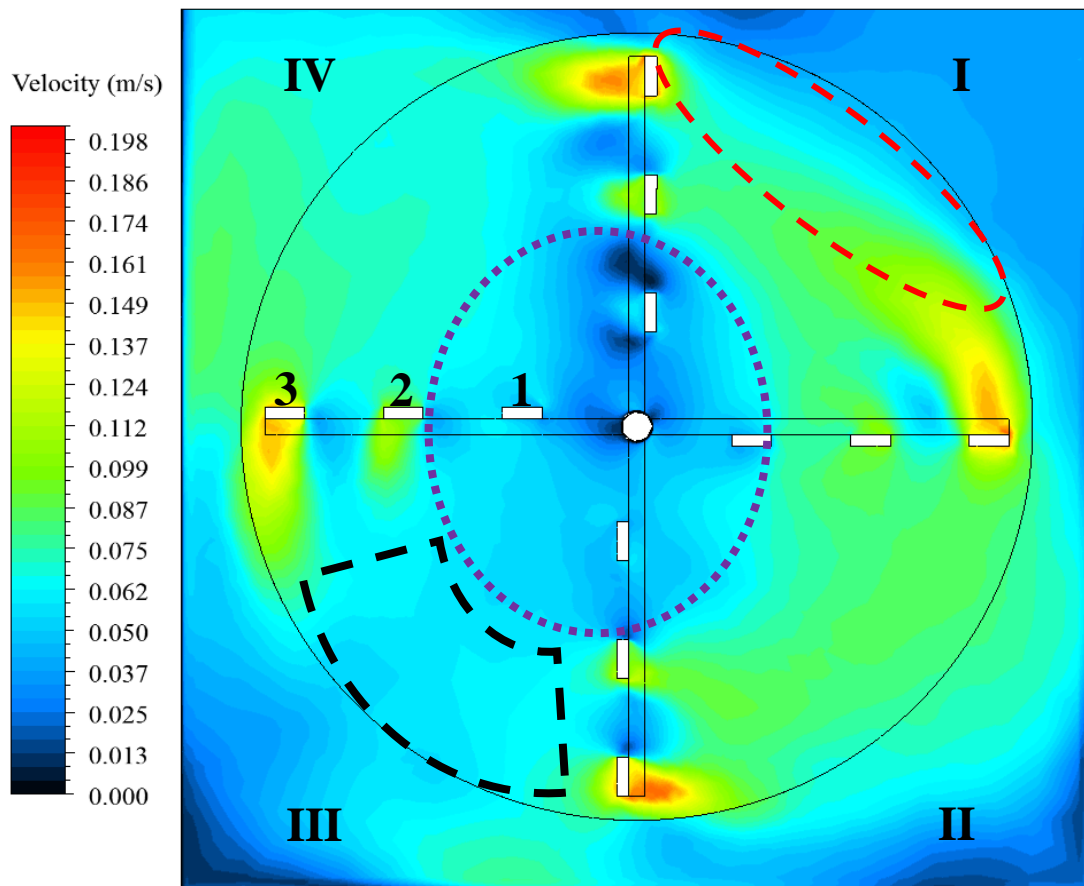**Figure 54: IDDES Velocity Contour at 3 rpm Detailed**

In the velocity contour above, for a rotational speed of 3 rpm, the mixer is rotating clockwise, and the velocity of blades ranges between 0.046 m/s and 0.140 m/s. The flow is discussed according to the annotations above. Each Roman numeral represents one quadrant, and the blades are numbered with respect to their location from the center. To

start with, the velocity at the corners (of quadrants II and III) is very low and almost equal to zero. This is expected since these locations are not within the rotational diameter of the mixer, and therefore water particles do not partake much to any of the mixing speed.

In quadrant I, the velocity field is affected by the top opening of the flocculator. A clear separation of flow is identified within the location marked by the red dashes. At this location, water rotating downwards from the face of blade 3 undergoes a separation within the rotational diameter of the mixer. The flow of water from blade 3 is interfered with flow layers of low velocity. The velocity field at the top right corner shows low velocity magnitude ranging between 0.025 m/s to 0.050 m/s. This can be anticipated since very little to no mixing is felt by the water. However, since the water body is not bounded by a top wall, water particles blend at low velocities as noted. Flow rotating downwards from each of blades 2 and 3 join and another flow separation area is identified that is formed due to blade 1. This is discussed at the end since it incorporates all quadrants.

Moving to quadrant II, flow from both blades 2 and 3 proceeds rotating downwards. Water surrounding blade 3 feels the entire mixing speed with no separation. Water surrounding blade 1 does not show a major contribution regarding the rotational movement of the water mass. Velocity magnitude decreases towards the bottom right corner as expected until reaching almost zero at certain locations at the bottom of the flocculator. Noting that water is bounded by the right and bottom walls of the flocculator, water particles interact with these walls as the mixer rotates. This interaction incorporates flow, which drifts from the rotating regime, hitting the walls and spinning. Relatively higher velocity magnitudes are identified near the right wall as compared to quadrant I.

Regarding quadrant III, the velocity flow field shows that water within this quadrant rotates at noticeably low or lower velocity magnitudes as compared to the previous quadrants. This can also be expected and predicted by considering the rotational orientation of the mixer. In quadrants I and II, water is being moved i.e. rotated or pushed downwards by the impact of the mixer. In quadrant III, water is being pushed upwards by the arm of the mixer. Clearly there is resistance from the water mass at this location onto the approaching flocculator arm. A meticulous inspection of the contour layers shows how the velocity magnitude decreases gradually at the faces of blades 2 and 3. The decrease in velocity magnitude proceeds as seen in the area denoted by the black dashed polygon. There is complete detachment of the rotational flow in this quadrant. This can be explained by considering two factors. The first one is the fact that water is being agitated upwards, which is against the direction of gravity. This creates evident resistance and complex flow structures. The second factor also impacting the field at this location is that the water mass is bounded between the flocculator left wall and the base.

In quadrant IV, the general aspect of a rotational flow still cannot be noticed. Water flows with low velocity above blade 3, and a great interaction with the flocculator wall is identified. A large part of the flow above blade 3 is directed towards the flocculator wall, and this flow gradually loses its magnitude with increasing height up to the top opening. It can be clearly noted that at this location, highest velocity magnitude is identified for the top opening. This is somewhat expected because the water mass is being moved in an upwards direction where part of the flow moves towards the unbounded top.

Regarding flow near blade 1 of all arms, as denoted by the dashed oval in blue, the location at the center includes very complex flow structures. The complex flow structures

are predominant in quadrants III and IV, which is to the left. This denoted area does not show any association with the rotational flow in the flocculator. Some sort of swirling motion can be identified where in quadrants I and II, there is a clear separation between this inner flow and the total rotational flow.

Another aspect of the velocity contour worth noting is the high velocity magnitude immediately beneath blade 3 of all arms reaching up to almost 0.2 m/s. Since blade 3 is the farthest from the center, it has the highest angular velocity. The contour shows that these blades move the water body with great energy carrying water particles at very high velocities. This is more evident for the top and right arm, which are moving water downwards as compared to the bottom and left arm which are moving water upwards.

A comparison between velocity contours at 3 rpm and 4 rpm does not show major variations. At 4 rpm, the impact of complex flow structures swirling at the center of the mixer and incorporating blades 1 of all arms is larger. In quadrant I, the rotating flow at blade 2 is further impacted by the flow structures coming from blade 1 as compared to the 3 rpm field.

As for comparing the results from IDDES and SST k–ω, the main difference in the velocity contours is the velocity magnitude right beneath blade 3. The SST k–ω model clearly shows an extended high velocity flow being carried by blade 3 as compared to IDDES. Another difference can be identified in quadrant III. From IDDES, rotational flow detachment between the flocculator arms is noticed as noted earlier. However, this location is greatly impacted by flow with low velocity magnitude joining from the corner and from the inner flow of the first blades. From SST k–ω, and for the same location, the

contours show relatively higher velocity magnitude as compared to IDDES since there are no joining flows from other regions.

From a quantitative perspective, and for comparing CFD and PIV results, velocity magnitude data were exported from each of the velocity contours at the same locations as that of the PIV velocity fields. That is, at the face of each of the blades, and at successive distances of 2.5 cm vertically upwards up to a height of 10 cm for the velocity profiles.

The lines below represent the locations where velocity magnitude data were exported.
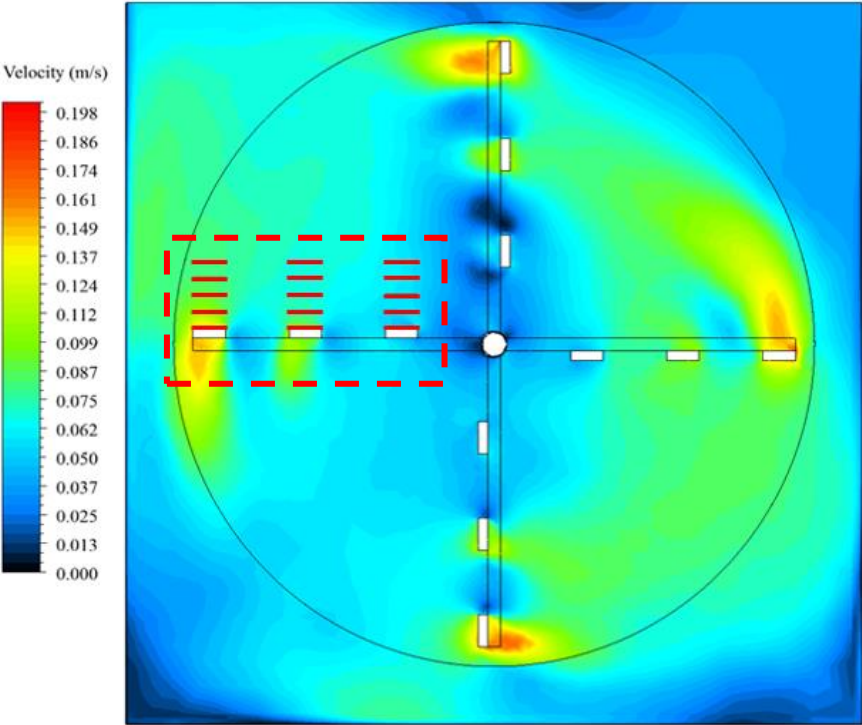
Figure 55: CFD Contour Showing Positions of Velocity Profiles Plotted

Velocity profiles are plotted as described above for both turbulence models adopted. Table 8 shows velocity profile plots at 3 rpm from both models, while table 9 shows the respective plots at 4 rpm.

Table 8: IDDES and SST k–ω Velocity Profiles at 3 rpm

IDDES at 3 rpm	SST k–ω at 3 rpm
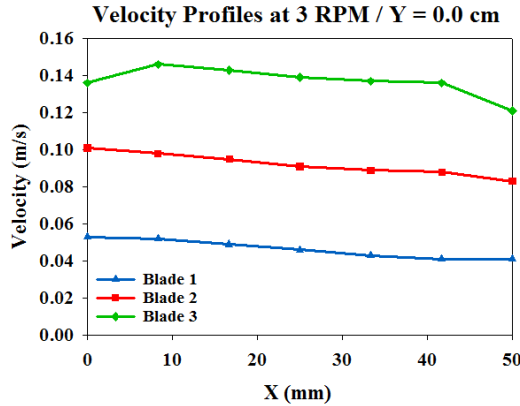
Position 1

Figure 56: Position 1 IDDES Plot at 3 rpm
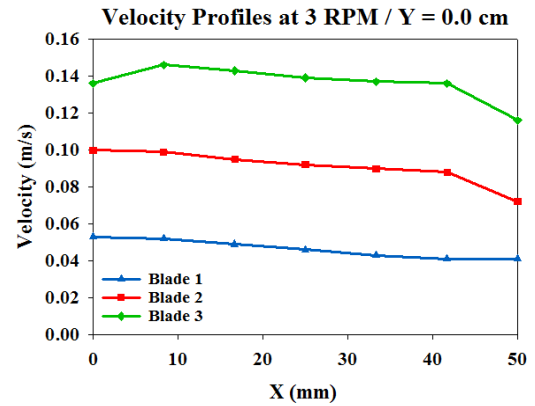
Figure 57: Position 1 SST k–ω Plot at 3rpm

Position 2
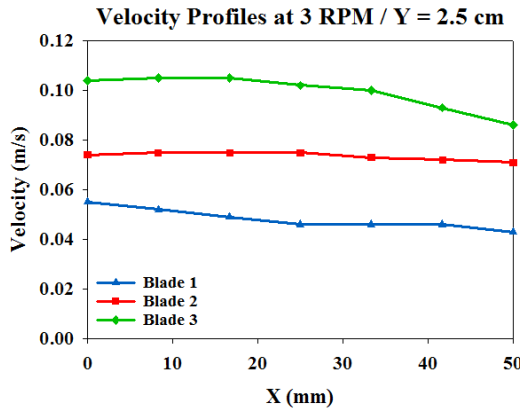
Figure 58: Position 2 IDDES Plot at 3 rpm
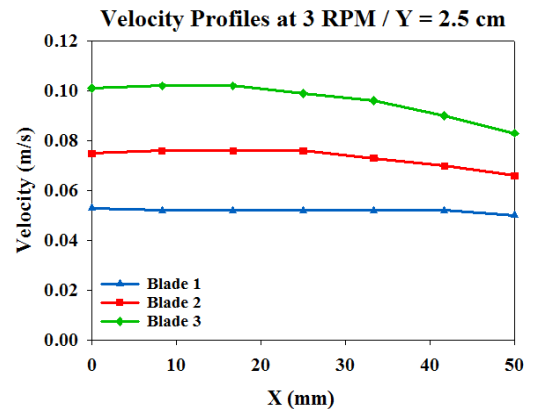
Figure 59: Position 2 SST k–ω Plot at 3 rpm

Position 3
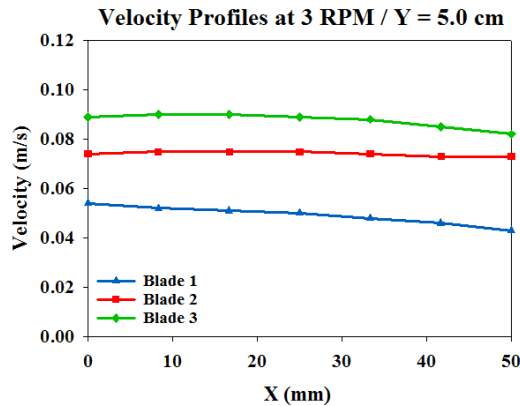
Figure 60: Position 3 IDDES Plot at 3 rpm
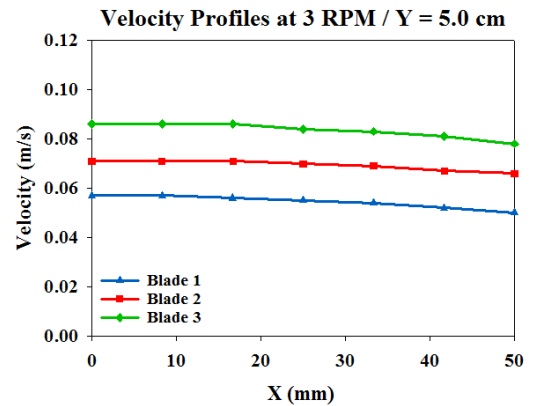
Figure 61: Position 3 SST k–ω Plot at 3rpm

Position 4

Velocity Profiles at 3 RPM / Y = 7.5 cm

Velocity Profiles at 3 RPM / Y = 7.5 cm

Figure 62: Position 4 IDDES Plot at 3 rpm

Figure 63: Position 4 SST k–ω Plot at 3 rpm

Position 5

Velocity Profiles at 3 RPM / Y = 10.0 cm

Velocity Profiles at 3 RPM / Y = 10.0 cm
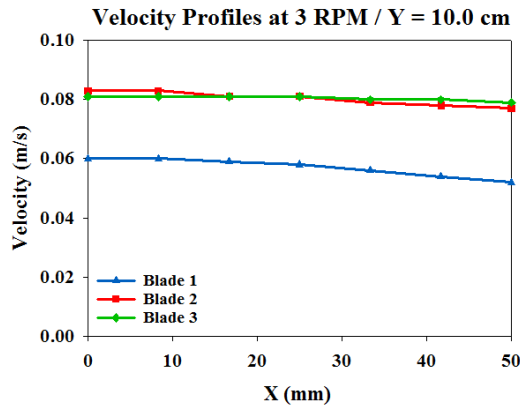
Figure 64: Position 5 IDDES Plot at 3 rpm
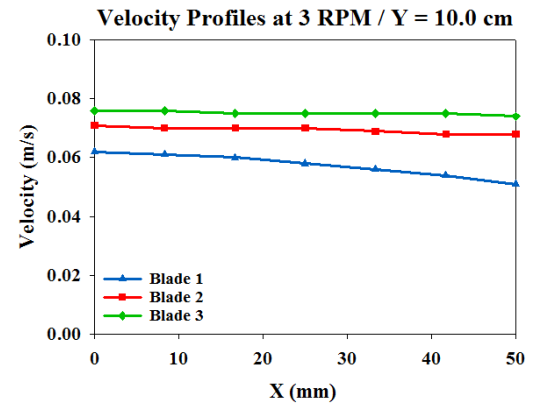
Figure 65: Position 5 SST k–ω Plot at 3 rpm

Table 9: IDDES and SST k–ω Velocity Profiles at 4 rpm

IDDES at 4 rpm	SST k–ω at 4 rpm

Position 1

Velocity Profiles at 4 RPM / Y = 0.0 cm

Velocity Profiles at 4 RPM / Y = 0.0 cm
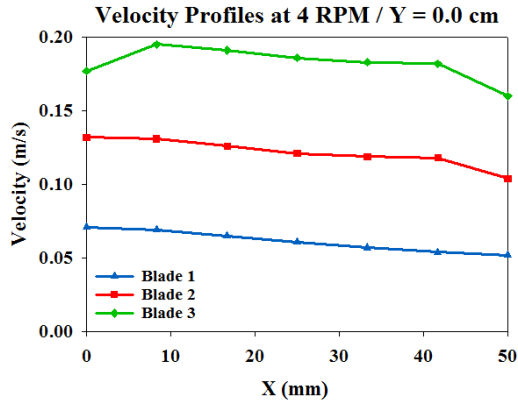
Figure 66: Position 1 IDDES Plot at 4 rpm | **Figure 67: Position 1 SST k–ω Plot at 4 rpm**
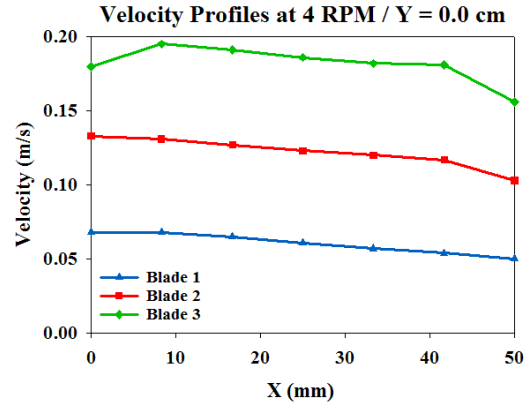
Position 2

Velocity Profiles at 4 RPM / Y = 2.5 cm

Velocity Profiles at 4 RPM / Y = 2.5 cm
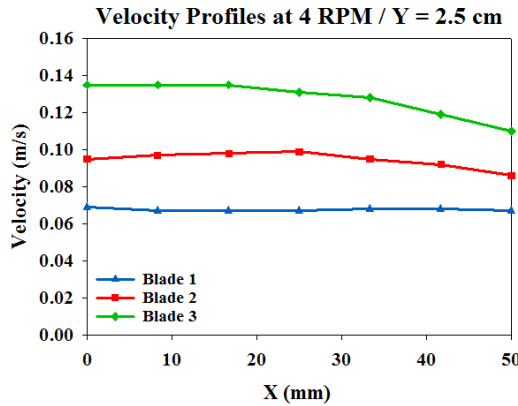
Figure 68: Position 2 IDDES Plot at 4 rpm | **Figure 69: Position 2 SST k–ω Plot at 4 rpm**
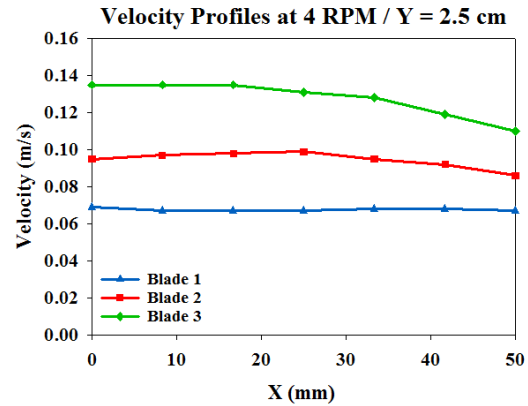
Position 3

Velocity Profiles at 4 RPM / Y = 5.0 cm

Velocity Profiles at 4 RPM / Y = 5.0 cm
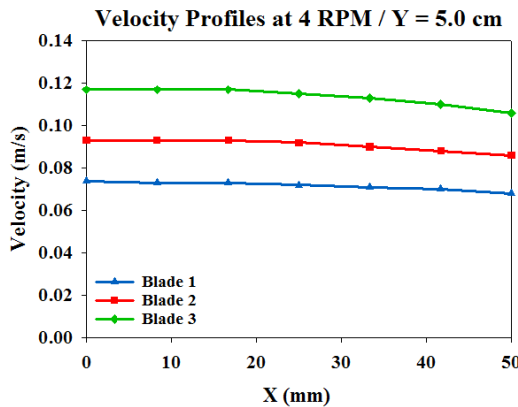
Figure 70: Position 3 IDDES Plot at 4 rpm | **Figure 71: Position 3 SST k–ω Plot at 4 rpm**
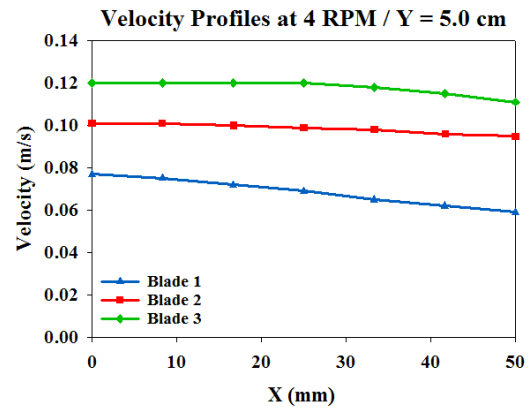
89
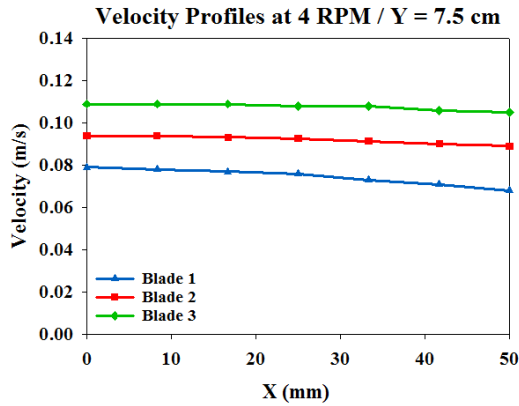
Position 4

Figure 72: Position 4 IDDES Plot at 4 rpm
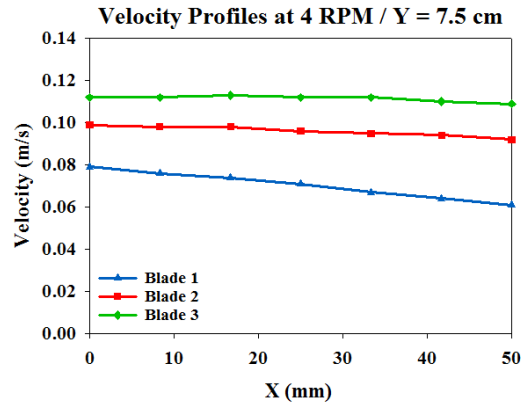
Figure 73: Position 4 SST k–ω Plot at 4 rpm

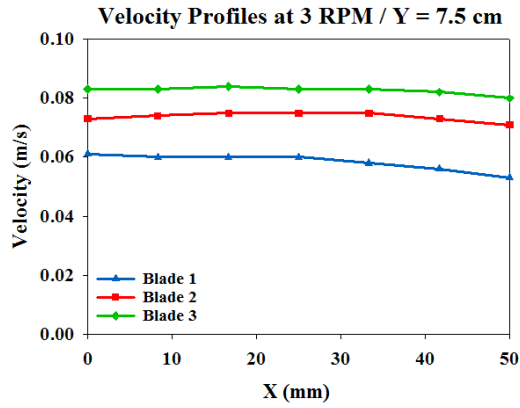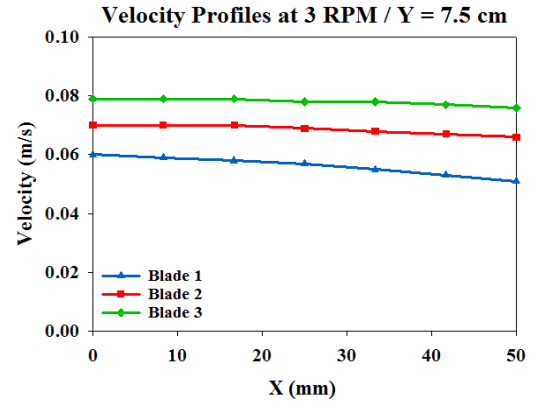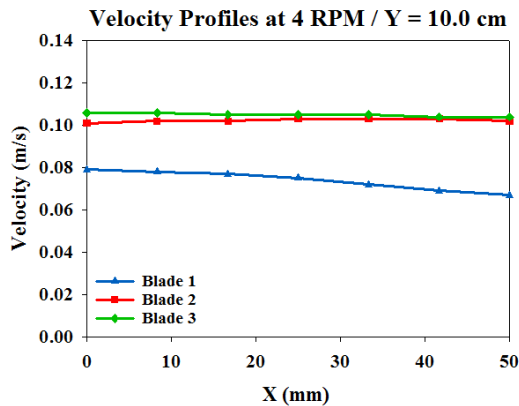## Position 5

Figure 74: Position 5 IDDES Plot at 4 rpm
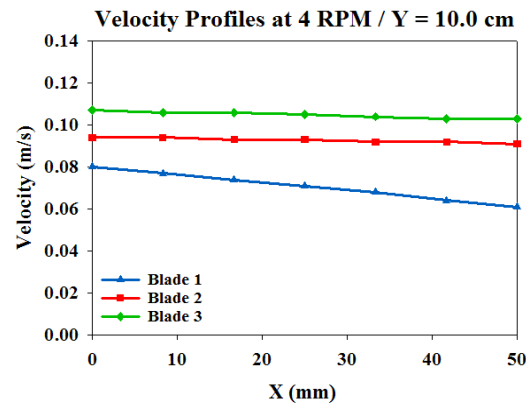
Figure 75: Position 5 SST k–ω Plot at 4 rpm

In the figures of tables 8 and 9, the x axis represents the width of each blade in mm. The origin (0 mm) represents the left periphery of blades, while the end (50 mm) represents the right periphery of blades which are denoted as per figure 43. A primary comparison between the velocity profiles in tables 8 and 9 shows that both turbulence models yield similar plots at each of the rotational speeds. Velocity profile plots at 4 rpm are clearly higher in magnitude yet show the same profile shape for each of the blades as compared to the 3 rpm plots. Starting with blade 1, the figures show that the velocity profile increases from the right periphery of the blade towards the left periphery. Plots from SST

90

k–ω model show profiles with a steeper increases from the right to the left at almost all positions.

The velocity profiles of blades 2 and 3 show similar behavior. At the face of blades, both profiles show a steep increase followed by a uniform velocity magnitude at the middle of the blade. In the case of blade 2, a further increase in magnitude is identified following the uniform location. While, in the case of blade 3, a decrease is identified towards the left periphery of the blade. With increasing height above the blade face, the velocity profiles of blades 2 and 3 start varying similarly. The profiles maintain the steep increase in velocity magnitude starting from the right periphery while proceeding with a uniform magnitude beyond the mid-blade without any further increase or decrease. Starting from a height of 7.5 cm above the blade face, these profiles begin to form a uniform and horizontal shape extending over the entirety of the blade width.

The main difference between the plots of IDDES and SST k–ω for both rotational speeds can be noted by referring to figures 64 and 65, or figures 74 and 75. It can be clearly seen that velocity profiles of blades 2 and 3 from IDDES become uniform at an equal magnitude at position 5. This cannot be identified for the profiles of blades 2 and 3 from SST k–ω. The profiles become completely straight at position 5, however not at the same magnitude exactly. It is important to note that the velocity profiles of blades 2 and 3 from SST k–ω at this position are very close in magnitude at 3 rpm, while show a greater difference at 4 rpm.

Model Validation

CFD provides a practical approach in simulating and investigating flows in numerous scientific practices. However, the accuracy of CFD results depends on numerous factors including meshing and turbulence models used. The validation of CFD results is achieved by comparison of the model results (referred to as the predicted results) with the experimental results (referred to as the observed results). The convergence of results from the two approaches is required to ensure the validity of the CFD model. Once validated, the model can be considered as calibrated against observed experimental measurements, and can be used as a research tool for investigating other aspects of the process at hand.

Referring to the velociy profiles plotted, it was noted that velocity above the blades becomes uniform at a height of 10 cm from the blade face. From this consideration, velocity magnitude data were exported at a vertical line extending from the center of the face of each blade and up to a height of 10 cm upwards as shown below. Thirteen data points were collected, where the distance between consecutive points is 0.85 cm.

Blade 3   **Blade 2**   **Blade 1**
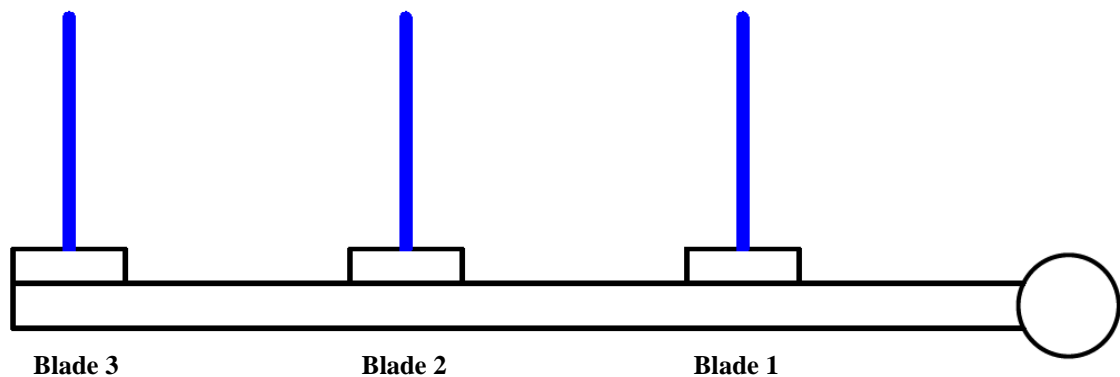
Figure 76: Schematic Showing Location of Velocity Lines Plotted

The height Y is zero at the face of the blade and increases with an increment of 0.85 cm above the blade faces up to 10 cm as shown below.
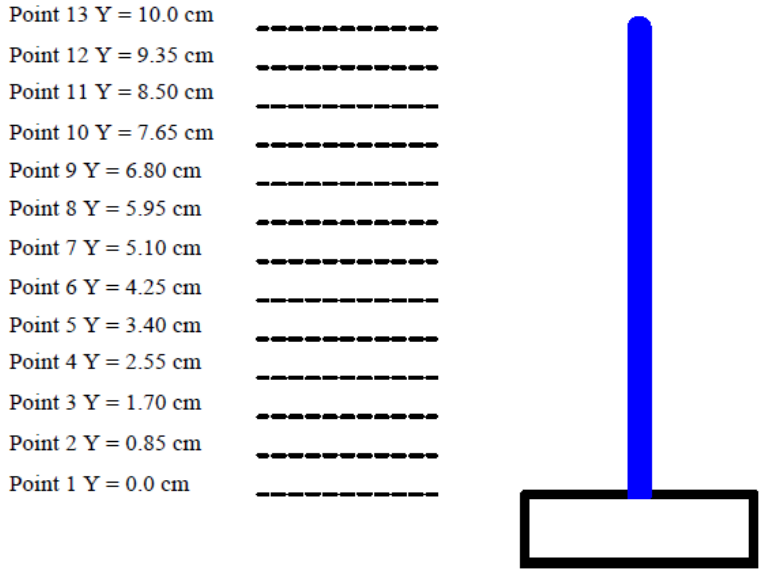
Figure 77: Schematic Showing Data Points' Height
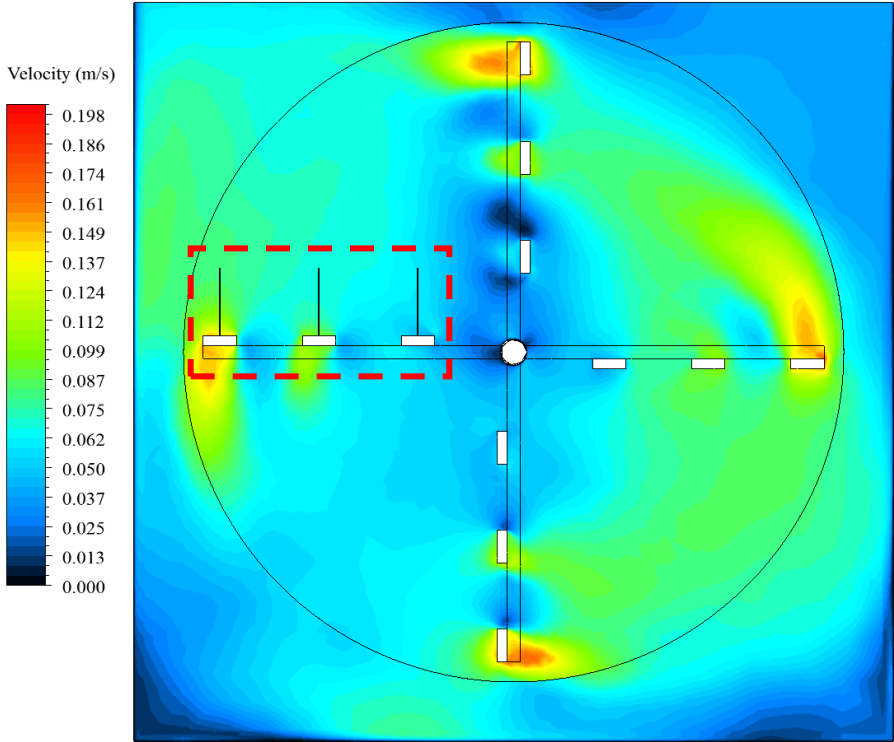
Figure 78: CFD Contour Showing Location of Velocity Lines Plotted

Table 10: PIV and ANSYS Velocity Results per Blade at 3rpm and 4 rpm

N = 3 rpm	N = 4 rpm

PIV and CFD Results above Blade 1
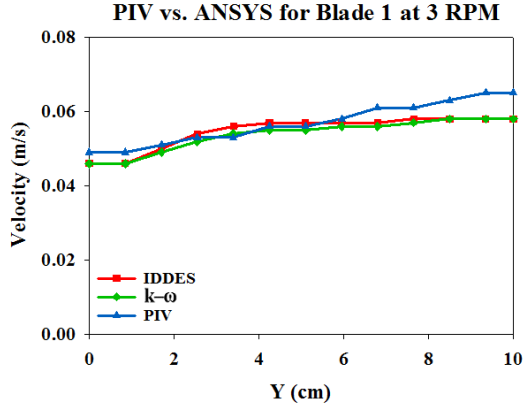
Figure 79: Velocity above Blade 1 at 3 rpm
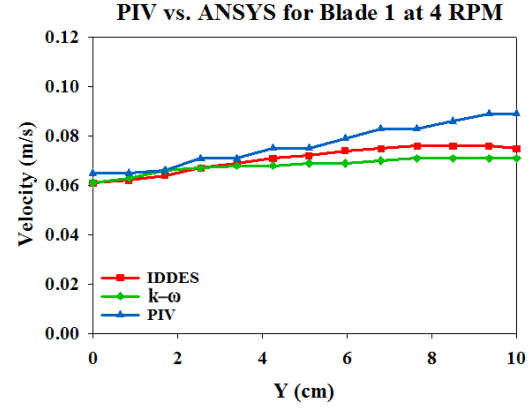
Figure 80: Velocity above Blade 1 at 4 rpm

PIV and CFD Results above Blade 2
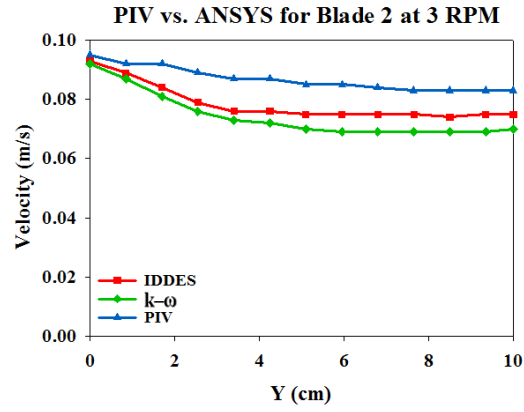
Figure 81: Velocity above Blade 2 at 3 rpm
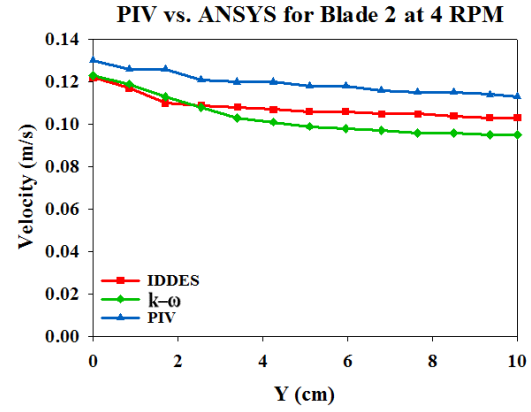
Figure 82: Velocity above Blade 2 at 4 rpm

PIV and CFD Results above Blade 3
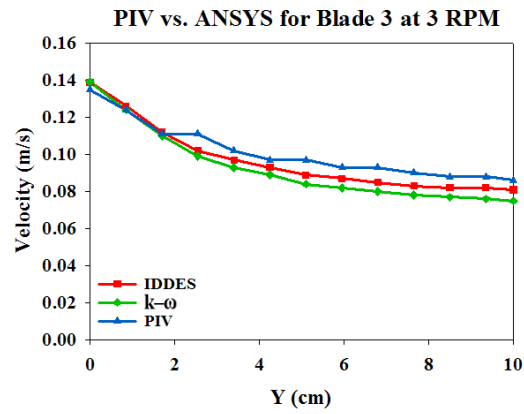
Figure 83: Velocity above Blade 3 at 3 rpm
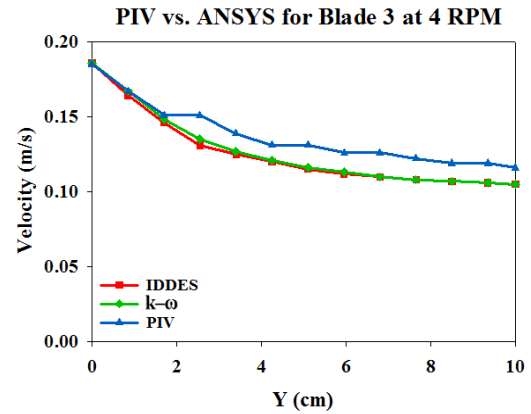
Figure 84: Velocity above Blade 3 at 4 rpm

The graphs of table 10 represent the velocity of water particles along a straight line from the center of the face of each blade extending upwards to a height of 10 cm. Figures 79 through 84 show curves for the 13 velocity points from the experimental approach (PIV results) and the numerical approach (CFD models IDDES and SST k–ω). In the graphs above, the x axis represents the height above blade face starting from the origin which is at the face of the blade and upwards up to $Y = 10$ cm as per figure 77. The y axis represents the velocity of the water particles at each location in m/s.

Investigating figures 79 and 80 related to blade 1, it can be clearly identified that the velocity of water particles is increasing with height above the blade face for both rotational speeds. In general, this is unpredictable since it is expected that water particles loose velocity magnitude with increasing distance away from a rotating plate. The results for this blade are valid because, as explained earlier, the velocity fields show complex flow structures encompassing blade 1 in a swirling motion form. Since the distance between the center of the mixer and centerline of the first blade is 14 cm, this small distance is leading to the formation of a small circular flow. It is presumed that water stirred by the first blade of an arm is rotating downwards onto the first blade of the following arm. Regarding figures 81 through 84 related to blades 2 and 3, the velocity of water particles above the blade faces is decreasing with height as expected. Blade 3 shows a much greater decrease as compared to blade 2.

The graphs above demonstrate that PIV and ANSYS show a very close variation for the velocity of water particles above all the blade faces. Both CFD turbulence models show almost the same variation, where IDDES is more closely matching with the PIV results.

Table 11: PIV and ANSYS Velocity Results for Blades at 3 rpm and 4 rpm

N = 3 rpm	N = 4 rpm

PIV
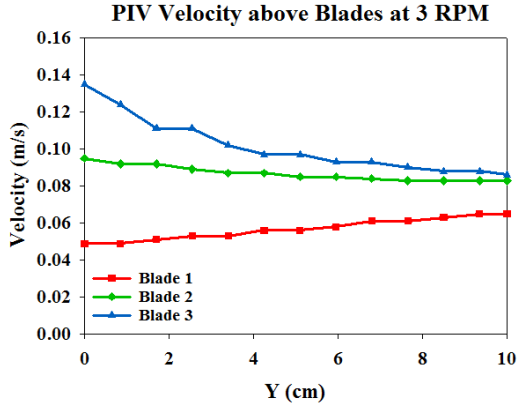
Figure 85: PIV Velocity Results at 3 rpm
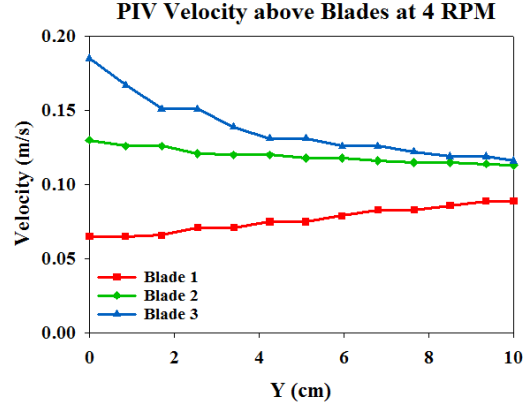
Figure 86: PIV Velocity Results at 4 rpm

IDDES
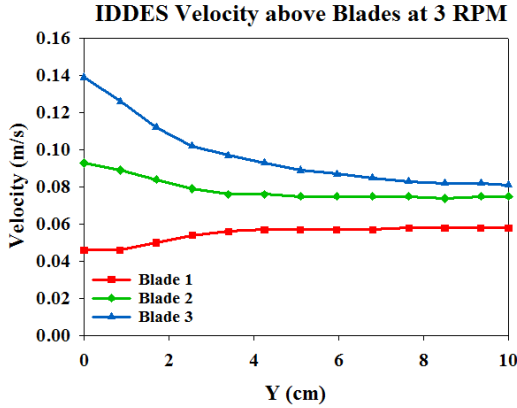
Figure 87: IDDES Velocity Results at 3 rpm
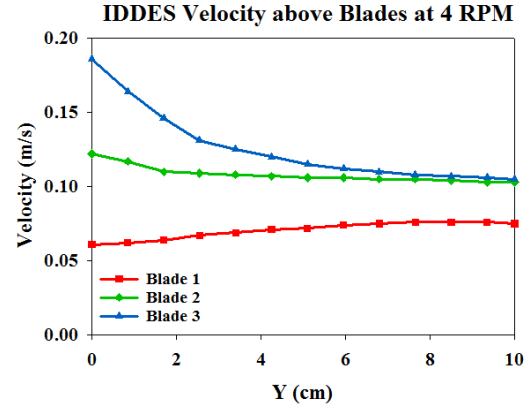
Figure 88: IDDES Velocity Results at 4 rpm

SST k–ω
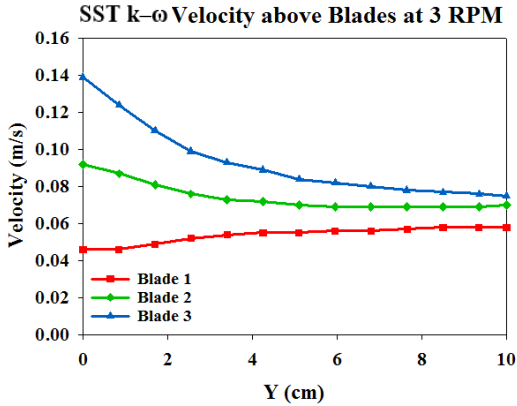
Figure 89: SST k–ω Velocity Results at 4 rpm
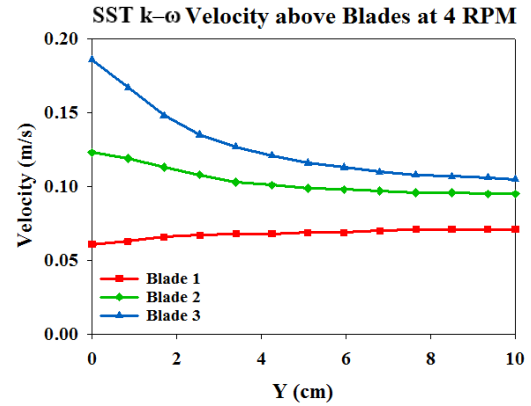
Figure 90: SST k–ω Velocity Results at 4 rpm

The graphs of table 11 show the variation of velocity magnitude above each of the blades represented together for each method and per each rotation. A general overview of the figures demonstrates the same variation in shape and magnitude from the three approaches for both rotational speeds.

In terms of shape, the variation of velocity above the blade faces differs at some locations between the experimental approach and the numerical one. For blade 3, the PIV velocity results shows a steep decrease within a height of 1.8 cm followed by no change in velocity magnitude. The pattern is repeated along the entire height where the slopes become less steep. While, the CFD results show a smoother curve for the decrease in velocity magnitude. IDDES shows a steep decrease within a height of 2.2 cm followed by a smooth decreasing curve. On the other hand, SST k–ω shows a smoother decreasing curve from the blade face up to a height of 10 cm without steep slopes as compared to IDDES. Regarding blades 1 and 2, all three approaches show very similar curves for the velocity variation in terms of shape. CFD approaches show a clearer initial decrease in velocity above blade 2 as compared to PIV graphs.

In terms of magnitude, all figures clearly show that blades 2 and 3 show a decrease in velocity magnitude starting from the blade face upwards, and reach an equal velocity magnitude at a height of 10 cm. The velocity above blade 3 decreases steeply within the first 2 cm from around 0.14 m/s to 0.11 m/s at 3 rpm and 0.19 m/s to 0.15 m/s for 4 rpm. This is not seen above blade 2, where the decrease in velocity magnitude is very incremental. Within a height of 10 cm, the velocity of water particles above blade 3 decreases from 0.14 m/s to 0.09 m/s at 3 rpm and 0.19 m/s to 0.12 m/s at 4 rpm. Whereas, the decrease in velocity magnitude above blade 2 is only 0.01 m/s for both rotational

speeds along the entire height of 10 cm. Therefore, this means that losses in velocity magnitude are much higher at blade 3 as compared to blade 2. This can be due to the fact that since blade 2 is in the middle between the first and third blade, water flows from both sides of blade 2 and joins into the flow above it. From this consideration, it is expected to see larger variations between PIV and CFD results at this blade as compared to the other blades as seen in figures 81 and 82. Flow simulation through CFD does not yield results as close to the experimental results as compared to other locations.

PIV results show that the velocity at a height of 10 cm above the blade faces becomes exactly the same for blades 2 and 3. This can also be seen from the CFD results however minor variations are identified mainly from SST k–ω results.

Regarding blade 1, velocity of water particles increase from the blade face with increasing height. For both rotational speeds, a total increase of around 0.012 m/s is identified. As explained earlier, the location of each of the first blades causes the formation of an inner swirling flow around the center of the mixer. The increase in velocity magnitude above the blade face is reasonable because water particles carried by the first blade of the previous falling downwards combine with the flow above blade 1.

From the figures of tables 10 and 11, satisfactory convergence can be identified between the experimental and numerical approaches. Both CFD turbulence models IDDES and SST k–ω accurately simulate the velocity flow field surrounding the blades. Noting that IDDES is a hybrid model that resolves by using both local grid characteristics and a wall-length scale, the results above show better agreement between PIV and IDDES as compared to PIV and SST k–ω which is expected. Furthermore, a comparison of the velocity profiles plotted from the two approaches is also considered.

A plot of the velocity profiles representing the PIV results and the CFD results (IDDES and SST k–ω) provides a general understanding of the agreement between the two approaches. Velocity profiles at the face of the blades are plotted using data from the three methods, and a good agreement is identified as seen in figures 91 and 92.
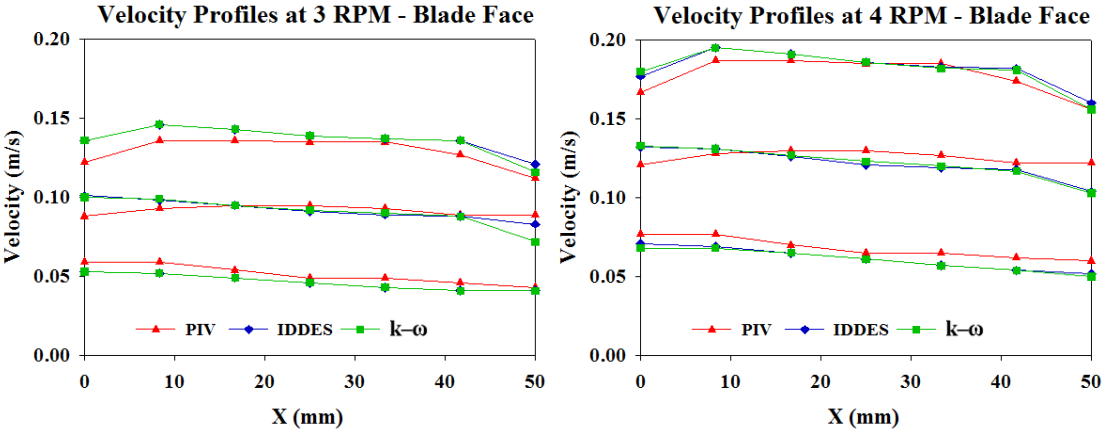
Figure 91: PIV-ANSYS Velocity Plots at 3 rpm   **Figure 92: PIV- ANSYS Velocity Plots at 4 rpm**

However, plotting the velocity profiles is yet another qualitative method for studying the convergence between PIV and CFD results. Furthermore, these graphs would not produce clear comparisons at other increments above the blade face. A quantitative method is needed to study the convergence between PIV and CFD results. Not only so, but to compare the accuracy of the two turbulence models with the experimental results as well. From this consideration, a Goodness-of-Fit evaluation is adopted.

A Goodness-of-Fit evaluation is conducted to study the accuracy of the results from the two approaches. The Goodness-of-Fit evaluation is based on the coefficient of determination R^2 of the linear regression. However, it is important to note that R^2 quantifies the degree of any linear correlation between observed values and predicted ones. This is not the case for a Goodness-of-Fit evaluation.

For this evaluation, one specific linear correlation should be taken into consideration:

$$Y_{observed} = 1 \times Y_{predicted} + 0 \quad \text{i.e. the 1:1 line}$$

The R^2 is a statistic which provides a measure of how well observed outcomes are replicated by a model (predicted outcomes). The R^2 value is the square of the correlation between values of two data sets. The more R^2 tends to 1, the more the variation in the first data set is explained by the variation in the second data set.

The velocity magnitude data exported to plot the velocity profiles above each of the blades for both rotational speeds were used to quantitatively study the convergence between PIV and ANSYS results. Each of the two CFD turbulence model results were compared separately with the PIV results for each rotational speed. Table 12 summarizes the values for the slope of the best fit line, and R^2 for each comparison.

Table 12: Goodness-of-Fit Results

Goodness-of-Fit Results		R²	Slope
N = 3 rpm	IDDES / PIV	0.89	0.92
	SST k–ω / PIV	0.89	0.91
N = 4 rpm	IDDES / PIV	0.89	0.89
	SST k–ω / PIV	0.92	0.89

Figures 93 through 96 show the distribution of PIV-ANSYS data points along with the coefficient of determination, the best fit line along with its slope, and the 45° line.
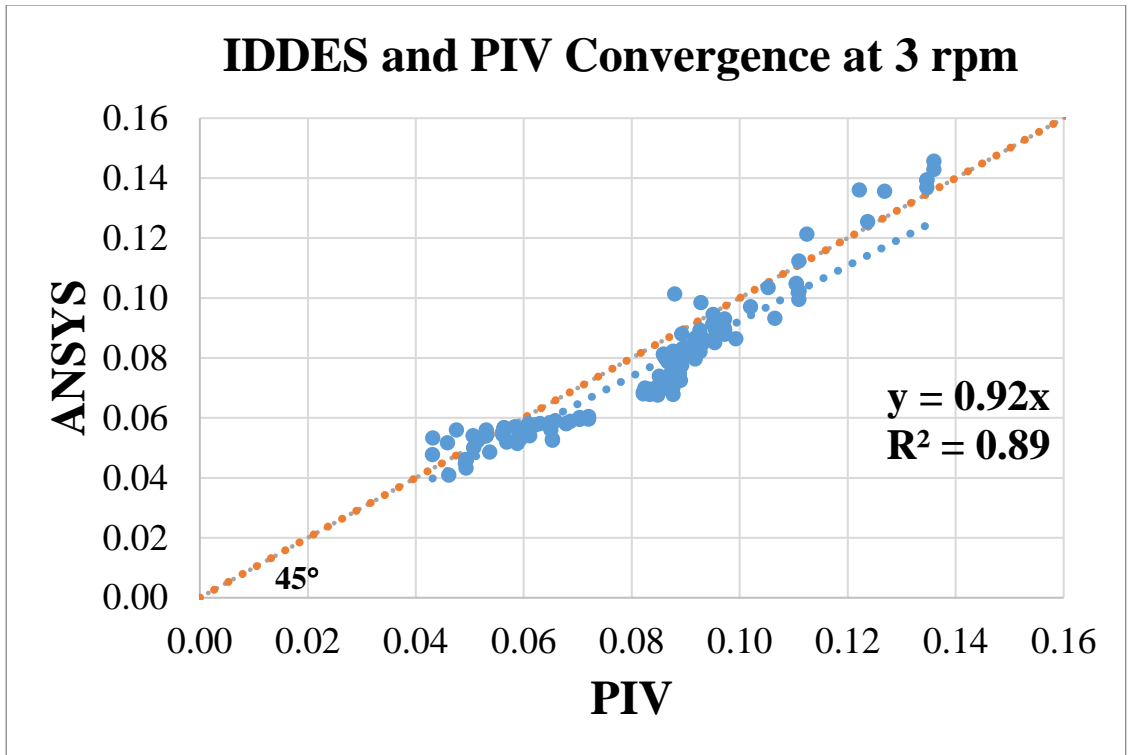
Figure 93: Goodness-of-Fit for IDDES and PIV at 3 rpm
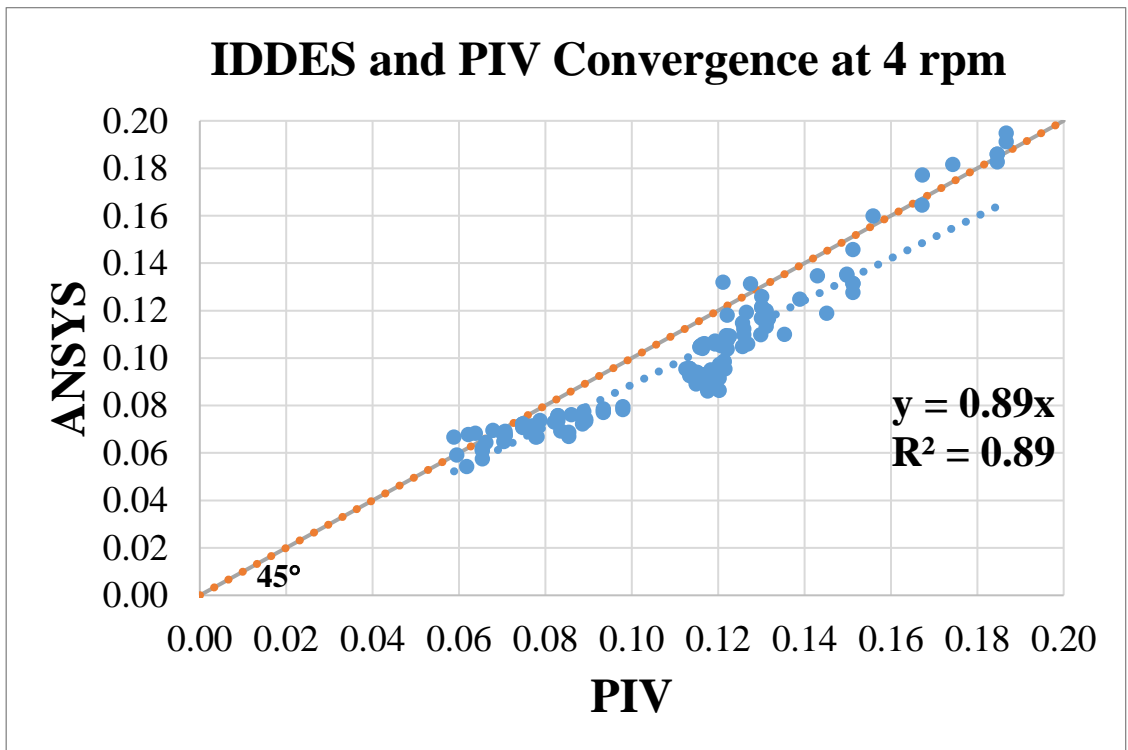
Figure 94: Goodness-of-Fit for IDDES and PIV at 4 rpm
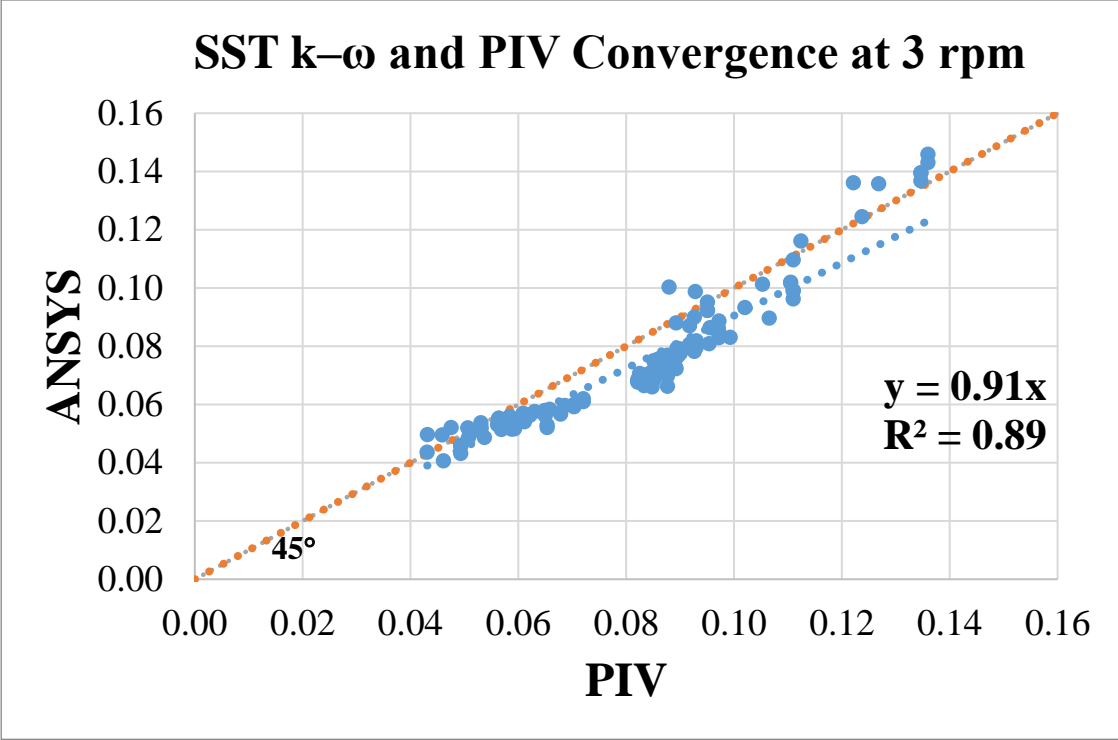
Figure 95: Goodness-of-Fit for SST k–ω and PIV at 3 rpm
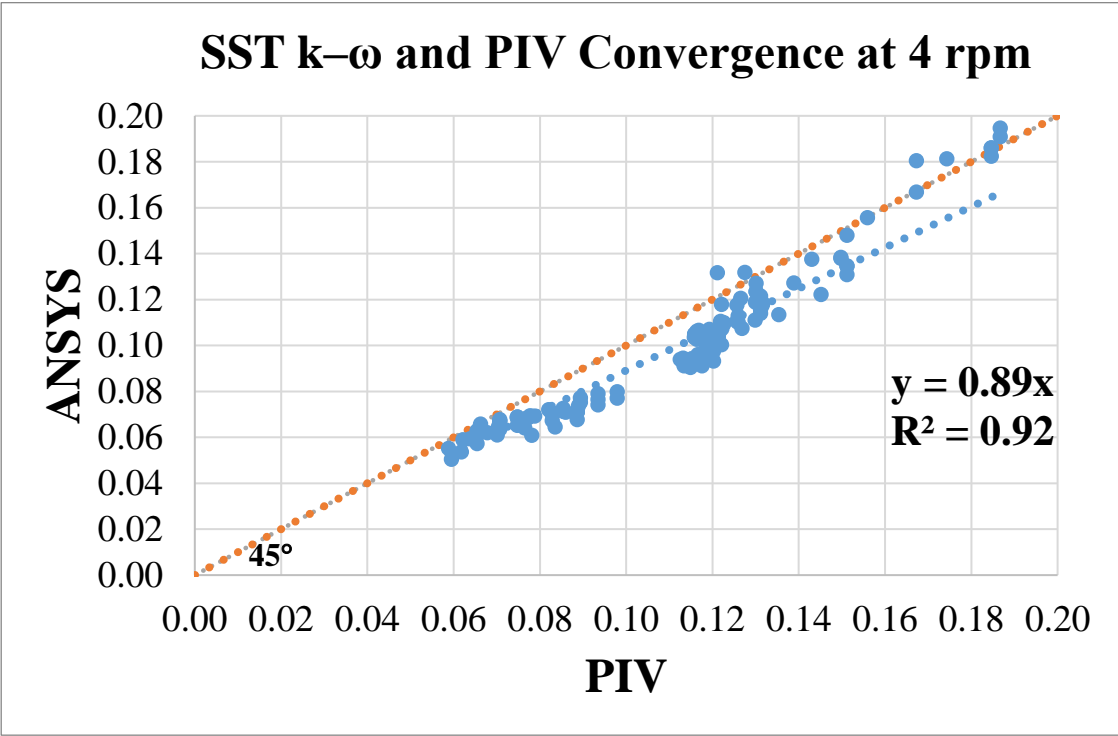
Figure 96: Goodness-of-Fit for SST k–ω and PIV at 4 rpm

The results of the Goodness-of-Fit evaluation show that the coefficient of determination R^2 is equal to around 0.9 (ranges between 0.89 and 0.92). This means that the CFD models well replicated the experimental results, where almost 90 % of the variation in the CFD results is explained by the variation in PIV results. A high value for R^2 allows us to confidently look into the slopes of the best fit lines drawn.

Regarding the IDDES and PIV evaluations, the slope of the best fit line is 0.92 for 3 rpm and 0.89 for 4 rpm. While for the SST k–ω and PIV evaluations, the slope of the best fit line is 0.91 for 3 rpm and 0.89 for 4 rpm. The line having a slope of 1 is the 45° line as plotted in each of the figures. Clearly a slope of 1 means a perfect agreement or correlation between PIV and CFD results which is unlikely. The slope of the best fit line is slightly better for IDDES at 3 rpm (by 0.01), and the same at 4 rpm. Since the slopes are nearly equal to 0.9, and noting again that the coefficient of determination is also almost 0.9, this means that both CFD models show good agreement with the experimental results deeming the models generated valid.

Moreover, the two CFD models produce results at almost the same accuracy when compared to experimental results. It is expected that IDDES would produce more accurate results, however the results are reasonable since flow in the flocculator is not highly turbulent (Reynolds number does not exceed 60,000). The two equation SST k–ω model can be utilized to accurately simulate the flow in paddle flocculators at low rotational speeds (3 rpm and 4 rpm), when the more computationally expensive IDDES model is not feasible.

5.3.4 Slippage Factor k

In flocculation, the efficiency of the process depends on the mixing flow conditions in the basin. In paddle flocculators, since turbulent mixing is achieved by mechanical mixers, the power dissipation or the power input to the water is calculated from the drag force as discussed earlier. The power dissipation is then used to determine the velocity gradient $\overline{G}$, where $\overline{G}$ values for flocculation range between 10 to 60 s^{-1}(Droste, 1997). The power input imparted by horizontal paddles is dependent on the drag force and the relative velocity of the fluid with respect to the blade as follows:

$$P = \frac{C_D A_p \rho v_R^3}{2}$$

Different authors discuss the velocity of the paddle relative to water (v_R) in varying terminology. As mentioned earlier in section 2.2 of the literature review, Thomas Camp (1955) who is the father of flocculation, stated in his research that rotary stirring devices set the liquid in spiral motion with an average angular velocity less than the velocity of the rotors. At that time, Camp discussed that the relative velocity of the stirring blade and of the liquid immediately surrounding the blade was difficult to determine, and thus little was known about the relative velocity of the paddles and the water. Camp noted that if S_o is the speed of the shaft in revolutions per second, then he represented the speed of the water as kS_o in revolutions per second. Camp investigated flocculation hydrodynamics to assess the value of k. In his paper, Camp specified that tests were conducted on flocculation mechanisms at the plant, and the test results showed that water revolves at approximately 24 % to 32 % of the speed of the rotors based on the compartment speeds. The problem here rests in the fact that no information was provided regarding the test

types and methodologies adopted. Also, noting the technological advancements at the time Camp conducted his research, it is evident that tools such as PIV or CFD or other flow visualization and simulation techniques were not current. From this consideration, and from a personal perspective, the tests conducted by Camp are assumed to involve a tracer such as dye or a vacuum bubble. It is presumed that Camp monitored the movement of the subject matter within the flocculation tank to assess a numerical value for k.

The incorporation of k in the power dissipation formula yields the following:

$$P = \frac{C_D A_p \rho [(1 - k)v_p]^3}{2}$$

Where the relative velocity v_R is the difference between the velocity of paddles and the velocity of water. Since the velocity of water is assumed to be less than the velocity of paddles by the factor k, therefore the relative velocity is represented as $(1 - k)v_p$ where v_p is the velocity of paddles. A comprehensive review of the literature in this particular term is summarized in table 13.

Table 13: Values of k from Literature

Reference	Slippage Factor
Bratby et al. (1977)	k = 0.24
Peavy et al. (1986)	k ~ 0.25
Droste (1997)	k = 0.25
Hendricks (2011)	k ~ 0.24 to 0.32
Howe et al. (2012)	k ~ 0.2 to 0.3
Bratby (2016)	k ~ 0.2 to 0.35

In an attempt to determine the slippage factor k for the laboratory scale paddle flocculator, the validated CFD models were considered. The power imparted to water by the mixer is needed to back calculate the value of k. From this determination, the torque coefficient C_m was exported from ANSYS using both turbulence models and for each of the two rotational speeds 3 rpm and 4 rpm. Solution convergence for the torque coefficient was reached when the average C_m value, over one complete rotation, did not differ over the last six consecutive rotations. The relationship between torque or moment, and the torque coefficient exported is shown below.

$$C_m = \frac{Moment}{0.5\rho V^2 Sr}$$

Where: ρ is the reference value for density in Fluent (kg/m^3)

V is the reference value for velocity in Fluent (m/s)

S is the reference value for area in Fluent (m^2)

r is the reference value for length in Fluent (m)

Power is calculated from torque through the angular speed ω as follows:

$$P \ (watts) = T \ (N\text{-}m) \ x \ \omega \ (rad/s)$$

Table 14 summarizes the values of C_m obtained from the CFD models using the two turbulence models, at 3 rpm and 4 rpm, and the corresponding values of torque (T), power imparted by the mixer (P), and the slippage factor (k) calculated accordingly.

Table 14: Calculation of the Slippage Factor

Rotational Speed	CFD Model	C_m (unit less)	T (N-m)	P (watts)	k (unit less)
N = 3 rpm	SST k–ω	1.30	0.80	0.25	0.19
	IDDES	1.35	0.83	0.26	0.18
N = 4 rpm	SST k–ω	2.35	1.44	0.60	0.19
	IDDES	2.42	1.48	0.62	0.18

The results show that each CFD turbulence model produces the same value of k for each of the two rotational speeds. The value of k from the SST k–ω model is slightly higher than that obtained by IDDES. Regardless of the variation, a general value for k can be considered as 0.18 for low rotational speeds such as 3 rpm and 4 rpm.

In the design of paddle flocculators, most authors as mentioned earlier, suggest a value of k ranging between 0.2 and 0.3 in recent books. While, the basis of this recommendation remains Camp's work in 1955, technological advancements must be utilized to better estimate the slippage factor incorporated in the design.

Ambiguity related to the slippage factor is noted in most designs. The outcome of this research study shows that k is equal to 0.18 for low rotational speeds of 3 rpm and 4 rpm. The quantified value of k from this research could be used as an additional guideline in the design of paddle flocculators. This research benefits from advanced scientific tools that Camp lacked in 1955, and adds to his legacy in research related flocculation and flocculation basins.

Chapter Six

Summary, Conclusion, and Recommendations

6.1   Summary and Conclusion

Water treatment is the process of improving water quality to make it acceptable for a certain end use. The entire treatment process must involve the proper performance of all units to ensure optimal treatment of impurities in the influent and the delivery of clean and safe water. Water treatment incorporates physical, chemical, and biological processes. Flocculation is a combination of physical and chemical processes in which larger particles, known as flocs, are formed from smaller particles due to collisions between them. Flocculation is generally achieved through mixing from mechanical or hydraulic devices. The efficiency of flocculation is highly related to the basin hydrodynamics. Hydrodynamics, which is the study of liquids in motion, has been made feasible to study through technological advancements such as PIV and CFD.

The aim of this research is to investigate flocculation hydrodynamics. A laboratory scale paddle flocculator was utilized to examine the velocity flow field surrounding the blades using PIV. Flow simulation was achieved using ANSYS Fluent, and the models generated produced a wholesome understanding of the rotational velocity field. The validation of the CFD models was reached through comparison of velocity results from the two approaches. Satisfactory convergence between the results ensured the validity of the generated models. A comprehensive analysis and discussion of the results obtained allows the following conclusions to be drawn:

- The velocity flow field and streamlines of each of the blades of the laboratory scale paddle flocculator show the same vector behavior and flow structures at a rotational speed of 3 rpm and 4 rpm, with accordingly higher magnitudes at 4 rpm.

- The velocity profiles of blade 1 at both rotational speeds increases from the right periphery of the blade towards the left one. The profile shape does not vary with increasing height above the blade face, and velocity magnitude increases with height. This increase is related to the fact that the first blade of all arms is encompassed in a swirling or re-circulating flow formed at the center of the mixer.

- The velocity profiles of blades 2 and 3 at both rotational speeds show a similar shape which flattens and becomes completely straight with increasing height above the face of the blades. Velocity magnitude decreases with height, and at a height of 10 cm from blade face, the profiles are at equal magnitude indicating the uniformity of flow.

- The velocity contours exported from the two CFD turbulence models IDDES and SST k–ω do not show any major differences. The only difference noted is the higher velocity carried beneath each of blades 3 from SST k–ω.

- The velocity contours from each of IDDES and SST k–ω are similar for the two rotational speeds, with accordingly higher velocity magnitude at 4 rpm.

- Velocity contours from both models show complex flow structures at the center of the mixer encompassing the first blade of the four arms. A swirling form of flow is identified at the location, spreading more towards the left of the mixer.

- Both models show a detachment of the rotational flow in the third quadrant, which is at the bottom left. IDDES contours show that the detachment zone incorporates

locations with very low velocity due to low velocity flow joining in from the corner and the inner swirling flow of the first blades.

- The qualitative and quantitative methods used for the validation of the CFD models against the PIV experimental results show a good agreement between the two approaches. Plots for the variation of velocity above blade faces from both approaches show curves with similar shapes and magnitude thus validating the models generated with satisfactory convergence.

- Both approaches show that the velocity of water particles above blade 3 decreases steeply and fundamentally loosing between 0.05 m/s to 0.07 m/s of its magnitude within a height of 10 cm. The velocity of water particles above blade 2 decreases gradually and incrementally losing only 0.01 m/s of its magnitude. Blade 1 shows an increase in velocity magnitude above the face due to its location near the center.

- A Goodness-of-Fit evaluation shows that the coefficient of determination R^2 is almost 0.9 for both models. The slopes of the best fit lines for both models are also around 0.9 for both rotational speeds indicating that these turbulence models accurately predict the flow inside the flocculator. Results of this evaluation also show that IDDES provides very slight improvement against SST k–ω, yielding the latter sufficient in accurately simulating the flow inside the flocculator. This is explained by noting the low levels of turbulence in the flocculator.

- The validation of the CFD models allows the calculation of the slippage factor k by determining the power imparted by the mixer to the water body. IDDES yields a slippage factor of 0.18 which is slightly lower than that obtained by SST k–ω which is 0.19. These values are constant for the two rotational speeds.

- The slippage factors calculated fall below the range recommended by Camp which is 0.24 to 0.32 or the range recommended by most books which is 0.2 to 0.3. The quantified value of k from this research could be used as an additional guideline in the design of paddle flocculators.

The slippage factor found through this research indicates that the relative velocity of paddles with respect to the fluid (v_R), is higher than what is indicated in most designs. This means that the mixer of the paddle flocculator is imparting more power to the water body, and therefore higher than expected velocity gradients are achieved for the same rotational speed. In terms of energy and sustainability, reduced mixing times or lower rotational speeds could be adopted in the operation of paddle flocculators while still achieving sufficient mixing and velocity gradient values for flocculation. As a result, the electric consumption of motors of a flocculation unit at a drinking water treatment plant could be potentially decreased.

6.2 Recommendations for Future Work

Since any research study is defined by its scope of work, not all related questions can be answered. This research aimed at investigating flocculation hydrodynamics in a laboratory scale paddle flocculator and forming a quantitative assessment of the slippage factor. From this consideration, future research could include the following:

- Utilizing the validated CFD models to study design recommendations of paddle flocculators by varying the number of blades per arm.

- Utilizing the validated CFD models to study the floc size distribution under different hydrodynamic and physical conditions.

- Developing CFD models of compartmentalized paddle flocculators for the determination of the slippage factor as a function of each compartment with varying rotating speeds.

- Investigating the impact of shear conditions during initial floc formation on floc size after breakage and regrowth in paddle flocculators.

References

Adrian, R. J. (2005). Twenty years of particle image velocimetry. *Experiments in Fluids, 39: 159-169.* DOI 10.1007/s00348-005-0991-7.

ANSYS Academic v 19.1, ANSYS Inc., www.ansys.com

ANSYS Fluent User's Guide, ANSYS Inc., Canonsburg, PA, November, 2013.

Bratby, J. (2016*). Coagulation and flocculation in water and wastewater treatment*. IWA Publishing.

Bratby, J., Miller, M. W., & Marais, G. (1977). Design of flocculation systems from batch test data. *Water SA, 3*(4), 173-182.

Bridgeman, J., Jefferson, B., & Parsons, S. (2008). Assessing floc strength using CFD to improve organics removal. *Chemical Engineering Research and Design, 86*(8), 941-950.

Bridgeman, J., Jefferson, B., & Parsons, S. A. (2009). Computational fluid dynamics modelling of flocculation in water treatment: A review. *Engineering Applications of Computational Fluid Mechanics, 3*(2), 220-241.

Bridgeman, J., Jefferson, B., & Parsons, S. A. (2010). The development and application of CFD models for water treatment flocculators. *Advances in Engineering Software, 41*(1), 99-109.

Camp, T. (1955). Flocculation and flocculation basins. *American Society of Civil Engineers Library, 120*, 1-16.

Coufort, C., Bouyer, D., & LinÃ, A. (2005). Flocculation related to local hydrodynamics in a Taylor-Couette reactor and in a jar. *Chemical Engineering Science; 5th International Symposium on Mixing in Industrial Processes (ISMIP5), 60*(8), 2179-2192.

Crittenden, J. C. (2012). *Water Treatment: Principles and Design*. J. Wiley & Sons.

DaVis 8.4 Software, LaVision GmbH, Göttingen, Germany, July 4, 2017. Available: www.lavision.com

Double-pulse Nd: YAG, LaVision GmbH, Göttingen, Germany, January 18, 2017. Available: www.lavision.com

Droste, R. L. (1997). *Theory and practice of water and wastewater treatment*. New York, N.Y: J. Wiley & Sons.

Flow Master Getting Started, LaVision GmbH, Göttingen, Germany, March 6, 2017. Available: www.lavision.com

Flow Master, LaVision GmbH, Göttingen, Germany, January 20, 2017. Available: www.lavision.com

Gregory, J. (2009). Monitoring particle aggregation processes. *Advances in Colloid and Interface Science, 147*, 109-123

Hendricks, D. W. (2011). *Fundamentals of Water Treatment Unit Processes: Physical, Chemical, and Biological.* CRC Press.

Howe, K. J., et al. (2012). *Principles of Water Treatment*. J. Wiley & Sons.

Imager pro plus & Imager pro X, LaVision GmbH, Göttingen, Germany, April 11, 2017. Available: www.lavision.com

Imaging Tools, LaVision GmbH, Göttingen, Germany, January 4, 2017. Available: www.lavision.com

Jarvis, P., Jefferson, B., & Parsons, S. (2004). The duplicity of floc strength. *Water Science and Technology: A Journal of the International Association on Water Pollution Research, 50*(12), 63-70.

Jarvis, P., Jefferson, B., Gregory, J., & Parsons, S. A. (2005). A review of floc strength and breakage. *Water Research, 39*(14), 3121-3137.

Oyegbile, B., Ay, P., & Satyanarayana, N. (2016). Flocculation kinetics and hydrodynamic 1interactions in natural and engineered flow systems: A review. *Environmental Engineering Research, 21*(1), 1-14.

Programmable Timing Unit (PTU X), LaVision GmbH, Göttingen, Germany, March 17, 2017. Available: www.lavision.com

Rowe, D. R., Tchobanoglous, G., & Peavy, H. S. (1985). *Environmental engineering*. Singapore, McGraw-Hill.

Tu, J., Yeoh, G. H., Liu, C. (2013). *Computational fluid dynamics: a practical approach* (2nd edition). Elsevier/Butterworth-Heinemann.

U.S. Environmental Protection Agency. Office of Water. (2000). The History of Drinking Water Treatment. (EPA-816-F-00-006). *Retrieved from:* https://www.epa.gov/

U.S. Environmental Protection Agency. State and Local Climate and Energy Program. (2013). Energy Efficiency in Water and Wastewater Facilities. Local Government Climate and Energy Strategy Series. *Retrieved from:* https://www.epa.gov/

Wang, L. K., & Shammas, N. K. (2015). *Water Engineering: Hydraulics, distribution, and treatment.* Hoboken, N.J: J. Wiley & Sons.

Wulf, W. A. (2000). *Great Achievements and Grand Challenges.* The Bridge, 30(3&4), 6-11.

Xiao, F., Lam, K. M., Li, X. Y., Zhong, R. S., & Zhang, X. H. (2011). PIV characterisation of flocculation dynamics and floc structure in water treatment. *Colloids and Surfaces A: Physicochemical and Engineering Aspects, 379*(1), 27-35.

Xiao, F., Li, X. Y., & Lam, K. M. (2007). Investigation of the hydrodynamic behaviour of particles and aggregates by particle image velocimetry. *Water Science & Technology: Water Supply, 7*(2), 213-220.

Yu, W., Gregory, J., Campos, L., & Li, G. (2011). The role of mixing conditions on floc growth, breakage and re-growth. *Chemical Engineering Journal, 171*(2), 425-430.

Yukselen, M. A., & Gregory, J. (2004). The effect of rapid mixing on the break-up and re-formation of flocs. *Journal of Chemical Technology & Biotechnology, 79*(7), 782-788.

Zhong, R. S., Zhang, X. H., Xiao, F., & Li, X. Y. (2011). Effects of humic acid on recoverability and fractal structure of alum-kaolin flocs. *Journal of Environmental Sciences (China), 23*(5), 731-737.

Appendix A

LaVision PIV System

The PIV system used to perform the experiments of this research is a standard system provided by LaVision composed of the components listed below.

1. Illumination System

A laser system is used as an illumination source for PIV. The laser system is a double oscillator Q-switched Nd: YAG laser that produces infrared laser light at a wavelength of 1064 nm. All lasers consist of three main components which are the laser material, the pump source, and the oscillator. In the case of the Nd: YAG laser, the laser material is a YAG (yttrium aluminum garnet) crystal in which Nd^{3+} ions are incorporated. The pump is usually a krypton flash lamp or a smaller semiconductor laser. The resonator is a set of high reflective mirrors, usually in a stable configuration in order to generate a Gaussian beam profile.
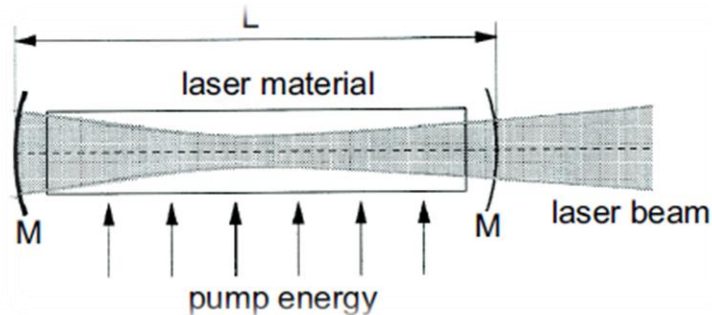

Figure 97: Nd: YAG Laser for PIV Systems

The double pulsed Nd: YAG laser is provided by Litron Lasers, a manufacturer of pulsed and CW Nd: YAG and Nd: YLF lasers. Litron PIV laser systems are twin head devices, which means that the PIV laser head contains two totally independent lasers. The Litron

PIV laser used is a class 4 laser product having a maximum output of 800 mJ, a pulse duration of 4 ns, and a wavelength of 1064 nm - 532 nm. Because the PIV camera is not sensitive to near infrared light, a harmonic generator is used to convert the laser light to a visible green light having a wavelength of 532nm. The use of two independent laser oscillators allows the generation of double pulse outputs with an inter-pulse separation time of less than 1 ns. Two laser outputs are combined by polarizers just before the harmonic generator, which are then used with a single set of external optics. Each laser cavity is operated in single Q-switch mode. The delay between the laser flash from cavity 1 and cavity 2 resembles the time between two images capturing particle positions. An illustration of the principle of a double oscillator Q switched laser can be seen below.
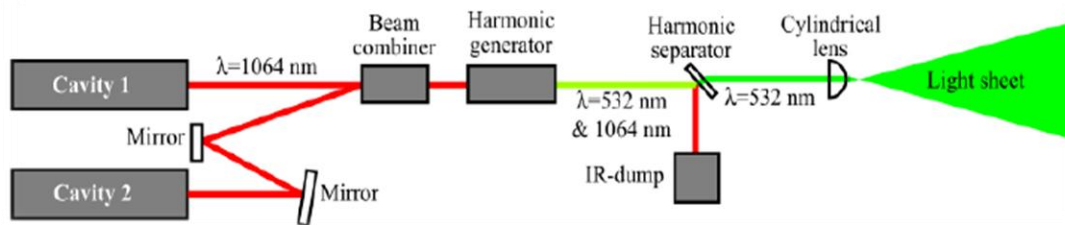

Figure 98: Double Oscillator Q Switched Laser

The laser system consists of three components which are the laser head, an integrated power supply, and a manual remote control box as seen below.

Figure 99: A PIV Power Supply and Control Unit   **Figure 100: A PIV Laser Head**

117

The laser head is the main component of the system comprised of laser oscillators, the 1064 nm polarization beam combination optics, and the 532 nm harmonic generation and separation optics. The integrated power supply is a self-contained unit comprising the control, power, and cooling units. Lastly, the laser functionality is controlled by a manual remote control box. The laser beam coming out from the laser system has an axisymmetric shape. To generate a planar light sheet, a light sheet optics must be connected to the laser system. The main components of light sheet optics are cylindrical lenses that focus the light sheet to a certain thickness and field angle.

2. Image Acquisition Unit

A CCD camera is used to capture the position of particles in the flow field illuminated by the laser sheet. The image acquisition unit consists of the LaVision Imager Pro X 2M which is a CCD camera with a digital image output, a separate control unit, and DaVis software for data acquisition and processing (to be discussed in the following section).

Figure 101: Imager Pro X 2M PIV Camera

CCD is an electronic sensor that converts light into electric charge. CCD cameras comprise of an array of detectors called pixels. The Imager Pro X 2M camera can record images with a maximum resolution of 1600 x 1200 pixels. When seed particles are small, or the light intensity is low, the camera needs to have a high sensitivity to incoming light.

The sensitivity of a CCD camera is evaluated by Quantum Efficiency (the percentage of photons hitting a photo-reactive device that produces charge carriers, measured in electrons per photon). The brightness of the picture is determined by an f-number. The f-number is a dimensionless number that is a quantitative measure of lens speed. It is the ratio of the system's focal length (f) to the diameter of the entrance pupil (D). Disregarding differences in light transmission efficiency, a lens with a greater f-number produces darker images. The Imager Pro X is accompanied with a camera controller connected to the power socket of the camera head for its operation.

The Imager Pro X CCD camera can operate at three different modes as follows.

Single frame and one reference time: This mode allows to take a single frame image. The exposure time can be selected and the image acquisition is synchronized to one reference time. This allows to use a triggered light source to illuminate the object."

Single frame and two reference times: This mode allows to take a single frame image. The exposure time can be selected and the image acquisition is synchronized to two reference times. The exposure time in this operating mode has at least the same value as the dt that determines the delay between the two reference times. This allows to use a triggered light source to illuminate the object twice during the exposure time of the image.

Double frame and two reference times: This mode allows to take a double frame image. The exposure time is given internally. The image acquisition is synchronized to two reference times. In this case the first frame is synchronized to reference time one and the second frame is synchronized to reference time two. The delay between the two reference times is given by the dt**.** This allows to use two separately triggered light sources to

illuminate the object. Light source one for the first frame and light source two for the second frame.

The **double frame and two reference times** mode is selected for the camera operation as it is the basis of operation for a PIV system.

3. System Calibration Tool

In order to determine the location of minute particles in a 3 D volume, it is vital to have an accurate calibration of the PIV system. The calibration process must be carried out with optimum accuracy and under the exact same conditions in which the experiments are conducted. The calibration of the PIV system in this case was achieved by using the LaVision 3D Type 11 calibration plate. The calibration plate is a 100 mm x 100 mm black aluminum plate with numerous precision dots. The diameter of said precision dots is 2.2 mm and the spacing between them is 10 mm. The plate surface has regular grooves to create a surface that represents two parallel planes of dots (a top level and a bottom level) with a plane to plane distance of 2 mm as seen below. Davis 8.4 performs the calibration process, which is discussed in a separate section, by relating each pixel to the line cut through the measurement volume.

Figure 102: PIV 3D Type 11 Calibration Plate

Calibration Process

The calibration conditions must be exactly the same as the conditions in which the experiment are conducted. Prior to proceeding with the calibration steps, the arrangement of the light sheet optics must be modified such that the laser sheet is directed exactly on the calibration plate creating a planar light sheet at its face.

The following steps are completed to achieve the proper calibration of the PIV system:

1. The experimental setup is defined by the selection of one camera calibration.

2. The coordinate system is defined by the selecting of one view (for one camera), and the axis orientation is identified where the lower left corner of the calibration plate (Type 11 3D) is the center of the coordinate system.

3. Four clear images are acquired of the calibration plate and averaged.

4. Three start marks (origin, x – axis, y – axis) are identified, as shown below, as a seed for the mark search which is achieved automatically by the software.
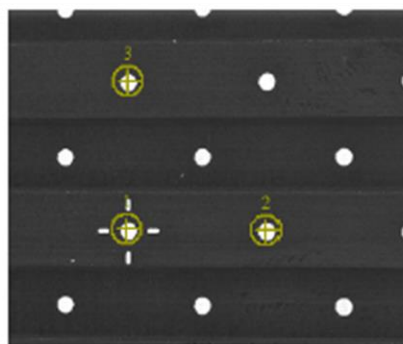

Figure 103: Identification of Start Marks on Calibration Plate

5. Calibration mapping function is fitted to the marks found in the image and the automatic calculation process begins.

6. Evaluation of the corrected images is the last step, to assess the fit results visually. A grid of the ideal regular gird marks is overlaid in red, where this grid should pass through the center of all marks.
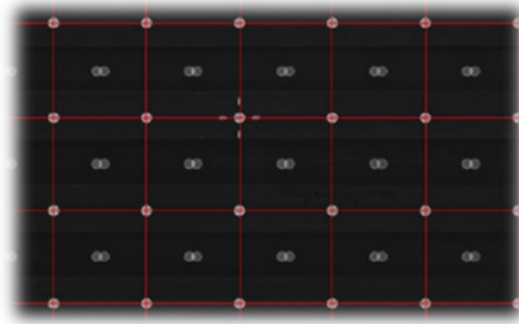

Figure 104: Grid Marks on Calibration Plate

4. Data Acquisition and Processing Unit

LaVision follows its philosophy of intelligent laser imaging with the DaVis software platform. DaVis 8.4 is a multifunctional package which contains tools for calibration, recording, plotting, and processing of acquired data. DaVis 8.4 is designed for Windows 7 SP 1 (32/64 bit) and it supports a variety of new hardware components, such as the latest technology sCMOS and High Speed cameras, and impresses with a significant processing speed boost. However, the software needs to cooperate with a synchronization unit such that the camera and the laser are synchronized to capture PIV images with a specified time difference.

LaVision's completely software controlled synchronization unit is the Programmable Timing Unit (PTU X). It is an embedded system for generation of complex patterns of pulses with highly accurate timing on multiple outputs. The pulse width and the interval between pulses are programmed automatically by DaVis. The microprocessor controlled

timing sequence can be started by an external trigger or constantly generated by an internal frequency set at a specified laser repetition rate. The PTU X takes control over the synchronization of all the devices connected to it in order to accomplish synchronized data readout from all sources of a PIV system.

The **trigger rate** is the rate that is generated by the PTU and sent to the different devices. The **recording rate** is the rate that the system is using to take images. The system is able to send trigger signals at a higher rate than it is taking images with, but the trigger rate needs to be a multiple of the recording rate.

Subsequently, there are three trigger source types, which are summarized below.

Internal trigger: this mode is used if the recording does not need to be synchronized to an external trigger signal that is generated by the experimental setup. Usually this is the case for steady phenomenon that should be observed. The timing is determined by the values that are selected for Trigger rate and Recording rate. The value for the trigger rate is programmed as soon its value in the corresponding textbox is confirmed and the image acquisition at the selected recording rate is started.

Before moving on to external trigger types it is important to note that the PTU X is able to receive external trigger signals from the experiment to phase-lock the recording to an external event. This is done by connecting the external trigger signal to the Trigger BNC of the PTU slot bracket.

External Cyclic trigger: this mode is selected for phase-locked acquisition of each single image with respect to a periodic external trigger signal. In this case the system can calculate a trigger strategy for image acquisition and usually goes for the lowest common

multiple of external trigger and allowable trigger rates of the used devices. The external trigger signal must be a TTL signal with positive logic (0 V →5 V) and a gate of ≥ 1 μs.
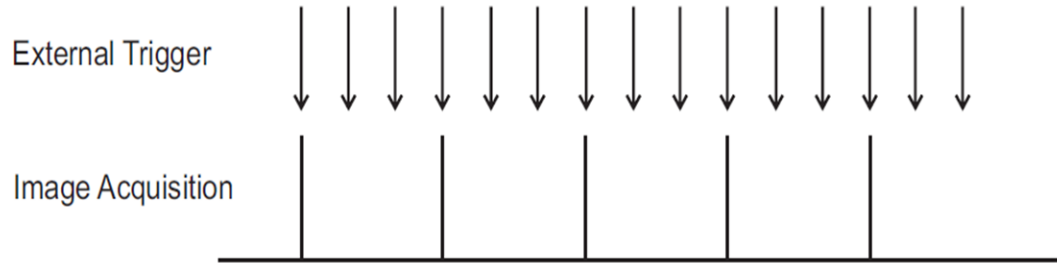

Figure 105: External Cyclic Trigger Signal

External Random trigger: this mode can be selected for phase-locked acquisition of each single image with respect to an external trigger signal that is not periodic. In this case the system has no chance to calculate a trigger strategy for image acquisition. If the external trigger signals come with a delay that is shorter than the required time for the acquisition of one recording it can happen that some external trigger signals will not start a recording. This mode requires a PTU-controlled light source that can be triggered at a range that has no lower limit, i.e. an allowable frequency range between 0 Hz and a maximum frequency. The external trigger signal must be a TTL signal with positive logic (0 V →5 V) and a gate of ≥ 1 μs.
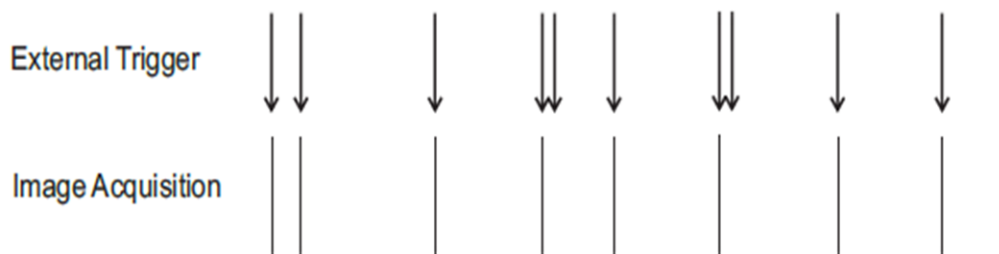

Figure 106: External Random Trigger Signal

Appendix B

Flocculator Design Calculations

1. **Flocculator Dimensions**

   ✓ Diameter of horizontal shaft = 4 cm

   ✓ Width of blade = 5 cm

   ✓ Length of arm = 10 + 5 + 10 + 5 + 10 + 5 = 45 cm

   ✓ Diameter of paddle wheel = 2 x 45 + 4 = 94 cm

   ➢ **Minimum width = 94 + 10 + 10 = 114 cm**

   ➢ **Minimum depth = 94 + 10 + 40 = 144 cm**

   ✓ Length of blade = 50 cm

   ✓ Spacing between the two paddle wheels = 14 cm

   ✓ Length of horizontal shaft = 10 + 50 + 14 + 50 + 10 = 134 cm

   ➢ **Minimum length = 134 cm**

   ✓ V = 110 x (140 - 3) x (120 - 3) = 1,763,190 cm^3 = 1.763 m^3

2. **Power Imparted to Water**

The power input to the water by the paddles is given by:

$$P = \frac{C_D A_p \rho v_R{}^3}{2}$$

- A_{Blades}= 2 paddle wheels x 4 $\frac{\text{arms}}{\text{paddle wheel}}$ x 3 $\frac{\text{blades}}{\text{arm}}$ x 0.5 x 0.05 = 0.6 m^2

- Where A_p is one third of the area of blades, A_p= $\frac{0.6 \text{ m}^2}{3}$ = 0.2 m^2

- Blade length to width ratio: L / W = 50 / 0.05 = 10 → C_D ~ 1.3.

- Relative velocity of blades: $v_R = 0.75 \frac{2\pi rN}{60}$

Where: r is the distance to centerline of paddle from center of rotation (m)

     N is the shaft rotational speed (rpm)

- $r_{\text{Inside Blade}}$ = 2 + 10 + 2.5 = 14.5 cm = 0.145 m

- $r_{\text{Middle Blade}}$ = 2 + 10 + 5 + 10 + 2.5 = 29.5 cm = 0.295 m

- $r_{\text{Outside Blade}}$ = 2 + 10 + 5 + 10 + 5 + 10 + 2.5 = 44.5 cm = 0.445 m

Also a slippage factor k of 0.25 is adopted as per most designs. That is, the speed of the blades relative to the water will be 75 % of the blade speed (0.75 accounts for this adjustment).

N = 3 rpm

$$P = \frac{C_D A_p \rho}{2}(v_{\text{Inside Blade}}{}^3 + v_{\text{Middle Blade}}{}^3 + v_{\text{Outside Blade}}{}^3)$$

$$P = \frac{C_D A_p \rho}{2}\left[\frac{2\pi N(0.75)}{60}\right]^3 (r_{\text{Inside Blade}}{}^3 + r_{\text{Middle Blade}}{}^3 + r_{\text{Outside Blade}}{}^3)$$

$$P = \frac{(1.3)(0.2)(1000)}{2}\left[\frac{2\pi(3)(0.75)}{60}\right]^3 (0.145^3 + 0.295^3 + 0.445^3)$$

$$P = 0.198 = 0.2 \text{ Watts}$$

N = 4 rpm

$$P = \frac{C_D A_p \rho}{2} \left(v_{\text{Inside Blade}}^3 + v_{\text{Middle Blade}}^3 + v_{\text{Outside Blade}}^3 \right)$$

$$P = \frac{C_D A_p \rho}{2} \left[\frac{2\pi N(0.75)}{60} \right]^3 \left(r_{\text{Inside Blade}}^3 + r_{\text{Middle Blade}}^3 + r_{\text{Outside Blade}}^3 \right)$$

$$P = \frac{(1.3)(0.2)(1000)}{2} \left[\frac{2\pi(4)(0.75)}{60} \right]^3 (0.145^3 + 0.295^3 + 0.445^3)$$

$$P = 0.47 = 0.5 \text{ Watts}$$

3. Velocity Gradient

In order to determine the $\overline{G}$ value, the power required by the blades is equated to the water

power input required, and $\overline{G}$ is back calculated for 3 rpm and 4 rpm.

The water power input required is calculated:

$$P = \overline{G}^2 \mu V$$

N = 3 rpm

$$\overline{G} = \sqrt{\frac{P}{\mu V}} = \sqrt{\frac{0.2}{0.001 \text{ x } 1.763}} = 10.65 \text{ s}^{-1}$$

N = 4 rpm

$$\overline{G} = \sqrt{\frac{P}{\mu V}} = \sqrt{\frac{0.5}{0.001 \text{ x } 1.763}} = 16.84 \text{ s}^{-1}$$

4. Reynolds Number

In addition, the Reynolds number is calculated to ensure that the flow is turbulent.

$$Re = \frac{D_{pw}{}^2 N \rho}{\mu}$$

N = 3 rpm

$$Re = \frac{0.94^2 (3/60)(1000)}{0.001} = 44{,}180$$

N = 4 rpm

$$Re = \frac{0.94^2 (4/60)(1000)}{0.001} = 58{,}910$$